Imperial College London

Exploring the Behaviour of Two-Dimensional Dry Polar Active Fluids in a Dense Regime

David Michael Nesbitt

Thesis submitted for the degree of Doctor of Philosophy

Department of Bioengineering
Imperial College London

supervised by

Dr Chiu Fan Lee, *Dept. of Bioengineering*
Dr Gunnar Pruessner, *Dept. of Mathematics*

February 14, 2020

Declaration

I declare that the work presented within this thesis is entirely my own with the exception of any material that is cited from publications other than my own.

It must be acknowledged that only part of the material presented in Chapter 4 was completed as part of the PhD submission. The results for the 'Stationary case' were obtained by me and Dr. Chiu Fan Lee in 2015 as part of a previously awarded MRes project. The results for the 'Moving case' were completed as part of the PhD and should be treated as new material. The interpretation of the results, including those from the stationary case, was also expanded upon during the PhD.

David Nesbitt
February 14, 2020

Publications

The work presented in Chapter 4 was published in the paper:

D. Nesbitt, G. Pruessner, and C. F. Lee, "Edge instability in incompressible planar active fluids," *Physical Review E*, vol. 96, no. 6, pp. 1-7, 2017.

The work presented in Chapters 2 & 3 has been submitted for publication:

D. Nesbitt, G. Pruessner, and C. F. Lee, "Uncovering novel phase transitions in dense dry polar active fluids using a lattice Boltzmann method," 2019. The paper has been accepted for review in *Physical Review Letters*.

Presentations

The work in this thesis has been presented at a number of events:

The Physics of Soft and Biological Matter (oral presentation)
Institute of Physics
Homerton College, Cambridge, UK
April 2016

CDT in fluids across scales student symposium (oral presentation)
Imperial College London, UK
June 2016

UK Fluids (oral presentation)
Imperial College London, UK
September 2016

Computational & Physical Biology Interest Group Afternoon Workshop (poster presentation)
Francis Crick Institute, London, UK
December 2016

CDT in fluids across scales student symposium (oral presentation)
Imperial College London, UK
June 2017

UK Fluids (oral presentation)
University of Leeds, UK
September 2017

APS March Meeting (oral presentation)
Boston, USA
March 2019

Copyright

Acknowledgements

I am eternally grateful to my supervisor Dr Chiu Fan Lee, without whose guidance this thesis would simply not exist. In addition to providing scientific advice, Chiu Fan has been instrumental in helping me remain positive during the difficult times of my PhD, as has Dr Gunnar Pruessner, and I am extremely grateful to both. Gunnar was also invaluable in providing an alternative perspective on my work, as well as a source of fresh ideas. Finally, I am grateful to both for being simply a pleasure to work and socialise with.

I'd like to thank the other members of my supervisors' groups, and other regular attendees of the Biological Physics Journal Club, for many an interesting conversation, and for the copious amounts of feedback on my presentation style. Particular thanks go to JD Wurtz, Andrea Cairoli, and Benjamin Partridge, who endured more than their fair share of my talks.

I want to thank everyone associated with the CDT in fluids across scales, especially my fellow members of Cohort 1, Alejo, Aran, Emma, Laura, Marco, Paige, Owen, Raquel and Steven. I'd also like to thank our administrator Clodagh Li, who did so much for all of us.

I must thank Becca and my parents for their love and support, as well as the many other members of my extended family who have always been keen to see me succeed. I'd also like to thank Becca's parents for all that they've done to help me during the last two years.

Finally I want to thank all of my friends who have supported me. Special thanks must go to my mathematician friends from Cambridge, Gavin, Phil and Will, my former mentor, Dr Tadashi Tokieda, and my flatmates from my time in London, Maxi, Ginka, Andrew and Tom.

Abstract

Active matter is the study of many-body systems driven out of equilibrium at a local level. Typical examples are found in biology and span many length scales, such as flocks of birds or tissues of cells. This thesis focuses on non-momentum conserving (dry), polar systems, whose hydrodynamics are generically described by the Toner-Tu equations. These systems exhibit a variety of emergent behaviour, such as collective motion and phase separation, which often only emerge at high densities.

By adapting the standard lattice Boltzmann method for fluid mechanics, we develop a new method for simulating dry, polar active fluids. In particular this method is easy to implement and effective at high densities. Through a Chapman-Enskog style expansion, we confirm that the corresponding macroscopic equations are the Toner-Tu equations, and connect the system parameters with the coefficients of the equations.

We demonstrate the functionality and adaptability of our method by recreating two different phenomena: motility-induced phase separation and collective motion. Furthermore, by incorporating contact inhibition of locomotion effects into the collective motion model, we uncover two new first order phase transitions and a potentially new critical transition. We interpret these transitions through a stability analysis.

In addition, we perform a stability analysis on an open interface of a fluid that obeys an incompressible version of the Toner-Tu equations. We find that collective motion stabilises the interface, but the interface is unstable when starting from a stationary state. This has implications for both wound healing and the results of our simulations.

Contents

List of Figures

Chapter 1

Dry active matter

Active matter refers to any system of interacting bodies, some or all of which can expend internally stored or ambient energy to generate self propulsion [1]. This broad definition encapsulates a diverse collection of systems spanning a wide range of length and time scales. Examples include: flocks of birds [2], schools of fish [3], herds of mammals [4], tissues of cells [5–8], collections of swimmers such as spermatazoa [9] or colonies of bacteria [10–12], and networks of actin filaments [13] or microtubules [14, 15].

In recent decades there has been a growing movement amongst physicists to examine active matter as a special class of non-equilibrium system [16, 17]. Unlike a classical many body problem, driven out of equilibrium by a localised source of energy, active matter systems are driven out of equilibrium by some or all of the constituent particles themselves [1, 16]. The goal of most studies is to determine the conditions and mechanisms required to generate the observed emergent phenomena of the systems, be it self-organization [15, 18–21], pattern formation [13, 22–27], active turbulence [15, 28–32], phase separation [16, 21, 33–37], orientational order [38, 39] or collective motion [3, 40–49].

1.1 Classification

The broad definition of active matter means that the field is simply too diverse to describe every system with one model. However, efforts have been made to find connections between systems which share certain characteristics and emergent behaviour [1]. As we shall see these characteristics are inherently linked to the symmetries of the systems, a theme we will return to frequently in the course of this thesis.

1.1.1 Dry and wet

One of the main distinguishing features is how the self-propulsion is generated; specifically via a method that conserves momentum or one that does not. If a system is dominated by friction, say through interaction with a fixed substrate in two dimensions or porous media in three, then the system is said to be **dry**. The active particles can accelerate, whilst the solid media remains unchanged, hence momentum is not conserved. Dry active matter includes most systems confined to a solid surface, such as herds of animals and collective cell migration [1].

In contrast, systems with a liquid medium are referred to as **wet** active matter. For an active particle to propagate forward they must send the ambient fluid in the opposite direction, thus conserving total momentum. This induces a velocity field in the medium, which in turn affects the motion of other active particles in the system, perhaps even over long distances. In this case forces are generated with respect to the relative velocities between the active particles and the ambient medium, therefore Galilean symmetry is upheld. Wet active matter includes systems of swimmers, such as bacterial suspensions and spermatazoa, although not all systems suspended in a fluid need be considered wet. For example, birds can fly only by inducing flow in the surrounding air, however flocks of birds are frequently treated as dry systems [1]. In minimal flocking models, many of which are inspired by birds, each particle is typically assumed to respond only to the positions and orientations of other particles, and is unaffected by the medium in between

[50, 51]. Certainly if the Reynolds number of the air is high enough, the effects of a single bird will be short ranged. Furthermore, there is evidence that, in large flocks of starlings, the individuals do not seek the energy-saving benefit of resting in other birds' wakes [2].

1.1.2 Polarity

In most of the cases studied, active particles are elongated and the direction of their propulsive forces is dictated by their shape. The symmetry of an elongated particle only allows for two possibilities. If the particles generate forces in a specific direction relative to their axis, we can identify a 'head' and a 'tail', and as such the particle is considered to be polar. Alternatively, if the head and tail are indistinguishable, perhaps because the particle is oscillating back and forth, or because it generates a force dipole, then the particle is said to be nematic. It is therefore natural to consider the polar or nematic order of the entire system. A particle does not have to be elongated to exhibit either of these types of forces. On a hydrodynamic level the shape is largely irrelevant and we are more concerned with the symmetries of the forces involved, than the symmetries of the shape.

Furthermore, polar particles do not always exhibit collective polar order. For example, microtubules are polar structures, however if bundled together with alternating polarity, as in an antiferromagnet, and driven by kinesin motors, the resulting global order is nematic [15]. As such, the order of a system depends not just on the symmetries of the individual particles, but on the symmetries of their interactions.

1.2 Emergent phenomena

This thesis is concerned with dry polar active matter in two dimensions. So far we have only described the properties of individual active particles. A collection without any interactions would be the active equivalent of an ideal gas, which, it should be stressed, is already significantly different from its passive counterpart due to a microscopic irreversibility, as evidenced through

interactions with ratchet-like structures [16,52,53]. Including interactions between particles, such as repulsion, attraction and alignment creates a wealth of emergent behaviours. We examine three cases in particular.

1.2.1 Motility-induced phase separation

Perhaps the simplest form of interactions are purely repulsive. Intuition may suggest that repulsive forces flatten a density profile, with particles trying to maximise their distance away from their neighbours. In fact when a persistent self-propulsion is coupled with short range repulsive forces, the very opposite can happen, resulting in what is known as motility-induced phase separation (**MIPS**) [16, 33, 54–58].

This arises from two related mechanisms. Firstly, it has been observed that active particles tend to congregate in regions where their speeds are slow [59]. This is well demonstrated using light sensitive strains of *E. coli* bacteria, with heterogeneous distributions of light leading to matching density profiles [60].

Secondly, in systems with repulsive forces, the converse is also true; in areas with high densities, the speeds slow down. The exact reason for the slowdown differs depending on the system of interest. Run-and-tumble bacteria respond to chemical secretions by their neighbours, which affects their own behaviour [61]. Active Brownian particles on the other hand don't alter their behaviour in the presence of other particles. Rather, at high densities, they experience many collisions in a short time, disrupting their motion. If their trajectory is averaged over a short interval, they are seen to effectively slow down at higher densities [33, 54].

In either case, under certain circumstances a positive feedback loop can develop and an instability occurs. A density fluctuation leads to a small region of higher density, with slower speeds. If the drop in speed is drastic enough, then more particles will congregate due to the slower speeds. The density rises further and the dense region grows spatially until it reaches a stable equilibrium with two phases: a dense liquid phase and a sparse gas phase.

1.2.2 Collective motion

A closely related property to the polarity of an active system is collective motion. In the previous section, there was no overall flow in the system in either phase. MIPS arises purely out of variation in the typical speeds of the particles, under the assumption that the distribution of particles' directions is approximately isotropic. Here we consider interactions that specifically align the particles. These interactions are purely orientational, hence they are distinct from repulsive or attractive forces, either of which may be included in conjunction.

Although exhibited by a range of examples, the emergence of collective motion from a many-bodied system is generally referred to as flocking, as many of the seminal studies were inspired by the dynamics of flocks of birds [40]. A variety of techniques have been employed over the years, to understand the basic mechanisms at play, and to characterize the onset of collective motion using the language of phase transitions [7, 42, 47, 50, 51, 62–66].

A particularly well known model that exhibits a transition to collective motion is the minimal agent-based Vicsek model [42, 50, 51, 62, 63, 67]. The model evolves many point particles discretely in time at a fixed speed. At each step the particles reorientate themselves to align with the net direction of all its neighbours within a fixed radius, plus some stochastic noise [50]. Therefore if the particle speeds are set to zero, the system reduces to that of a 2D XY model [51]. No other forces are included, and no specific direction is imposed on the system. As the particles move at fixed speed, and are never impeded by neighbouring particles, it is unambiguous to refer to the polar order and the net velocity as the same thing. Some sample frames from a Vicsek model are shown in Fig. 1.1.

Starting from a noisy system of complete disorder, as the average density increases, or equivalently the noise strength decreases, a spontaneous breaking of symmetry occurs, resulting in collective motion, with a net velocity that is stable and changes direction slowly in time. Most interesting of all is the transition between these two states. Rather than alignment smoothly increasing across the system, phase separation occurs, forming a dense aligned

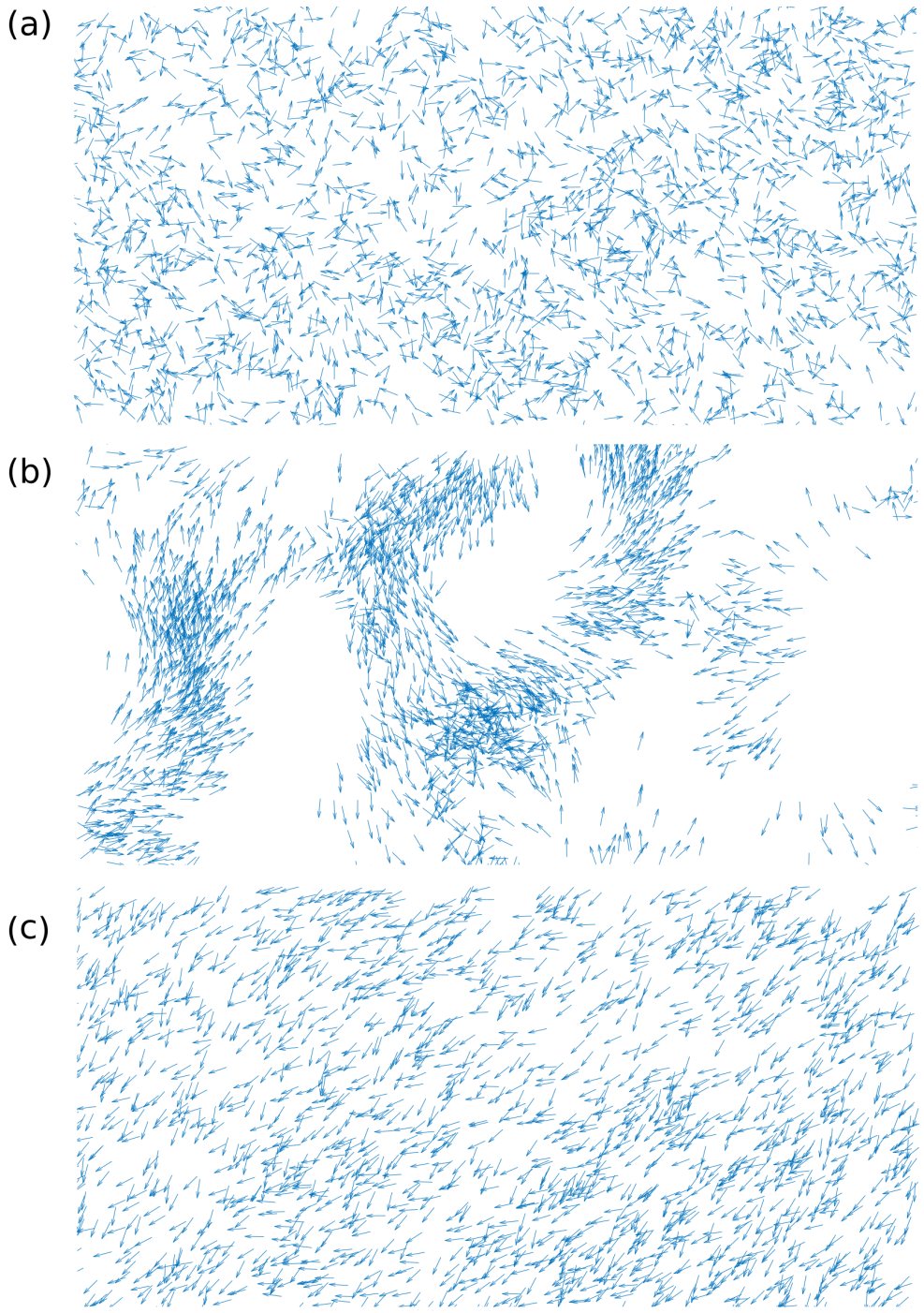

Figure 1.1: Example frames from a Vicsek model, which studies flocking dynamics. Each arrow represents the location and direction of a point particle. At each time step the arrows advance forward by a constant distance, then reorientate to align with the net direction of all neighbours within a fixed radius, plus some stochastic noise. Boundary conditions are periodic. (a) shows a noisy system with no global order, (b) shows a system in the process of aligning, (c) shows a final steady ordered state.

phase, which then propagates through the disordered sparse phase [63]. In periodic geometries, the aligned phase typically forms bands in two dimensions, or planes in three dimensions, which propagate in a direction normal to the interface. This transition was originally believed to be continuous [50], however this result has since been attributed to finite size effects, with the transition now believed to be discontinuous [63].

1.2.3 Fingering instability

Finally we consider a system which includes attractive forces. Isolated epithelial cells will naturally crawl on the substrate they rest upon, suggesting they qualify as dry polar active matter [68]. Together they form tightly packed epithelial sheets. Given room to manoeuvre, such as in a wound healing experiment, they will collectively flow to fill the void, but do not separate from one another, demonstrating that there are adhesive forces between the cells [48, 69–72]. A commonly observed phenomenon in wound healing assays is that an initially straight wound does not heal uniformly, rather, finger-like protrusions develop which propagate into the void [69, 71, 72]. The primary mechanism driving this phenomenon is a matter of debate. Some believe it is due to specialised 'leader cells' at the tip of each finger, dragging the other cells behind them [69, 71–73]. Alternatively, studies have suggested that it is an emergent phenomenon, resulting from the collective interaction of the cells, implying it should be treated as an active matter problem [8].

Furthermore, there is disagreement over what type of active matter the tissue should be considered as. Although individually the cells behave in a polar fashion, experiments on monolayers have observed weak nematic order, as recognised by the presence of nematic defects [74–76]. Topological defects are discontinuities in the director field, and are realised in a finite number of distinct shapes. These shapes depend on the symmetries involved, as demonstrated in Fig. 1.2. If polar interactions dominate a system, then all nematic defects would be eliminated. The presence of nematic defects implies that the cells actually interact in a nematic manner. One way to shed light on the nature of the system is to attempt to replicate observable behaviour

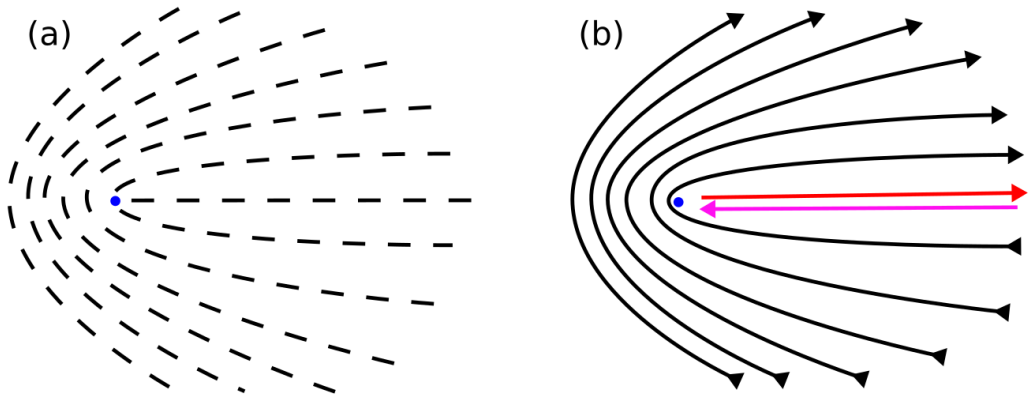

Figure 1.2: (a) An example of a nematic defect (blue spot) in two dimensions. The dashed lines represent the orientation of head-tail symmetric particles. The field is ordered as neighbouring particles are aligned, but the direction of the field is not well defined at the blue spot, hence it is a defect.
(b) Here we have recreated this situation with a polar field, in which asymmetric particles align with their neighbours. As they are asymmetric the particles can be associated with a direction, and thus can be represented by a vector field, with the direction signified by the arrows. The red arrow is consistent with the field directly above, whilst the magenta arrow aligns with the field directly below. However, as they point in opposite directions, this clearly violates the rule of particles aligning with their neighbours. In two dimensions this rule violation can be tolerated at a single point as in (a), but not along the length of a line, as the situation would be inherently unstable. As such, this type of defect is specific to nematic systems, and is not exhibited by polar fields.

with the various models. We investigate this further in Chapter 4.

1.3 Modelling

A recurring theme from these systems is phase separation, with a significant variation in density between the two phases. In the first two, the phase separation emerges from the system, whilst the fingering instability is exhibited during the relaxation of an artificially created phase separation. In particular, all of these phenomena occur only in a dense regime. Therefore it is imperative that the methods employed to study these systems are effective

at high densities.

Now that we have introduced the systems of interest, how best can we model these systems, especially in the dense regime? Biological systems are typically complex, so to draw comparisons excess detail must be stripped away to leave the core mechanics that generate the behaviour of interest. A variety of techniques have been established over the years, but largely fall under the following categories.

1.3.1 Agent-based modelling

We have already introduced a quintessential example of agent-based modelling of active matter, namely the Vicsek model. This is an extremely minimal model, designed only to capture the effects of flocking, without even volume exclusion. The Vicsek model has inspired many variations, incorporating more effects, such as cohesive forces [42], turning effects [77], velocity reversals [32], chirality [78], to name just a few. In addition to collective motion, there are many agent-based models investigating MIPS [12, 33], and tissue mechanics [8, 79–81].

All molecular dynamics simulations come with a computational cost. Whilst easy to program for a small number of particles, the complexity increases dramatically with the number of particles N. Not only does the motion of each particle have to be tracked at each time step, its trajectory is determined through the interactions with its neighbours, which must therefore be calculated. Hence a naïve approach to the system will have complexity of order $O(N^2)$. Smarter algorithms can improve upon this for systems without long-range interactions, obtaining an order of $O(NN_c)$ where N_c is the average number of neighbours within interaction range [67]. However, N_c also increases with density, meaning that to simulate a dense regime comes with a hefty computational cost. As a guide, current state of the art simulations of Vicsek models involve tens of millions of particles [67].

1.3.2 Symmetry and hydrodynamics

We established earlier that the categories of wet and dry, polar and nematic, are based on the symmetries of the systems. This is not a coincidence. When coarse grained to a hydrodynamic level, the microscopic details of a system of particles become largely irrelevant, and it is the symmetries which determine the equations of motion. This principle is the foundation of fluid mechanics. For simple passive fluids, these are the famed Navier-Stokes equations. It is noteworthy that the same equations apply for many different fluids. There is no "Navier-Stokes for water" and a different "Navier-Stokes for air" — they are one and the same. Microscopically these fluids may not be similar at all, yet on a much larger scale the differences are mostly irrelevant. The only change to the equations of motion are the values of the coefficients. In fact if we consider an arbitrary system of particles, and insist that it respects temporal, rotational, translational, chiral, and Galilean symmetries, then that system is necessarily described by the Navier-Stokes equations in the hydrodynamic limit. [82] In this way, the Navier-Stokes equations are said to be universal.

The same logic can be applied to active systems. For dry polar active matter, the Galilean symmetry is broken, as is conservation of momentum. This leads instead to the Toner-Tu equations [40, 41, 43, 49]

$$\frac{\partial \rho}{\partial t} + \nabla \cdot (\rho \mathbf{u}) = 0 \ , \tag{1.1a}$$

$$\begin{aligned} \frac{\partial \mathbf{u}}{\partial t} &+ \lambda_1 (\mathbf{u} \cdot \nabla) \mathbf{u} + \lambda_2 (\nabla \cdot \mathbf{u}) \mathbf{u} + \lambda_2 \nabla \left(|\mathbf{u}|^2 \right) \\ &= -\nabla P_1 - \mathbf{u}(\mathbf{u} \cdot \nabla) P_2 + \left[\alpha(\rho) - \beta |\mathbf{u}|^2 \right] \mathbf{u} + D_T \nabla^2 \mathbf{u} \\ &\quad + D_1 \nabla (\nabla \cdot \mathbf{u}) + D_2 (\nabla \cdot \mathbf{u})^2 \mathbf{u} + \mathbf{f} \ , \end{aligned} \tag{1.1b}$$

in the hydrodynamic limit, where ρ is the density field, and $\mathbf{u}$ the velocity field. P_1 and P_2 are pressure terms, isotropic and anisotropic respectively, and $\mathbf{f}$ is a delta-correlated noise function. The continuity equation (1.1a) is the same as in the Navier-Stokes equations, however the momentum equation (1.1b) has many more terms. This is to be expected, since the continuity equation is simply enforcing conservation of mass, which still holds in a typi-

cal polar active fluid, but conservation of momentum certainly doesn't, hence the new terms.

Although there are many ways of deriving these equations, the method that Toner and Tu used was to appeal to symmetry [40]. Assuming that the dynamics of $\mathbf{u}$ depend only on functions of ρ and $\mathbf{u}$, they listed every possible combination of terms that the dimensionality and symmetries permitted. This list includes many more terms that do not feature in Eq. (1.1b); these extra terms were eliminated by considering orders of magnitude and observing that in the hydrodynamic limit they are negligible in comparison.

Eq. (1.1b) appears to be far too complicated to solve, with a plethora of non-linear terms. However for the purposes of this thesis, the key term to note is that of $[\alpha(\rho) - \beta|\mathbf{u}|^2]\,\mathbf{u}$. This term is simultaneously a driving and a damping force, and does not depend on the derivatives. For $\mathbf{u}$ to be bounded we must have $\beta > 0$. The sign of α then heavily impacts the nature of the system. If $\alpha < 0$, the system is constantly applying the brakes, with all velocity experiencing drag. On the other hand if $\alpha > 0$, the system has a steady solution: a constant uniform flow with

$$|\mathbf{u}| = \sqrt{\frac{\alpha(\rho)}{\beta}}\ . \tag{1.2}$$

This solution is that of uniform ordered collective motion. The fact that it can be a solution to the system (in the absence of stochastic noise) is an excellent indicator that these equations do indeed model a polar active fluid. Note that the solution only dictates the speed, not the final direction. There is no preference to the direction; there is no external field applied.

Although we have established that dry polar systems are described by the Toner-Tu equations (1.1), solving these equations is far from trivial, with an abundance of non-linear terms. Furthermore the effects of each term on the system are not always obvious, and to reproduce the dynamics of a particular system, one would need to know the values of the coefficients. This is a limitation of the symmetry method of derivation; we gain no information about the values of the parameters.

1.3.3 Kinetic theory

A potential remedy to the issue of unknown parameters is to derive the hydrodynamics by another means. Rather than appealing to symmetry to determine the form of the macroscopic equations, one can instead derive the equations starting from the microscopic system, using multiscale expansions [44, 64, 66, 83–85]. Typically this involves first approximating the system to a one-particle distribution function, $f(\mathbf{r}, \boldsymbol{\xi}, t)$, described by a Boltzmann equation [83],

$$\frac{\partial f}{\partial t} + \boldsymbol{\xi} \cdot \nabla f = I_{\text{dif}}[f] + I_{\text{col}}[f] \ , \tag{1.3}$$

where $I_{\text{dif}}[f]$ and $I_{\text{col}}[f]$ account for the self-diffusion and collision effects respectively. $f(\mathbf{r}, \boldsymbol{\xi}, t)$ should be interpreted as a probability density of a particle at location $\mathbf{r}$ and time t moving with velocity $\boldsymbol{\xi}$. For particles in two dimensions moving at fixed speeds, $\boldsymbol{\xi}$ can unambiguously be described by an angle θ indicating the direction of motion [44, 66, 83]. The macroscopic variables, and hydrodynamic equations, are then obtained by integrating over various moments of f to remove the dependency on $\boldsymbol{\xi}$.

This approach has its own downsides. Determining a closed useful expression for $I_{\text{col}}[f]$ is extremely difficult, even in the simplest case where only binary collisions are considered, which itself is only valid in a sufficiently dilute system [66]. In order to proceed more approximations are employed, such as truncating the expansions in the Fourier-space representation of the angular argument of Eq. (1.3) [83]. The resulting macroscopic equations are consistent with the Toner-Tu equations (1.1) [83], and the microscopic parameters can be linked to the macroscopic coefficients, but the number of approximations made in the process raises questions about the range of validity of this approach.

1.4 A mesoscopic approach

As a main part of this thesis we develop a new method for simulating dry polar active matter based on the lattice Boltzmann method for simulating passive fluids, the details of which are presented in Chapter 2. This method

effectively solves a discretised Boltzmann equation (1.3) for dry polar active systems. As opposed to deriving the form of $I_{\text{col}}[f]$ directly from the microscopic system of interest, we instead adapt the result for the standard lattice Boltzmann method, using symmetry and phenomenological arguments. As a result we expect our results to be applicable to multiple systems who share these symmetries. Furthermore the method is easy to implement and functions effectively in the dense regime. We also prove that our model indeed reproduces the Toner-Tu equations in the hydrodynamic limit using Chapman-Enskog style multi-scale expansions.

We demonstrate the versatility of our method by using it to simulate two types of dry polar active matter; that is, a system that exhibits MIPS, and a system that exhibits collective motion. The results of our method are presented in Chapter 3. Not only can we successfully reproduce the phenomena of both MIPS and collective motion, but by including contact inhibition of locomotion effects into our alignment model we discover two new first order phase transitions and a potentially new critical transition. We also use the Toner-Tu equations to interpret our new-found phase transitions from the perspective of a stability analysis. Using a renormalization technique, we successfully connect the parameters of our model with those of the Toner-Tu equations.

Finally in Chapter 4, we perform a stability analysis on a strip of fluid that behaves according to an incompressible version of the Toner-Tu equations. The results have implications both for wound healing and for the outcomes of our alignment model.

Chapter 2

Lattice Boltzmann methods applied to dry active matter

In this chapter, we introduce the standard lattice Boltzmann method for simulating fluid flow, and explain how this can be adapted to describe dry active systems with two simple, but significant, adjustments. In addition, we derive the corresponding hydrodynamic equations using a Chapman-Enskog expansion, and observe that they are a version of the Toner-Tu equations, as expected from the symmetries of the modified system.

2.1 Lattice Boltzmann methods for passive fluids

Simultaneously solving the equations of motion for every single constituent molecule of a fluid would be a monumental task. Thankfully, we have no need to do so if we are concerned only with the collective effect. Instead, by ignoring the microscopic details and treating the system as a continuum, a new set of governing equations can be derived which describe the large scale behaviour of the system. Information, such as the trajectories of individual particles, is lost in the process, but the task is simplified to a significantly more manageable challenge. For simple fluids, these macroscopic equations are the famed Navier-Stokes (**NS**) equations. Despite the simplification, solv-

ing these non-linear partial differential equations analytically still remains a formidable challenge. With the exception of some noteworthy exact solutions, numerical solutions are the best we can collectively obtain. As such, an abundance of computational methods have been developed with the aim of directly integrating the equations to higher and higher accuracy whilst minimizing computational time. Perhaps none are quite like the Lattice Boltzmann method (**LBM**). Instead of solving the NS equations directly, the LBM evolves a Boltzmann equation describing a microscopic system which in no way resembles a physical fluid, yet whose macroscopic behaviour obeys the NS equations. [86, 87].

That such a method should work emphasises the universality of the Navier-Stokes equations. By identifying the underlying symmetries of a classical many-body system, one can derive the hydrodynamic equations of motion (**EOM**) that govern the macroscopic dynamics of that system, and, crucially, any other system that respects the same symmetries [88]. In the case of simple fluids, temporal, rotational, translational, chiral, and Galilean symmetries necessarily lead to the Navier-Stokes equations in the hydrodynamic limit [82]. Conversely, breaking any one of these symmetries would likely render the NS equations invalid for describing such a system. For example, removing both the Galilean symmetry and conservation of momentum leads instead to the more general Toner-Tu EOM (1.1) [40,41,49], which generically describe dry polar active fluids [1].

Analysis of a hydrodynamic theory can elucidate the universal behavior exhibited by all generic systems respecting the prescribed set of symmetries; conversely, any particular many-body system defined by certain microscopic rules that respect the same set of symmetries can also be used to study the associated universal behaviour in the hydrodynamic limit. This is the reason that 'toy' models in physics are so useful and can provide insights beyond their own curiosities — if a toy system respects the same symmetries as a more physical system then it must exhibit the same universal behaviour in the hydrodynamic limit. This is how lattice gas cellular automata systems, the predecessor of LBMs, can be relevant to fluid mechanics. Although they consist of discrete particles moving and interacting on a lattice in discrete

time, with the right collision rules they exhibit behaviour identical to the NS equations in the hydrodynamic limit [89].

This is a powerful concept. A simple system can be studied in place of a much more complex one provided that they share the key similarities. By constructing a minimal model, stripped of unnecessary detail, computation time and effort can be saved. The crucial question is what is the minimal level of detail required to accurately achieve the goal. The history of lattice gas models reveals the challenge this question once posed. The first model which fits the description above was the Hardy, de Pazzis and Pomeau (**HPP**) model [90–92]. Defined on a square lattice, it can successfully produce some features typically associated with fluid flows, however the method itself is insufficient for exploring the full NS equations as it cannot generate the non-linear effects, nor the dissipative term. The problem was discovered to be a lack of isotropy in the system, a problem that was solved by Frisch, Hasslacher and Pomeau in two dimensions and d'Humiéres, Lallemand and Frisch in three dimensions [86, 89, 93].

Lattice Boltzmann methods are a natural evolution from this formula and were developed towards the end of the 1980s [94–97]. Lattice gas automata are Boolean and stochastic in nature; results are obtained only through copious statistical averaging across large time and length scales [96]. The lattice Boltzmann framework effectively performs this averaging in advance, and, instead of finite particles, transports and collides probability densities according to a Boltzmann equation. As a result LBMs are (typically) deterministic systems, and need only be solved once [96]. Other more pressing issues are also resolved. Lattice gas models do not exhibit Galilean invariance, and the equation of state is velocity dependent; both of these issues are remedied in the LBM [97].

Lattice Boltzmann methods have their limitations: they cannot recreate supersonic flows as a low Mach number is a key assumption in their derivation [98, 99]. A further consequence is that they exist in the incompressible limit, but they are not strictly incompressible, though attempts have been made to achieve as much [99–101]. The pressure field is related to density by an equation of state, whereas in the incompressible NS equations the pressure

term is a Lagrangian multiplier.

The key advantages of LBMs come in their simplicity. They are relatively easy to program when compared with direct NS solvers and can be heavily parallelised [86, 98]. Boundary conditions are especially simple to apply in a lattice gas model [87]. A no-slip condition can easily be implemented by simply reflecting any particles that arrive at a boundary node, causing the particle to 'bounce-back', travelling back along the path it arrived on with its velocity reversed [87, 102]. The same idea extends to lattice Boltzmann models, although it should be noted that whilst the LBM is second order accurate in the Mach number, the bounce-back boundary condition gives only a first order accurate no-slip condition [87]. As a result it lowers the accuracy of the system. Nonetheless the simplicity in applying the rules makes the LBM ideal for complex geometries and have been extensively used to simulate flows through porous media [103].

The adaptability to complex geometries also has uses in the world of active matter as LBMs have been employed to simulate the fluid part of suspensions of active swimmers [104]. In these simulations the active swimmers are each several lattice spaces in diameter and are modelled as collections of boundary nodes with specified surface pressures. Not only do they induce flow in the surrounding medium, they in turn respond to the flow and propagate through the system, meaning that the nodes must fluctuate between being boundary nodes or being in the fluid depending on the current location of the particles.

Other variations of LBMs have also been used for simulating complex fluids such as passive and active liquid crystals [28,30,74–76,105–115]. This is typically accomplished by solving the fluid part of the system with LBMs and using an alternative method, such as finite differences, to solve the nematic crystal part. This combination of methods has earned them the title of hybrid lattice Boltzmann methods.

These examples all describe wet active matter with momentum conserving forces [1], however the development of the LBM for dry active fluids is still missing, which is the focus of this chapter. Lattice gas models have been successfully used to simulate active matter [116, 117], however, like their passive counterparts, these systems require extensive averaging over long time

frames in order to produce results. By designing a lattice Boltzmann style simulation, we hope to reduce the total computation time, whilst also creating a robust model that can be easily adapted to produce a variety of active systems. In this thesis we modify the conventional LBM to reproduce two different behaviours of dry polar systems in two dimensions: motility-induced phase separation (MIPS), and collective motion with contact inhibition of locomotion (CIL). The simulation method developed enables us to explore the rich phase behaviour of the systems. In particular, in the CIL model we have uncovered two novel first-order and a potentially novel critical transition. These results will be discussed in detail in Chapter 3.

2.2 Overview of the lattice Boltzmann method

The lattice Boltzmann method refers to solving the discretised Boltzmann equation on a lattice. The Boltzmann equation itself concerns the temporal evolution of a distribution function $f(t, \mathbf{r}, \boldsymbol{\xi})$, which here corresponds to the mass density of matter moving with velocity $\boldsymbol{\xi}$ at location $\mathbf{r}$ and time t. Although f is the variable being evolved in time, it is rarely the object of interest; rather macroscopic variables obtained from f are the goal. In simple fluid simulations the typical variables of interest are the mass density field ρ, and the velocity field $\mathbf{u}$, which are related to f by

$$\rho(t, \mathbf{r}) = \int \mathrm{d}^{\mathrm{D}}\boldsymbol{\xi}\ f(t, \mathbf{r}, \boldsymbol{\xi}) \tag{2.1a}$$

$$\rho(t, \mathbf{r})\mathbf{u}(t, \mathbf{r}) = \int \mathrm{d}^{\mathrm{D}}\boldsymbol{\xi}\ f(t, \mathbf{r}, \boldsymbol{\xi})\boldsymbol{\xi} \tag{2.1b}$$

where D is the spatial dimension.

Discretizing $\boldsymbol{\xi}$ into a finite number of velocity vectors, $c\,\mathbf{e}_i$ directed towards neighbouring spatial nodes naturally constructs a lattice in the domain. The evolution equation can be expressed as

$$\frac{\partial f_i}{\partial t} + c\,\mathbf{e}_i \cdot \nabla f_i = \Omega_i \tag{2.2}$$

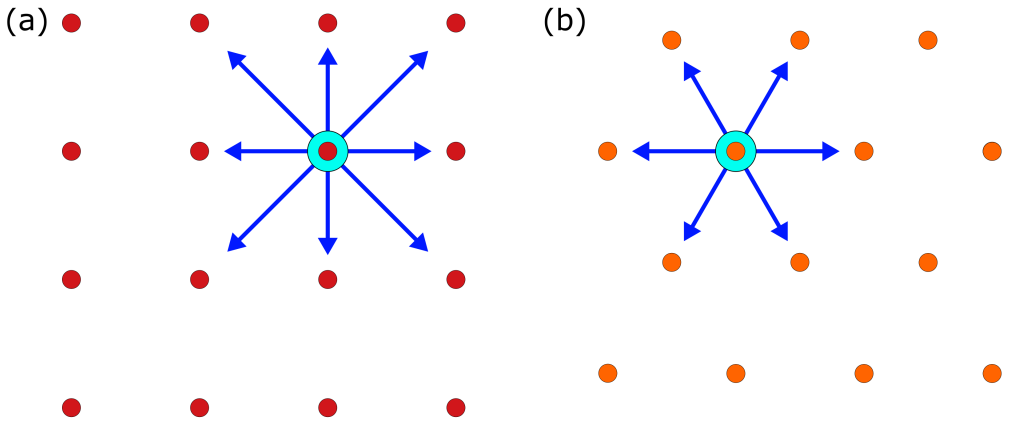

Figure 2.1: Lattice configuration for the (a) D2Q9 and (b) D2Q7 stencils. This shorthand indicates the dimension D (in this case both are two-dimensional), and the number Q of lattice vectors $\mathbf{e}_i$ directed to the nearest neighbours. These are demonstrated by the blue arrows for a particular node. Also included is a zero vector $\mathbf{e}_0 = \mathbf{0}$, denoted here by the cyan circles. Both of these configurations possess the required symmetries to accurately reproduce the behaviour of the Navier-Stokes equations.

where f_i is the mass density moving with velocity $c\mathbf{e}_i$ and Ω_i is a collision operator. It should be stressed here that in the discretisation of $\boldsymbol{\xi}$, an assumption has been made that the amount of material moving at speeds greater than $\max_i c|\mathbf{e}_i|$ is negligible. This restricts the realm of validity of the LBM, as we will discuss later.

The DQ notation is conventional for describing the lattice structure of the domain, where D is again the spatial dimension, and Q is the number of nodes each is connected to, including itself. Typically a 'zero' vector is included in the discrete directional space to help balance higher moments. Here we will take $\mathbf{e}_0 = \mathbf{0}$. There are many suitable choices of lattice, but they must contain the necessary number of symmetries to preserve enough higher moments of the system in question according to the desired level of accuracy [89, 118]. For example, a D2Q5 lattice, that is, a two dimensional square lattice is insufficient to accurately reproduce the Navier Stokes equations, as was observed in the HPP model [86], but a triangular lattice, D2Q7 (Fig. 2.1(b)), is sufficient [89, 118]. This is not to say that any square shaped

lattice cannot work — by including the diagonal components, as in the D2Q9 model (Fig. 2.1(a)), not only is a functioning model achieved, this model is more accurate than the D2Q7. Naturally the trade off is in computational efficiency. In the D2Q7 model the non-zero lattice vectors are all equivalent, but in the D2Q9 model, the diagonal directions require different weighting from the horizontal and vertical directions. Furthermore the speed of sound c_s is different. Even more specific lattices are required to acquire high enough orders of isotropy to study systems more advanced than isothermal fluids [118].

Here, we will focus on a D2Q7 lattice, which is a triangular lattice in two dimensions with a discretised distribution function $f_i(t, \mathbf{r})$, where $i = 0, 1, ..., 6$. The corresponding vectors are $\mathbf{e}_0 = \mathbf{0}$, and $\mathbf{e}_i = \cos[(i-1)\pi/6]\hat{\mathbf{x}} + \sin[(i-1)\pi/6]\hat{\mathbf{y}}$ for $i > 0$. The local mass density and velocity are thus given by

$$\rho = \sum_{i=0}^{6} f_i \quad , \quad \mathbf{u} = \frac{1}{\rho} \sum_{i=0}^{6} f_i c\, \mathbf{e}_i \ , \tag{2.3}$$

where the lattice speed c is the ratio of the lattice spacing Δx to the time increment Δt. For accurate solutions velocities must obey $|\mathbf{u}| \ll c$, which is known as the low Mach number assumption. As a result LBM cannot be used to simulate supersonic flows [119]. Typically scales in the LBM scheme are chosen such that $c = 1$, though this is not essential.

The discretised Boltzmann equation can then be evolved using the single relaxation parameter Bhatnagar-Gross-Krook (BGK) collision operator [120]

$$f_i(t + \Delta t, \mathbf{r} + c\mathbf{e}_i \Delta t) - f_i(t, \mathbf{r}) = -\frac{1}{\tau} \left[f_i(t, \mathbf{r}) - f_i^{\mathrm{eq}}(t, \mathbf{r}) \right] \ , \tag{2.4}$$

where $f_i^{\mathrm{eq}}(t, \mathbf{r})$ is a lattice dependent steady-state (equilibrium) distribution and τ is a relaxation parameter. When simulating the Navier Stokes equations, τ is linearly proportional to the viscosity, though its exact relationship to macroscopic parameters is lattice dependent. The evolution of this equation is typically split into two processes: the streaming step and the collision step, the latter of which is effectively a local redistribution. To obtain the NS equations in the macroscopic behaviour, the moments of f_i^{eq} should match

the symmetries of the NS equations. However, in a discretised system there are a finite number of degrees of freedom to work with, therefore it is impossible to match every moment ad infinum. As such, as many moments as possible are fulfilled, prioritising those of lowest order.

The first three moments are

$$\begin{aligned} \sum_{i=0}^{Q-1} f_i^{\mathrm{eq}} &= \sum_{i=0}^{Q-1} f_i = \rho \ , \\ \sum_{i=0}^{Q-1} f_i^{\mathrm{eq}} c\mathbf{e}_i &= \sum_{i=0}^{Q-1} f_i c\mathbf{e}_i = \rho\mathbf{u} \ , \\ \sum_{i=0}^{Q-1} f_i^{\mathrm{eq}} c^2 \mathbf{e}_i\mathbf{e}_i &= \rho\mathbf{u}\mathbf{u} + P \ . \end{aligned} \tag{2.5}$$

The pressure term P obeys a simple equation of state $P = c_s^2\rho$, where c_s is the lattice dependent speed of sound. These three moments have been shown to be necessary and sufficient to generate NS behaviour. In two dimensions these amount to six independent restrictions on the vector f_i^{eq}, hence Q must be at least six. This explains why a D2Q5 framework is insufficient, but D2Q7 is sufficient.

The general form of f_i^{eq} is of a truncated Taylor expansion in $\mathbf{u}$. In fact, the expression can also be obtained by discretizing the Boltzmann distribution for velocities at thermal equilibrium [98],

$$f^{eq} = \frac{\rho}{(2\pi RT)^{D/2}} \exp\left(-\frac{(\boldsymbol{\xi}-\mathbf{u})^2}{2RT}\right) \tag{2.6}$$

$$\approx \frac{\rho}{(2\pi RT)^{D/2}} \exp\left(-\frac{\boldsymbol{\xi}^2}{2RT}\right)\left[1 + \frac{\boldsymbol{\xi}\cdot\mathbf{u}}{RT} + \frac{(\boldsymbol{\xi}\cdot\mathbf{u})^2}{2\,(RT)^2} - \frac{|\mathbf{u}|^2}{2RT}\right] \ , \tag{2.7}$$

where R is the ideal gas constant, D is the spatial dimension and T is the temperature. For this truncation to be valid, $\mathbf{u}$ must be small, $|\mathbf{u}| \ll \sqrt{RT} = c_s$; this is the aforementioned low Mach number assumption. From here, as $\boldsymbol{\xi}$ is discretised to $\{c\mathbf{e}_i\}$, the prefactor $\exp(-\boldsymbol{\xi}^2/2RT)$ must be replaced with constants so as to satisfy Eq. (2.5).

In a D2Q7 framework

$$f_i^{\text{eq}} = w_i \rho \left[1 + 4\frac{\mathbf{e}_i \cdot \mathbf{u}}{c} + 8\frac{(\mathbf{e}_i \cdot \mathbf{u})^2}{c^2} - 2\frac{|\mathbf{u}|^2}{c^2} \right] , \tag{2.8}$$

where w_i are lattice specific weights: $w_0 = 1/2$ and $w_{i\neq 0} = 1/12$. For comparison the D2Q9 equivalent is

$$f_i^{\text{eq}} = w_i \rho \left[1 + 3\frac{\mathbf{e}_i \cdot \mathbf{u}}{c} + \frac{9}{2}\frac{(\mathbf{e}_i \cdot \mathbf{u})^2}{c^2} - \frac{3}{2}\frac{|\mathbf{u}|^2}{c^2} \right] , \tag{2.9}$$

where $\mathbf{e}_0 = \mathbf{0}$, $\mathbf{e}_1 = (1,0)$, $\mathbf{e}_2 = (0,1)$, $\mathbf{e}_3 = (-1,0)$, $\mathbf{e}_4 = (0,-1)$, $\mathbf{e}_5 = (1,1)$, $\mathbf{e}_6 = (-1,1)$, $\mathbf{e}_7 = (-1,-1)$, $\mathbf{e}_8 = (1,-1)$ and $w_0 = 4/9$, $w_i = 1/9$ for $i \in \{1,2,3,4\}$, $w_i = 1/36$ for $i \in \{5,6,7,8\}$.

Note that f_i^{eq} only depends on ρ and $\mathbf{u}$ and not the other values of f_i. As mentioned the speed of sound c_s is lattice dependent, as is the relationship between τ and the macroscopic viscosity ν. Explicitly these are

D2Q7: $$c_s = \frac{c}{2} , \qquad \nu = \frac{2\tau - 1}{8} c^2 \Delta t , \tag{2.10}$$

D2Q9: $$c_s = \frac{c}{\sqrt{3}} , \qquad \nu = \frac{2\tau - 1}{6} c^2 \Delta t . \tag{2.11}$$

These relationships are derived during the recovery of the Navier-Stokes equations in Section 2.5.1. As $\nu > 0$ necessarily, we require $\tau > 1/2$, although it should be noted that as τ approaches $1/2$, the system becomes unstable. As such, when simulating high Reynolds number (low viscosity) flows, it is advised that other system parameters, such as Δx and Δt, are modified to ensure τ is large enough for the system to be stable.

The significance of $\tau \geq 1/2$ can be readily understood by looking at a simpler problem. Recall that τ is a relaxation parameter, determining the rate at which the distribution f_i at a lattice site relaxes to the equilibrium distribution f_i^{eq}. Consider instead the simple difference equation

$$x_{i+1} - x_i = -\frac{x_i}{\tau} , \tag{2.12}$$

where $x_0 > 0$. This resembles Eq. (2.4), and describes a sequence x_i which

relaxes towards a constant value, in this case 0. If $\tau = 1$ it arrives at 0 in a single step. Rearranging

$$x_{i+1} = \left(1 - \frac{1}{\tau}\right) x_i \ . \tag{2.13}$$

If $\tau > 1$, then x_i steadily decreases without ever becoming negative, resembling an overdamped system. Conversely if $1/2 < \tau < 1$, the sequence tends towards 0 whilst fluctuating in sign, thus resembling an underdamped system. If $\tau \leq 1/2$ the sequence does not converge to 0 at all. Therefore the issue with τ being too close to $1/2$ in the lattice Boltzmann algorithm is actually a vanishing of the damping effect, hence the lack of stability in the system.

2.3 Basic algorithm

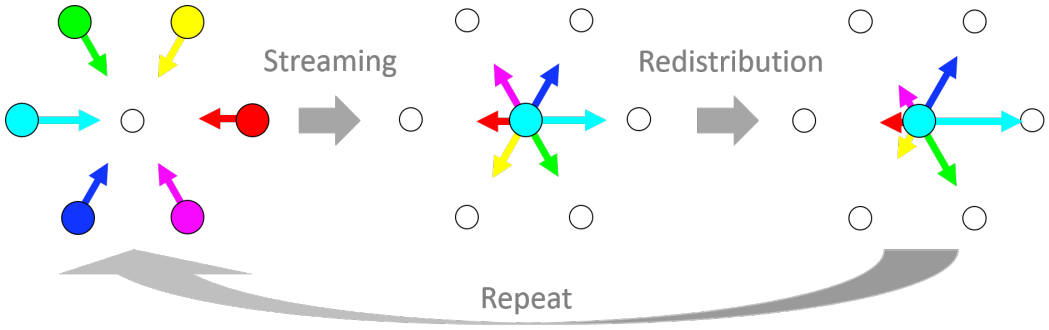

Figure 2.2: Schematic of the temporal evolution of a lattice Boltzmann algorithm for a single site. The collision step simply redistributes the values at a site towards the profile described by f_i^{eq}.

To evolve the system numerically the evolution equation (2.4) is typically broken into two alternating steps, namely the *streaming* step and the *collision* step. Some intermediate calculations are pre-requisite for the collision step so a more detailed description of the algorithm for a single step is as follows:

Standard LBM algorithm:

1. **Streaming step:** An intermediate *post-stream* distribution f_i' is evaluated by advancing all of the values f_i one lattice space forward in their corresponding directions, for each lattice site:

$$f_i'(\mathbf{r} + c\mathbf{e}_i\Delta t) = f_i(\mathbf{r}) \ . \tag{2.14}$$

2. **Calculate macroscopic variables:** Eq. (2.3) is employed to calculate the new values of ρ and $\mathbf{u}$ from the post-stream distribution f_i'.

$$\rho = \sum_{i=0}^{Q-1} f_i' \ , \qquad \rho\mathbf{u} = \sum_{i=0}^{Q-1} f_i' c\mathbf{e}_i \ . \tag{2.15}$$

3. **Calculate equilibrium distribution:** The equilibrium distribution is calculated using the newly found macroscopic variables ρ and $\mathbf{u}$. For the D2Q7 model:

$$f_i^{\mathrm{eq}} = w_i\rho\left[1 + 4\frac{\mathbf{e}_i\cdot\mathbf{u}}{c} + 8\frac{(\mathbf{e}_i\cdot\mathbf{u})^2}{c^2} - 2\frac{|\mathbf{u}|^2}{c^2}\right] \ . \tag{2.16}$$

4. **Collision step:** Assign new values to f_i, one time step ahead of the previous values, given by

$$f_i = f_i' - \frac{1}{\tau}\left(f_i' - f_i^{\mathrm{eq}}\right) \ , \tag{2.17}$$

   where f_i' is again the post-stream distribution.

Only the streaming step involves relating neighbouring lattice sites — all the remaining processes occur at individual sites, independent of all others. Therefore in a single time step information is at most transmitted by a distance of one lattice spacing. Hence the speed at which information can propagate through the system is determined by c and the geometry of the

lattice. Furthermore, deconstructing the algorithm in this way permits the use of parallelisation techniques for efficient computation.

Note that most LBM guides introduce the streaming step first, though it is irrelevant whether the streaming or collision step is performed first, so long as the macroscopic variables $\rho, \mathbf{u}$ are always calculated from the post-stream distribution. Strictly speaking f_i' as described here corresponds to $f_i(t + \Delta t, \mathbf{r} + c\mathbf{e}_i\Delta t)$ given in Eq. (2.4) and the initial distribution f_i would be the actual intermediate distribution, however given that the values of f_i are rarely of interest, this is unlikely to be a great source of confusion.

2.4 A lattice Boltzmann method for dry active fluids

So far we have described the basic algorithm for the LBM which recovers the Navier-Stokes equation in the incompressible limit. Here we will explain how we adapted the LBM for dry active matter. Some of the details are model specific. To date we have successfully recreated the behaviour of two types of dry matter using our LBM: a non-aligning system that exhibits motility-induced phase separation (**MIPS**), and a flocking system with contact inhibition of locomotion (**CIL**). CIL is an effect observed in cell assays; as the cells become more crowded, their individual speeds decrease [48]. Although both of these systems are described by the Toner-Tu equations (1.1), they occupy very different locations in parameter space as we demonstrate in Section 2.5.2. As a result they behave in vastly different ways. For further explanation, and the unexpected outcomes of our simulations, see Chapter 3.

Despite the differences between the systems, we achieved them in a similar manner. Ultimately we make just two adjustments to the method already described, the crucial change being that we replace the equilibrium distribution f_i^{eq} with that of our choosing which generates the system of interest. We will denote this new steady state distribution as f_i^{SS} in order to differentiate the two. The second change was to include stochastic fluctuations into the

evolution equation. Therefore our discretised Boltzmann equation is now

$$f_i(t+\Delta t, \mathbf{r}+c\mathbf{e}_i\Delta t) - f_i(t,\mathbf{r}) = -\frac{1}{\tau}\left[f_i(t,\mathbf{r}) - f_i^{\mathrm{SS}}(t,\mathbf{r})\right] + \eta_i(t,\mathbf{r}) \ , \quad (2.18)$$

where τ is a relaxation parameter as before, and

$$\eta_i(t,\mathbf{r}) = \tilde{\eta}_i(t,\mathbf{r}) - \frac{1}{7}\sum_{i=0}^{6}\tilde{\eta}_i(t,\mathbf{r}) \ , \quad (2.19)$$

where $\tilde{\eta}_i$ are temporally and spatially uncorrelated random variables uniformly distributed in the interval $[-\sigma,\sigma]$. Note that this particular choice of noise alters the local velocity, but Eq. (2.19) ensures that the density is conserved. It is possible for one or more of the f_i values to become negative after adding this noise. This is not permitted, hence we immediately correct this using the following procedure at each lattice site.

Negative correction procedure:

1. If $f_0 < 0$, simply set $f_0 = 0$.
2. If $f_i < 0$ for $i > 0$, then take j, such that $\mathbf{e}_j$ is the reverse direction of $\mathbf{e}_i$ ($1 \leftrightarrow 4, 2 \leftrightarrow 5, 3 \leftrightarrow 6$), and add $|f_i|$ to f_j, then set $f_i = 0$.
3. By now $f_i \geq 0$ for all i, however it is possible that the density has changed. This is corrected by rescaling

$$f_i \mapsto \frac{\rho}{\sum_j f_j} f_i \ . \quad (2.20)$$

As was established earlier, in the standard LBM f_i^{eq} is constructed so as to satisfy the moments in Eq. (2.5). The first two conditions in Eq. (2.5) ensure that the collision operation preserves mass and momentum respectively. Therefore built into the system are conservation of mass and conservation of momentum, both of which are key symmetries in the NS equations. When this is considered in conjunction with the isotropy of the lattice itself, it is of little surprise that this system generates the behaviour of the NS equations in the hydrodynamic limit with almost all of the necessary symmetries fulfilled.

The remaining symmetries are ensured by the third moment in Eq. (2.5). Hence through considering symmetries alone one can almost deduce the final equations. See Section 2.5.1 for a rigorous derivation of NS from LBM.

Active systems do not respect the same symmetries as Navier-Stokes. The crucial difference between active particles and passive particles is that active particles can generate local propulsive forces. As a result, spontaneous motion can develop, resulting in a violation of momentum conservation.

Therefore in order to model dry active matter in a LBM, we choose f_i^{SS} such that density is conserved, but that momentum is not. In fact we chose f_i^{SS} to maintain the form of f_i^{eq} so that

$$f_i^{\mathrm{SS}} = w_i \rho \left[1 + 4\frac{\mathbf{e}_i \cdot \mathbf{u}^*}{c} + 8\frac{(\mathbf{e}_i \cdot \mathbf{u}^*)^2}{c^2} - 2\frac{|\mathbf{u}^*|^2}{c^2} \right] , \tag{2.21}$$

where $\mathbf{u}$ has been replaced by $\mathbf{u}^*$. The weights w_i are as before. This automatically ensures that the density ρ is preserved, but the momentum is dictated by what we choose the steady state velocity field $\mathbf{u}^*$ to be. This also explains our choice of noise in Eq. (2.19). Any rotationally invariant noise will suffice so long as it preserves density. There is no need to seek a momentum balancing noise since momentum is not conserved anyway.

Due to both the noise and the replacement of $\mathbf{u} \mapsto \mathbf{u}^*$ in f_i^{SS}, it is possible that

$$f_i(t, \mathbf{r}) - \frac{1}{\tau}\left[f_i(t, \mathbf{r}) - f_i^{\mathrm{SS}}(t, \mathbf{r}) \right] < 0 , \tag{2.22}$$

when $\tau < 1$, even if $f_i > 0$ for all i. Therefore to ensure that no values become negative, we only use $\tau \geq 1$. Different values of τ were tested for the models described below. Results were qualitatively similar to those described in Chapter 3, however if τ is too close to 1 in the MIPS model, the nature of the lattice has too strong an effect, with unrealistic hexagonal structures forming. As mentioned previously, the value of τ is proportional to the viscosity ν. As the viscosity is not the focus of this thesis we maintain $1 \leq \tau \leq 2$.

For our algorithm to be consistent with Eq. (2.18), we must add the noise after the collision step. Our algorithm is now given by

Active LBM algorithm:

1. **Streaming step:**

$$f_i'(\mathbf{r} + c\mathbf{e}_i\Delta t) = f_i(\mathbf{r}) \ . \tag{2.23}$$

2. **Calculate macroscopic ρ and u:**

$$\rho = \sum_{i=0}^{Q-1} f_i' \ , \qquad \rho\mathbf{u} = \sum_{i=0}^{Q-1} f_i' c\mathbf{e}_i \ . \tag{2.24}$$

3. **Calculate $\mathbf{u}^*$:** This step is model dependent. In our MIPS and CIL models, $\mathbf{u}^*$ is a function of ρ and $\mathbf{u}$, as calculated in step 2. Future models may be more elaborate.

4. **Calculate steady state distribution f_i^{SS}:**
For the D2Q7 model,

$$f_i^{\mathrm{SS}} = w_i\rho\left[1 + 4\frac{\mathbf{e}_i\cdot\mathbf{u}^*}{c} + 8\frac{(\mathbf{e}_i\cdot\mathbf{u}^*)^2}{c^2} - 2\frac{|\mathbf{u}^*|^2}{c^2}\right] \ . \tag{2.25}$$

5. **Collision step:**

$$f_i = f_i' - \frac{1}{\tau}\left(f_i' - f_i^{\mathrm{SS}}\right) \ . \tag{2.26}$$

6. **Add noise:**

$$f_i \mapsto f_i + \eta_i \ , \tag{2.27}$$

where η_i is given by Eq. (2.19).

7. **Negative correction procedure:** As described earlier, we amend f_i so that $f_i \geq 0$.

The choice of $\mathbf{u}^*$ determines which active system is described. As such this is where our MIPS and CIL models differ.

2.4.1 Motility-induced phase separation

Motility-induced phase separation is exhibited by several different types of active particles, such as run-and-tumble particles and active Brownian particles. Though the exact mechanism by which MIPS arises is different in each system, certain properties are shared. Both types of particle self-propagate with some persistency to their directions, interactions with their neighbours cause them to slow down, and particles congregate in areas where they are slow moving. These are the key ingredients required to generate MIPS. As our model is already coarse-grained we do not specify which system we are recreating, and simply present a general model that exhibits MIPS. In fact, it has been shown that the coarse-grained dynamics for active Brownian particles and run-and-tumble particles are equivalent if the orientation rates and swim speeds do not depend on the swimming direction [34]. This is the case for our system, hence we do not make a distinction between the two systems, and adopt a notation consistent with the LBM.

We use the following definition for our steady state velocity $\mathbf{u}^*$,

$$\mathbf{u}^* = \begin{cases} C\left(1 - \frac{\rho}{\rho^*}\right)\nabla\rho & \text{if } \rho < \rho^* \\ 0 & \text{otherwise} \end{cases} , \tag{2.28}$$

where C is a positive constant, dictating the sensitivity of the system to density gradients. The parameter ρ^* acts as an upper bound for the local density as permitted by the system; above this there is no net flow, regardless of density gradients, hence the density cannot rise further. As we established earlier, the LBM only works for small speeds, however it is not obvious *a priori* how large the values of $\nabla\rho$ will be. Hence for stability purposes we include a precautionary step in our algorithm, where, if need be, we reduce the magnitude of the velocity to a prespecified $U_{\max}$. Explicitly

$$|\mathbf{u}^*| \mapsto \min\left(|\mathbf{u}^*|,\ U_{\max}\right) . \tag{2.29}$$

The standard LBM does not typically feature gradients. Indeed, apart from the streaming step, all of the calculations and operations are strictly

localised to each lattice site. To calculate a gradient we must include information from neighbouring nodes. We do so by incorporating a finite difference procedure into the routine [121]. It is important to use a finite difference stencil which is isotropic when projected to the lattice. A suitable choice is given by

$$\nabla\rho = A\left[(\rho_1 - \rho_4)\mathbf{e}_1 + (\rho_2 - \rho_5)\mathbf{e}_2 + (\rho_3 - \rho_6)\mathbf{e}_3\right] \ , \tag{2.30}$$

for $A = 1/(3\Delta x)$, where in this notation $\rho_i = \rho(t, \mathbf{r} + \Delta x \mathbf{e}_i)$ [121]. The resulting stencils are

$$\frac{\partial\rho_0}{\partial x} = \frac{2(\rho_1 - \rho_4) + (\rho_2 + \rho_6) - (\rho_3 + \rho_5)}{6\Delta x}, \tag{2.31}$$

$$\frac{\partial\rho_0}{\partial y} = \frac{(\rho_2 + \rho_3) - (\rho_5 + \rho_6)}{4\Delta y} \ . \tag{2.32}$$

We motivate the expression in Eq. (2.28) firstly by intuition, and secondly through comparison with other studies. For our system to experience MIPS the speed of particles must decrease in regions of high density. The speeds of individual particles do not feature in our system, as $\mathbf{u}^*$ is a macroscopic variable. However, a consequence of all particles' speeds decreasing is that the net speed $|\mathbf{u}^*|$ will also decrease. This is clearly achieved by the term $(1 - \rho/\rho^*)$, with the net speed hitting zero altogether for $\rho \geq \rho^*$. Physical systems of hard particles have an upper limit as to how tightly they can be packed, hence it is natural to have a maximum density ρ^*. In Chapter 1, we established that there is no alignment mechanism in a MIPS model, and that directions of particles are typically random and isotropic. This raises a question as to how we can have a non-zero net flow at all. The answer comes in the form of a statistical average. Consider a fixed point in space and assume that there exists a persistent density gradient in a fixed direction. As they are heading into a region of higher density, particles moving in that direction will be impeded more than particles moving in any other direction. Within a short time the non-impeded particles have left the vicinity, whilst the impeded particles remain. As the time span was short, most of these particles will have maintained their current direction, due to our persistency assumption. As a result there is a net flow towards regions of higher density.

This is also consistent with the observation that particles will congregate in areas of lower speeds or, equivalently, higher densities; we expect there to be a flow towards those regions.

We can also arrive at the expression in Eq. (2.28) through comparison with previous studies in the field. For a system of non-interacting active particles propagating with fixed speed $v(\mathbf{r})$, and orientational relaxation time $\tau(\mathbf{r})$, where v and τ can vary in space, it has been shown that the macroscopic density obeys the following

$$\frac{\partial \rho}{\partial t} = -\nabla \cdot \mathbf{J} \ , \tag{2.33a}$$

$$\mathbf{J} = -D\nabla\rho + \mathbf{V}\rho + \sqrt{2D\rho}\Lambda \ , \tag{2.33b}$$

where $\mathbf{V}$ is a drift velocity, D is a diffusivity, and Λ is a white noise [16]. With negligible translational diffusivity these can be expressed as

$$D = \frac{v^2\tau}{d} \ , \tag{2.34}$$

$$\frac{\mathbf{V}}{D} = -\nabla \log v \ , \tag{2.35}$$

where d is the dimension. Generalising this system to include interaction effects, allows v and τ to now depend on the local density ρ, as well as $\mathbf{r}$. By extension so do D and $\mathbf{V}$. For simplicity we assume τ to be constant and v to depend only on ρ. Numerical studies of active Brownian particles have shown that the effective speed has an approximately linear dependence on the density [33, 54, 57, 58]. Hence we adopt

$$v(\rho) = v_0 \left(1 - \frac{\rho}{\rho^*}\right) \ . \tag{2.36}$$

The drift velocity $\mathbf{V}$ becomes

$$\mathbf{V} = \frac{\tau v_0^2}{\rho^* d} \left(1 - \frac{\rho}{\rho^*}\right) \nabla\rho \ . \tag{2.37}$$

Finally we observe that Eq. (2.33a) is a continuity equation and equate

$\mathbf{J} \equiv \rho\mathbf{u}$ in our system. We take the drift velocity to be the steady state that $\mathbf{u}$ tends towards, that is $\mathbf{V} \equiv \mathbf{u}^*$. The term $D\nabla\rho$ features in our model as the pressure term in our hydrodynamic equations, as can be seen in Section 2.5.2, and of course we also have noise. Our system is very similar to that presented in Eq. (2.33), albeit our velocity $\mathbf{u}$ is dynamic, whilst $\mathbf{J}$ has no time dependence. In that sense, Eq. (2.33) is the overdamped version of our model.

2.4.2 Alignment with contact inhibition of locomotion

In the model described in the previous section, the net flow of matter was largely determined by the gradient of the density field. In a periodic system, this means that a steady state cannot have a constant unidirectional flow, nor homogeneous polar order, as either of these would require the density field to be endlessly growing in a particular direction. This lack of collective motion is to be expected since the active systems on which the model is based have no mechanism for their active particles to align their velocities.

In this section we consider an alternative model with an alignment mechanism. Explicitly we attempt to produce the collective behaviour of two dimensional dry active polar particles with the following characteristics:

- nearby particles align their velocities in the local net direction of motion
- there is no preferred direction of motion
- particles propel themselves to move at the same fixed speed
- high densities impede the mobility of the particles

The first three of these are very common from previous studies of collective motion, with local alignment occurring by assumption, such as in toy models like the Vicsek model, or through two (or more) body collisions [44, 50, 51, 62, 66]. These studied the minimum requirements for collective motion to emerge from local interactions. The third assumption is a common theme in dry active matter; local momentum is not conserved with propulsion usually

generated through an interaction with a fixed substrate, from cells crawling on a surface to wildebeest running on a plain.

The final assumption is a phenomenon observed in wound healing experiments; epithelial cells propagate around a growing sheet of tissue, but their motion gradually decreases as the density increases, effectively stopping entirely as the sheet reaches confluence [48]. This relationship between local speeds and density is generally known as contact inhibition of locomotion (CIL), although the exact reason it occurs between epithelial cells is debated [122]. Regardless of why it occurs in cells the effect can be witnessed in many other systems of collectively moving bodies with volume exclusion, such as people walking down a crowded corridor, and most famously in traffic flow [123, 124].

To encapsulate these into the model we take

$$\mathbf{u}^* = U_0(\rho)\frac{\mathbf{u}}{|\mathbf{u}|} \ , \tag{2.38}$$

where U_0 is a predetermined local mesoscopic speed, which may be density-dependent. This expression amounts to accelerating or decelerating the fluid without changing the instantaneous local direction, although it should be considered in the context of particles reorienting to align with the net direction, as opposed to particles speeding up or slowing down.

CIL is included by choosing U_0 to be a decreasing function of density; we use

$$U_0(\rho) = \begin{cases} -A\rho^2 + B & \text{if } B \geq A\rho^2 \\ 0 & \text{otherwise} \end{cases} \tag{2.39}$$

where A and B are positive constants. We do not allow U_0 to become negative; as in wound healing assays, we assume collective motion ceases if the density is high enough.

In violating conservation of momentum, our system is necessarily not equivalent to the Navier-Stokes equations. By imposing a fixed particle speed we have also lost Galilean invariance, as this speed is specific to the rest frame of the substrate. As a result we are in the realm of the Toner-Tu

equations [40, 41]. In Section 2.5.2 we demonstrate this using Chapman-Enskog analysis.

2.5 Relationship to hydrodynamic equations

2.5.1 Recovery of the Navier-Stokes equations

Sydney Chapman and David Enskog introduced a multiscaling method to derive a hydrodynamic description from a microscopic Boltzmann equation. Given that the lattice Boltzmann method can be viewed as a discretisation of the continuous Boltzmann equation, by extension the same conclusions apply to the hydrodynamics of the LBM [98]. Alternatively the asymptotic techniques can be directly applied to the lattice Boltzmann equation, as we will demonstrate here.

There is no consensus on how Chapman-Enskog analysis should be implemented, however all of the derivations share a common theme, namely f_i is asymptotically expanded about the equilibrium distribution f_i^{eq} by a small perturbation parameter ε and various orders of the expansion are matched to give a hierarchy of equations. What the small parameter ε represents varies between studies. Some studies take Δt as ε, justified by the fact that a discretised differential equation must be evolved in small time increments to be valid. However, strictly speaking this should be $\varepsilon = \Delta t/T$ where T is a typical time scale of the system, since the definition of the lattice Boltzmann equation permits arbitrary rescaling of t. Other methods use the Knudsen number as ε. This is a dimensionless parameter comparing the microscopic length scales with the length scales of the system, and is often referenced when discussing the validity of a continuum assumption in fluid mechanics or other statistical mechanics formulations. Typically it is defined as the mean free path divided by a representative length scale. In lattice Boltzmann systems terms the mean free path is simply Δx, as this is the distance travelled between collision evaluations. Hence ε would be equal to $1/N$ where N is the number of nodes spanning a typical length in the system.

Of course, Δx and Δt are explicitly linked by $c = \Delta x/\Delta t$, which per-

haps explains why both methods arrive at the same conclusion, and either formulation is valid.

Presented here is the analysis using $\varepsilon = \Delta t$, which is assumed to be small, as given by [99].

To begin, we introduce Chapman-Enskog (asymptotic) expansions

$$f_i = \sum_{n=0} \varepsilon^n f_i^{(n)} = f_i^{(0)} + \epsilon f_i^{(1)} + \epsilon^2 f_i^{(2)} + ... \ , \tag{2.40}$$

where $\epsilon = \Delta t$. Note that the index in brackets does not indicate a derivative. We also need to expand the time derivative across multiple scales,

$$\partial_t = \sum_{n=0} \varepsilon^n \partial_{t_n} = \partial_{t_0} + \varepsilon \partial_{t_1} + \varepsilon^2 \partial_{t_2} + ... \ , \tag{2.41}$$

so $\partial f / \partial t_1$ measures variation that occurs on time scales $1/\varepsilon$. Finally we take a Taylor expansion of the first term in Eq. (2.4)

$$f_i(\mathbf{x} + \mathbf{e}_i c\Delta t, t + \Delta t) = \sum_{n=0} \frac{\varepsilon^n}{n!} D_t^n f_i(\mathbf{x}, t) \ , \tag{2.42}$$

where $D_t = (\partial_t + c\mathbf{e}_i \cdot \nabla)$ so the LHS becomes

$$f_i(\mathbf{x} + \mathbf{e}_i c\Delta t, t + \Delta t) - f_i(\mathbf{x}, t) = \sum_{n=0} \frac{\varepsilon^n}{n!} D_t^n f_i(\mathbf{x}, t) - f_i(\mathbf{x}, t) \tag{2.43}$$

$$= \sum_{n=1} \frac{\varepsilon^n}{n!} D_t^n f_i \tag{2.44}$$

$$= \varepsilon D_t^1 f_i + \frac{\varepsilon^2}{2} D_t^2 f_i + O(\varepsilon^3) \ . \tag{2.45}$$

Inserting the asymptotic expansions into Eq. (2.4), and truncating to $O(\varepsilon^2)$

this becomes

$$\varepsilon(\partial_{t_0}+\varepsilon\partial_{t_1} + c\mathbf{e}_i \cdot \nabla)\left(f_i^{(0)} + \varepsilon f_i^{(1)}\right) + \frac{\varepsilon^2}{2}\left(\partial_{t_0} + c\mathbf{e}_i \cdot \nabla\right)^2 f_i^{(0)} + O(\varepsilon^3) \quad (2.46)$$

$$\begin{aligned} &= \varepsilon\left[\left(\partial_{t_0} + c\mathbf{e}_i \cdot \nabla\right) f_i^{(0)}\right] \\ &\quad + \varepsilon^2\left[\partial_{t_1} f_i^{(0)} + \left(\partial_{t_0} + c\mathbf{e}_i \cdot \nabla\right) f_i^{(1)} + \frac{1}{2}\left(\partial_{t_0} + c\mathbf{e}_i \cdot \nabla\right)^2 f_i^{(0)}\right] \\ &\quad + O(\varepsilon^3)\ . \end{aligned} \quad (2.47)$$

The RHS is simply

$$-\frac{1}{\tau}\left(\left[f_i^{(0)} - f_i^{\mathrm{eq}}\right] + \varepsilon f_i^{(1)} + \varepsilon^2 f_i^{(2)} + O(\varepsilon^3)\right)\ . \quad (2.48)$$

Matching the orders we obtain

$$O(\varepsilon^0): \qquad f_i^{(0)} = f_i^{\mathrm{eq}}\ , \quad (2.49)$$

$$O(\varepsilon^1): \qquad D_{t_0} f_i^{(0)} = -\frac{f_i^{(1)}}{\tau}\ , \quad (2.50)$$

$$O(\varepsilon^2): \qquad \partial_{t_1} f_i^{(0)} + D_{t_0} f_i^{(1)} + \frac{1}{2} D_{t_0}^2 f_i^{(0)} = -\frac{f_i^{(2)}}{\tau}\ , \quad (2.51)$$

where $D_{t_m} = \partial_{t_m} + c\mathbf{e}_i \cdot \nabla$.

Using Eq. (2.50), we can rewrite Eq. (2.51) as

$$\partial_{t_1} f_i^{(0)} + \left(1 - \frac{1}{2\tau}\right) D_{t_0} f_i^{(1)} = -\frac{f_i^{(2)}}{\tau}. \quad (2.52)$$

From Eq. (2.49) and the definition of f_i^{eq} we now know that

$$\sum_{i=0}^{Q-1} f_i^{(0)} = \rho\ , \quad (2.53)$$

$$\sum_{i=0}^{Q-1} c f_i^{(0)} \mathbf{e}_i = \rho\mathbf{u}\ , \quad (2.54)$$

meaning

$$\sum_{i=0}^{Q-1} f_i^{(k)} = 0 \ , \tag{2.55}$$

$$\sum_{i=0}^{Q-1} c f_i^{(k)} \mathbf{e}_i = \mathbf{0} \ , \tag{2.56}$$

for $k \geq 1$.

From here, we essentially arrive at the result by summing over various moments of Eq. (2.50) and Eq. (2.52) using the identities above, coupled with some tensor identities specific to the lattice.

Summing Eq. (2.50)

$$\sum_{i=0}^{Q-1} D_{t_0} f_i^{(0)} = \sum_{i=0}^{Q-1} \partial_{t_0} f_i^{(0)} + \sum_{i=0}^{Q-1} c\mathbf{e}_i \cdot \nabla f_i^{(0)} \tag{2.57}$$

$$= \partial_{t_0} \sum_{i=0}^{Q-1} f_i^{(0)} + \sum_{i=0}^{Q-1} \nabla \cdot (c\mathbf{e}_i f_i^{(0)}) \tag{2.58}$$

$$= \partial_{t_0} \sum_{i=0}^{Q-1} f_i^{(0)} + \nabla \cdot \sum_{i=0}^{Q-1} c\mathbf{e}_i f_i^{(0)} \tag{2.59}$$

$$= \partial_{t_0} \rho + \nabla \cdot (\rho \mathbf{u}) \tag{2.60}$$

$$= -\frac{1}{\tau} \sum_{i=0}^{Q-1} f_i^{(1)} = 0 \ , \tag{2.61}$$

where we have used the identity

$$\nabla \cdot (\psi \mathbf{A}) = \psi \left(\nabla \cdot \mathbf{A} \right) + \mathbf{A} \cdot (\nabla \psi) \ , \tag{2.62}$$

the linearity of $\nabla \cdot$ and the fact that $\mathbf{e}_i$ is a constant vector for all i.

Similarly, summing over the first moment of Eq. (2.50) leads to

$$\sum_{i=0}^{Q-1} c\mathbf{e}_i D_{t_0} f_i^{(0)} = \sum_{i=0}^{Q-1} c\mathbf{e}_i \partial_{t_0} f_i^{(0)} + \sum_{i=0}^{Q-1} c\mathbf{e}_i \left(c\mathbf{e}_i \cdot \nabla f_i^{(0)} \right) \tag{2.63}$$

$$= \partial_{t_0} \sum_{i=0}^{Q-1} c\mathbf{e}_i f_i^{(0)} + \sum_{i=0}^{Q-1} c\mathbf{e}_i \nabla \cdot \left(c\mathbf{e}_i f_i^{(0)} \right) \tag{2.64}$$

$$= \partial_{t_0} \sum_{i=0}^{Q-1} c\mathbf{e}_i f_i^{(0)} + \nabla \cdot \sum_{i=0}^{Q-1} c^2 \mathbf{e}_i \mathbf{e}_i f_i^{(0)} \tag{2.65}$$

$$= \partial_{t_0} (\rho \mathbf{u}) + \nabla \cdot \Pi^{(0)} \tag{2.66}$$

$$= -\frac{1}{\tau} \sum_{i=0}^{Q-1} c\mathbf{e}_i f_i^{(1)} = \mathbf{0} \ , \tag{2.67}$$

where

$$\Pi^{(0)} = \sum_{i=0}^{Q-1} c^2 f_i^{(0)} \mathbf{e}_i \mathbf{e}_i \tag{2.68}$$

$$= \rho \mathbf{u}\mathbf{u} + PI \ , \tag{2.69}$$

and $P = c_s^2 \rho$ is a pressure term. As mentioned previously c_s is a lattice dependent quantity, in fact, as a result of this specific summation. Substituting the respective definitions of f_i^{eq} into this summation gives $c_s = c/\sqrt{3}$ in the D2Q9 model , whilst $c_s = c/2$ in the D2Q7 model.

In summary, thus far

$$\partial_{t_0} \rho + \nabla \cdot (\rho \mathbf{u}) = 0 \ , \tag{2.70}$$

$$\partial_{t_0} (\rho \mathbf{u}) + \nabla \cdot \Pi^{(0)} = 0 \ , \tag{2.71}$$

which we recognise as the Euler equations; the Navier-Stokes equations in the limit of zero viscosity.

Now we do the same for Eq. (2.52). Summing the zeroth moment.

$$\sum_{i=0}^{Q-1} \partial_{t_1} f_i^{(0)} + \left(1 - \frac{1}{2\tau}\right) D_{t_0} f_i^{(1)} \tag{2.72}$$

$$= \partial_{t_1} \sum_{i=0}^{Q-1} f_i^{(0)} + \left(1 - \frac{1}{2\tau}\right) \sum_{i=0}^{Q-1} \left(\partial_{t_0} + c\mathbf{e}_i \cdot \nabla\right) f_i^{(1)} \tag{2.73}$$

$$= \partial_{t_1} \rho + \left(1 - \frac{1}{2\tau}\right) \left(\partial_{t_0} \cancel{\sum_{i=0}^{Q-1} f_i^{(1)}} + \nabla \cdot \cancel{\sum_{i=0}^{Q-1} c\mathbf{e}_i f_i^{(1)}}\right) \tag{2.74}$$

$$= \partial_{t_1} \rho \tag{2.75}$$

$$= -\frac{1}{\tau} \sum_{i=0}^{Q-1} f_i^{(2)} = 0 \ . \tag{2.76}$$

And the first moment

$$\sum_{i=0}^{Q-1} c\mathbf{e}_i \partial_{t_1} f_i^{(0)} + \left(1 - \frac{1}{2\tau}\right) c\mathbf{e}_i D_{t_0} f_i^{(1)} \tag{2.77}$$

$$= \partial_{t_1} \sum_{i=0}^{Q-1} c\mathbf{e}_i f_i^{(0)} + \left(1 - \frac{1}{2\tau}\right) \sum_{i=0}^{Q-1} c\mathbf{e}_i \left(\partial_{t_0} + c\mathbf{e}_i \cdot \nabla\right) f_i^{(1)} \tag{2.78}$$

$$= \partial_{t_1} (\rho \mathbf{u}) + \left(1 - \frac{1}{2\tau}\right) \left(\partial_{t_0} \cancel{\sum_{i=0}^{Q-1} c\mathbf{e}_i f_i^{(1)}} + \nabla \cdot \sum_{i=0}^{Q-1} c^2 \mathbf{e}_i \mathbf{e}_i f_i^{(1)}\right) \tag{2.79}$$

$$= \partial_{t_1} (\rho \mathbf{u}) + \left(1 - \frac{1}{2\tau}\right) \nabla \cdot \Pi^{(1)} \tag{2.80}$$

$$= -\frac{1}{\tau} \sum_{i=0}^{Q-1} f_i^{(2)} c\mathbf{e}_i = \mathbf{0} \ , \tag{2.81}$$

where $\Pi^{(1)} = \sum_{i=0}^{Q-1} c^2 \mathbf{e}_i \mathbf{e}_i f_i^{(1)}$.

Now we have to calculate Π^1 explicitly.

$$\Pi^{(1)} = \sum_{i=0}^{Q-1} c^2 \mathbf{e}_i \mathbf{e}_i f_i^{(1)} \tag{2.82}$$

$$= -\tau \sum_{i=0}^{Q-1} c^2 \mathbf{e}_i \mathbf{e}_i D_{t_0} f_i^{(0)} \tag{2.83}$$

$$= -\tau \sum_{i=0}^{Q-1} \left[\partial_{t_0} c^2 \mathbf{e}_i \mathbf{e}_i f_i^{(0)} + \nabla \cdot c^3 \mathbf{e}_i \mathbf{e}_i \mathbf{e}_i f_i^{(0)} \right] \tag{2.84}$$

$$= -\tau \left[\partial_{t_0} \Pi^{(0)} + \nabla \cdot \Gamma \right] \ , \tag{2.85}$$

where $\Gamma = \sum_{i=0}^{Q-1} c^3 \mathbf{e}_i \mathbf{e}_i \mathbf{e}_i f_i^{(0)}$.

In index notation

$$\Gamma_{\alpha\beta\gamma} = c_s^2 \rho \left(\delta_{\alpha\beta} u_\gamma + \delta_{\alpha\gamma} u_\beta + \delta_{\beta\gamma} u_\alpha \right) \ , \tag{2.86}$$

where c_s is again the lattice dependent speed of sound.

$$\Pi_{ij}^{(1)} = -\tau \left(\partial_{t_0} \Pi_{ij}^{(0)} + \nabla_k \cdot \Gamma_{ijk} \right) \tag{2.87}$$

$$= -\tau \left(\partial_{t_0} (\rho u_i u_j + c_s^2 \rho \delta_{ij}) + c_s^2 \left[\delta_{ij} \partial_k (\rho u_k) + \partial_i (\rho u_j) + \partial_j (\rho u_i) \right] \right) \tag{2.88}$$

$$= -\tau \left(\partial_{t_0} (\rho u_i u_j) + c_s^2 \left[\partial_i (\rho u_j) + \partial_j (\rho u_i) \right] \right) \ . \tag{2.89}$$

The time derivative can be eliminated by making use of the Euler continuity and momentum equations

$$\partial_{t_0} (\rho u_i u_j) = u_i u_j \partial_{t_0} (\rho) + \rho u_i \partial_{t_0} (u_j) + \rho u_j \partial_{t_0} (u_i) \tag{2.90}$$

$$\begin{aligned} &= u_i u_j \partial_k (\rho u_k) - \partial_k (\rho u_i u_k) u_j - u_i \partial_k (\rho u_j u_k) \\ &\quad - c_s^2 (\partial_i \rho) u_j - c_s^2 u_i (\partial_j \rho) \ . \end{aligned} \tag{2.91}$$

Ignoring terms of $O(u^3)$, valid by the low Mach number approximation, leaves

$$\Pi_{ij}^{(1)} = -\tau c_s^2 \rho \left(\partial_i (u_j) + \partial_j (u_i) \right) \ . \tag{2.92}$$

Thus

$$\partial_{t_1}(\rho\mathbf{u}) = -\left(1-\frac{1}{2\tau}\right)\nabla\cdot\Pi^{(1)} = \frac{\nu}{\epsilon}\nabla\cdot\left[\rho\left(\nabla\mathbf{u}+(\nabla\mathbf{u})^T\right)\right] \ , \tag{2.93}$$

where ν is the viscosity given by

$$\nu = \frac{2\tau-1}{2}c_s^2\Delta t \ . \tag{2.94}$$

Note that this definition is lattice dependent due to the presence of c_s and features $\Delta t = \varepsilon$ in its definition.

In order to unite these equations with the Euler equations, we recycle the definition of the full time derivative as $\partial_t = \partial_{t_0} + \varepsilon\partial_{t_1}$ hence the full equations are

$$\frac{\partial\rho}{\partial t} + \nabla\cdot(\rho\mathbf{u}) = 0 + O(M^2) \ , \tag{2.95}$$

$$\frac{\partial(\rho\mathbf{u})}{\partial t} + \nabla\cdot(\rho\mathbf{u}\mathbf{u}) = -\nabla P + \nu\left[\nabla^2(\rho\mathbf{u}) + \nabla(\nabla\cdot(\rho\mathbf{u}))\right] + O(M^3) \ , \tag{2.96}$$

where M is the Mach number, as terms of order $O(\mathbf{u}^3)$ were neglected.

2.5.2 Recovery of the Toner-Tu equations

The analysis for the active fluid model proceeds in much the same way as before, with the key difference being that the values of certain moments have changed. The noise term will be ignored for now and treated in a separate manner in Section 3.2.5. Therefore the governing equation (2.18) is the same as Eq. (2.4) and using the same expansions, equations (2.49),(2.50),(2.51) are as before with $f_i^{\mathrm{eq}} \mapsto f_i^{\mathrm{SS}}$. Recall that f_i^{SS} is simply

$$f_i^{\mathrm{SS}} = f_i^{\mathrm{eq}}\Big|_{\mathbf{u}\mapsto\mathbf{u}^*} \ . \tag{2.97}$$

Summing Eq. 2.49 now leads to

$$\sum_{i=0}^{Q-1} f_i^{(0)} = \sum_{i=0}^{Q-1} f_i^{\mathrm{SS}} = \rho \ , \tag{2.98}$$

$$\sum_{i=0}^{Q-1} c f_i^{(0)} \mathbf{e}_i = \sum_{i=0}^{Q-1} c f_i^{\mathrm{SS}} \mathbf{e}_i = \rho \mathbf{u}^* \ , \tag{2.99}$$

but

$$\sum_{i=0}^{Q-1} f_i = \rho \ , \tag{2.100}$$

$$\sum_{i=0}^{Q-1} c f_i \mathbf{e}_i = \rho \mathbf{u} \neq \rho \mathbf{u}^* \ , \tag{2.101}$$

hence

$$\sum_{i=0}^{Q-1} f_i^{(1)} = 0 \ , \tag{2.102}$$

$$\sum_{i=0}^{Q-1} c f_i^{(1)} \mathbf{e}_i = \rho \frac{\mathbf{u} - \mathbf{u}^*}{\varepsilon} \ . \tag{2.103}$$

Evidently $\rho(\mathbf{u} - \mathbf{u}^*) = O(\varepsilon)$, so $\mathbf{u}$ is assumed to be close to $\mathbf{u}^*$. For all other $k > 1$ we again have

$$\sum_{i=0}^{Q-1} f_i^{(k)} = 0 \tag{2.104}$$

$$\sum_{i=0}^{Q-1} c f_i^{(k)} \mathbf{e}_i = \mathbf{0} \ . \tag{2.105}$$

To naïvely continue from this point would result in some rather cumbersome algebra. The more insightful approach is to realise that the velocity field that the final governing equations will be expressed in terms of is neither $\mathbf{u}$ nor $\mathbf{u}^*$, but something in between. By making this transformation now rather than later greatly simplifies the analysis.

In fact, by expressing our active lattice Boltzmann model in the form of a conventional lattice Boltzmann scheme with a body force term, we can use the results of [125] to derive the macroscopic equations.

Let's introduce the notation

$$\xi_i(\rho, \mathbf{u}) = w_i \rho \left[1 + 4\frac{\mathbf{e}_i \cdot \mathbf{u}}{c} + 8\frac{(\mathbf{e}_i \cdot \mathbf{u})^2}{c^2} - 2\frac{|\mathbf{u}|^2}{c^2} \right] \ . \tag{2.106}$$

Hence in the conventional LBM $f_i^{\mathrm{eq}} = \xi_i(\rho, \mathbf{u})$ and in our active model $f_i^{\mathrm{SS}} = \xi_i(\rho, \mathbf{u}^*)$.

The evolution equation becomes

$$f_i(t + \Delta t, \mathbf{r} + \mathbf{e}_i \Delta t) - f_i(t, \mathbf{r}) = -\frac{1}{\tau} \left[f_i - \xi_i(\rho, \mathbf{u}) \right] + F_i \ , \tag{2.107}$$

where

$$F_i = \frac{1}{\tau} \left[\xi_i(\rho, \mathbf{u}^*) - \xi_i(\rho, \mathbf{u}) \right] \ . \tag{2.108}$$

Note that

$$\sum_{i=0} F_i = 0 \quad , \quad \sum_{i=0} F_i c \mathbf{e}_i = \rho \frac{\mathbf{u}^* - \mathbf{u}}{\tau} = \Delta t \ \mathbf{F} \ . \tag{2.109}$$

As in [125], we define the 'actual velocity' according to

$$\mathbf{v} = \mathbf{u} + \frac{\Delta t \mathbf{F}}{2\rho} = \mathbf{u} - \frac{1}{2\tau} \left(\mathbf{u} - \mathbf{u}^* \right) \ . \tag{2.110}$$

After expressing Eq. 2.107 in terms of the actual velocity,

$$f_i(t + \Delta t, \mathbf{r} + \mathbf{e}_i c \Delta t) - f_i(t, \mathbf{r}) = -\frac{1}{\tau} \left[f_i - \xi_i(\rho, \mathbf{v}) \right] + \tilde{F}_i \ , \tag{2.111}$$

where

$$\tilde{F}_i = F_i + \frac{1}{\tau} \left[\xi_i(\rho, \mathbf{u}) - \xi_i(\rho, \mathbf{v}) \right] = \frac{1}{\tau} \left[\xi_i(\rho, \mathbf{u}^*) - \xi_i(\rho, \mathbf{v}) \right] \ , \tag{2.112}$$

we can now use the results of [125] to determine our macroscopic equations. They are the continuity equation

$$\partial_t \rho + \nabla \cdot (\rho \mathbf{v}) = 0 \ , \tag{2.113}$$

and the momentum equation

$$\partial_t (\rho \mathbf{v}) + \nabla \cdot (\rho \mathbf{v}\mathbf{v}) = -\nabla P + \nabla \cdot \tilde{\Pi} + \mathbf{F} + \nabla \cdot \Theta \ , \tag{2.114}$$

where

$$\tilde{\Pi} = \rho\nu \left(\nabla \mathbf{v} + (\nabla \mathbf{v})^T \right) \ , \tag{2.115}$$

and

$$\Theta = \left(\tau - \frac{1}{2} \right) \Delta t \left(\mathbf{v}\mathbf{F} + \mathbf{F}\mathbf{v} \right) - \tau \sum_i \mathbf{e}_i \mathbf{e}_i \tilde{F}_i \ . \tag{2.116}$$

Note that in deriving this, several $O(\mathbf{u}^3)$ terms have already been ignored, as consistent with a small Mach number assumption. From Eq. (2.112),

$$\tau \sum_i \mathbf{e}_i \mathbf{e}_i \tilde{F}_i = \rho \mathbf{u}^* \mathbf{u}^* - \rho \mathbf{v}\mathbf{v} \ . \tag{2.117}$$

Rearranging Eq. (2.110), we can express $\mathbf{u}$ in terms of $\mathbf{u}^*$ and $\mathbf{v}$,

$$\mathbf{u} = \frac{1}{2\tau - 1} \left(2\tau \mathbf{v} - \mathbf{u}^* \right) \ . \tag{2.118}$$

Thus

$$\mathbf{F} = \frac{\rho}{\tau \Delta t} \left(\mathbf{u}^* - \mathbf{u} \right) = \frac{\rho}{\Delta t} \frac{2}{2\tau - 1} \left(\mathbf{u}^* - \mathbf{v} \right) \ . \tag{2.119}$$

Substituting this into Θ, and factorising gives

$$\Theta = -\rho \left(\mathbf{u}^* - \mathbf{v} \right) \left(\mathbf{u}^* - \mathbf{v} \right) . \tag{2.120}$$

Transferring $\nabla \cdot \Theta$ to the left hand side of the momentum equation, we can see that it relates to the term $\nabla \cdot (\rho \mathbf{v}\mathbf{v})$. However, as $(\mathbf{u}^* - \mathbf{v}) \sim O(\varepsilon)$, we can safely ignore $\nabla \cdot \Theta$, as it is of order $O(\varepsilon^2)$.

Finally, using the continuity equation, we can express the momentum equation as

$$\rho\left(\partial_t \mathbf{v} + \mathbf{v}\cdot\nabla\mathbf{v}\right) = -\nabla P + \nabla\cdot\rho\nu\left(\nabla\mathbf{v} + (\nabla\mathbf{v})^T\right) + \mathbf{F}. \tag{2.121}$$

The analysis so far is valid for both the MIPS and the CIL models. The only difference stems from the choice of $\mathbf{u}^*$ in $\mathbf{F}$.

MIPS model:

For the MIPS model, $\mathbf{u}^*$ depends on the density, with

$$\frac{\mathbf{F}_{\text{MIPS}}}{\rho} = \frac{2}{\Delta t(2\tau-1)}\left(C\left(1-\frac{\rho}{\rho^*}\right)\nabla\rho - \mathbf{v}\right) \ . \tag{2.122}$$

We have divided by ρ because Eq. (2.121) is expressed in terms of $\rho\mathbf{v}$, whereas Eq. (1.1b) is in terms of $\mathbf{u}$. Only one of the terms in Eq. (2.122) depends on $\mathbf{v}$, and it necessarily corresponds to $\alpha\mathbf{u}$ in Eq. (1.1b), with

$$\alpha = -\frac{2}{\Delta t\,(2\tau-1)} \ . \tag{2.123}$$

The expression for α is similar to that of ν in Eq. (2.94), however they are independent variables as ν also depends on the lattice speed c. Since $\alpha < 0$ the velocity decays to a fixed value, which would otherwise be $\mathbf{0}$ if not for the remaining term in $\mathbf{F}_{\text{MIPS}}/\rho$. Since $\nabla P = c_s^2\nabla\rho$, this is effectively an unusual pressure term where the coefficient varies with density. The key aspect is that for $\rho < \rho_*$ the coefficient is positive. Hence this pressure acts in the opposite direction from the conventional pressure term. Instead of material flowing away from areas of high density (pressure), material flows towards them. In summary, the macroscopic velocity $\mathbf{v}$ decays to a value predominantly determined by a balance between the density term in $\mathbf{F}_{\text{MIPS}}/\rho$, the standard pressure term ∇P, and the noise, which we have not included in the Chapman-Enskog analysis. This is consistent with the model in Eq. (2.33); this same balance is described in the definition of $\mathbf{J}$.

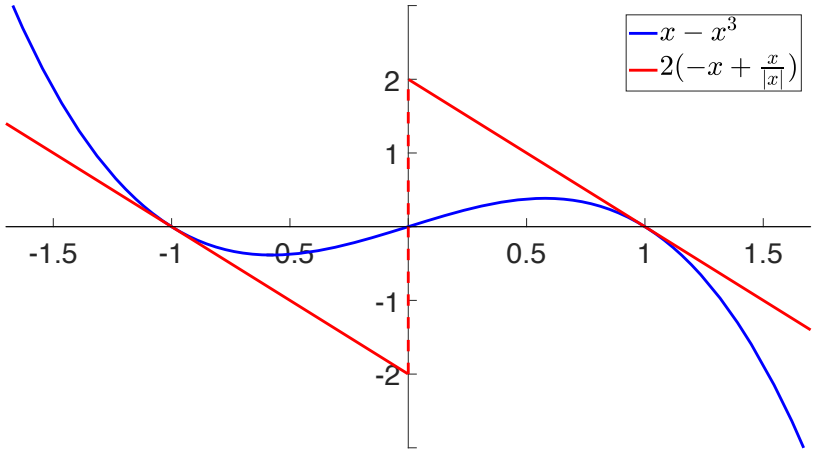

Figure 2.3: Comparing the form of the momentum generating term from the Toner-Tu equations (blue) with the version from the LBM derivation (red). The latter is a linearisation of the former.

CIL model:

As for the CIL model we use the fact that $\mathbf{u}$, $\mathbf{u}^*$ and $\mathbf{v}$ are parallel vectors to express $\mathbf{u}^*$ in terms of $\mathbf{v}$ and U_0 by

$$\mathbf{u}^* = U_0 \frac{\mathbf{u}}{|\mathbf{u}|} = U_0 \frac{\mathbf{v}}{|\mathbf{v}|} \ . \tag{2.124}$$

Thus

$$\frac{\mathbf{F}_{\mathrm{CIL}}}{\rho} = \frac{2}{\Delta t(2\tau - 1)} \left(U_0 \frac{\mathbf{v}}{|\mathbf{v}|} - \mathbf{v} \right) \ . \tag{2.125}$$

$\mathbf{F}_{\mathrm{CIL}}/\rho$ corresponds to a linearised version of $[\alpha(\rho) - \beta|\mathbf{u}|^2]\,\mathbf{u}$ in Eq. (1.1b), where the linearisation has occurred about the stationary points $|\mathbf{u}| = \sqrt{\alpha/\beta}$ The linearisation is visualised in Fig. 2.3. Matching the terms gives

$$\alpha = \frac{1}{\Delta t\,(2\tau - 1)} \quad , \quad \beta = \frac{\alpha}{U_0^2} \ . \tag{2.126}$$

These are not well defined when $U_0 = 0$. In this case

$$\frac{\mathbf{F}_{\mathrm{CIL}}}{\rho} = -\frac{2}{\Delta t(2\tau - 1)}\mathbf{v} \ , \tag{2.127}$$

From this we can deduce nothing about β, but conclude that

$$\alpha = -\frac{2}{\Delta t\,(2\tau - 1)} \ , \tag{2.128}$$

as in the MIPS model. These values of α are consistent with the claim that $\alpha\mathbf{u}$ is a driving force; $\alpha > 0$ gives a non-zero flow U_0, whereas if $\alpha < 0$ flow will decay to $\mathbf{u} = \mathbf{0}$.

We stress here that both systems are versions of the Toner-Tu equations, albeit with very different coefficients. As such the overall behaviour is not the same, as we demonstrate in Chapter 3.

Chapter 3

Applications to dry active matter

In Chapter 2 we introduced the lattice Boltzmann method for simulating the Navier-Stokes equations, along with the modifications we implemented to adapt the system to describe dry active matter. In this chapter we present the results obtained for two different systems: a model that exhibits motility-induced phase separation (MIPS), and an active fluid with an alignment mechanism combined with contact inhibition of locomotion (CIL). In particular, we are able to construct phase diagrams by varying the system parameters. Most interestingly we uncover several new phase transitions in the CIL model, including a potentially novel critical transition.

3.1 Motility-induced phase separation

3.1.1 System setup

As established in the previous chapter, the modifications made to the lattice Boltzmann method renders our new system in the realm of the Toner-Tu equations, and we expect it to behave like a dry active fluid. As such, we simulate our system in a simple rectangular geometry with periodic boundary conditions, and observe the behaviour over a range of parameter values. Since the system is active, we do not need to apply any external forces in order to

drive the system out of equilibrium, hence periodic boundary conditions suffice for this study. We deliberately adopt a non-unitary aspect ratio. Doing so reduces the number of possible configurations for certain steady states, and therefore aids our data collection. Specifically, in the event of phase separation, the two phases adopt a topology that minimizes their effective surface tension, hence they will predictably form strips running along the shortest length of the rectangular domain, in this case the vertical axis (Fig. 3.1(d)). We use this predictability to our advantage during data collection, as the system can be safely averaged over the y-direction whilst preserving the information of interest. Note that this is a geometrical consideration and no external fields have been applied. We expect that solid boundaries could be implemented using the standard techniques for LBMs, such as the 'bounce-back' method [87]. The effects of boundaries on the flow would certainly be worth studying in the future, though they are not investigated here.

In the results presented here only the mean density $\bar{\rho}$ and the noise strength are varied, with all other parameters fixed and presented in Table 3.1.

Parameter	Value
τ	2
C	50
ρ_*	0.2
Δx	1
$U_{\max}$	0.3
c	1

Table 3.1: Parameters used to obtain the results depicted in Fig. 3.1, Fig. 3.3 and Fig. 3.4. Values are non-dimensional.

3.1.2 Typical behaviour

To demonstrate the typical behaviour we used a system of 180×60 nodes. The system measurements were therefore $180\Delta x$ by $60\Delta y$ where $\Delta y = (\sqrt{3}/2)\Delta x$. Fig. 3.1 displays sample still frames from running our MIPS model. Each of

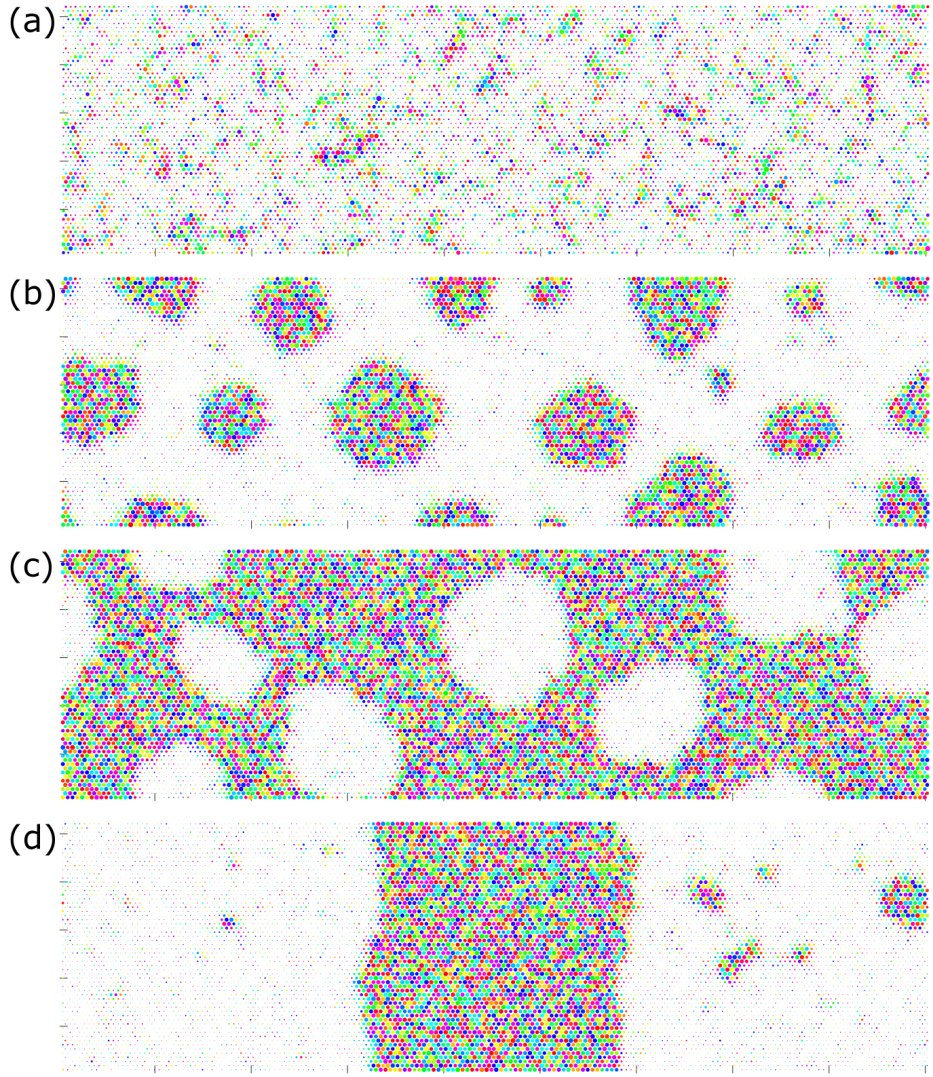

Figure 3.1: Sample behaviour of our MIPS model for various parameter values. The plots show a dot for each of our 180×60 triangular lattice sites. The colour of the dot denotes the direction of $\mathbf{u}$ according to the colour wheel in Fig. 3.2, whilst the size of the dot describes the density ρ according to Eq. (3.1). White space implies a region of low density. (a),(b),(d) are produced with $\bar{\rho} = 0.1$, however (a) has a larger noise strength, $\sigma = 0.031$, than (b)-(d) where $\sigma = 0.014$.(c) has a higher mean density, $\bar{\rho} = 0.18$, and the liquid/gas ratio is large enough such that the gas forms bubbles in the liquid. (d) has the same parameters as (b) but is taken from a significantly later time step, and has nearly reached the theoretical steady state of a single dense phase running along the shortest axis of the rectangular domain.

Figure 3.2: Colour wheel used to determine direction of velocity $\mathbf{u}$ in Fig. 3.1, 3.6 and 3.9(b).

these images portrays a snapshot of the lattice in its entirety for a single time step. The values of the macroscopic variables at each node are represented by a coloured dot; the size of the dot is the scaled local density, whilst the colour denotes the direction of the local velocity according to the colour wheel in Fig. 3.2. As our system is two dimensional a single angle (colour) is sufficient to determine the direction. The area of each dot is assigned by the following formula

$$a = a_0 \left(\frac{\rho - \rho_{\min}}{\rho_{\max} - \rho_{\min}} \right)^{3/2} + \epsilon \ , \tag{3.1}$$

where $\rho_{\max}$, ($\rho_{\min}$) is the maximum (minimum) value of ρ over all of the lattice sites in that frame, and a_0 is an appropriately chosen value for the size of the biggest circle, which depends on the spacing of the particular plot. A small value ϵ is added to ensure no values are exactly zero. Areas of low density manifest as white space with small dots, whilst high density points are large and colourful. The magnitudes of the velocities are approximately as dictated by $|\mathbf{u}^*|$, hence we only concern ourselves with the direction.

Across each of the plots in Fig. 3.1 there is almost no correlation between the colours of the dots and their nearest neighbours. This demonstrates that the systems are all highly disordered, and there is no collective motion, even at relatively small scales.

Fig. 3.1(a) shows a noisy system. Although some clusters of high density can be seen, these are fairly spontaneous events and none last long enough to grow and survive. Fig. 3.1(b) shows a system with identical parameters

as (a), with the exception that the noise strength has been reduced. The difference is visually striking, with large high density globules forming; clear phase separation.

The value of the density in the liquid and gas phases are dictated by the parameters of the system. As a result the total density simply dictates the liquid/gas fraction in the domain. If the total density is increased, such that the liquid/gas ratio is greater than 1, the image is inverted, with areas of low density dispersed among a single fully connected region of high density, as is the case in Fig. 3.1(c).

Despite the visual difference between (b) and (c), the inevitable steady state of the system is the same: namely, a single vertical strip of high density liquid, albeit the strip would be significantly thicker in the case of (c). This arrangement minimizes the effective surface tension of the system [37]. By choosing an elongated domain we have biased the system to separate in this particular fashion, with the strip running across the shortest length of the periodic rectangle. This steady state has almost been achieved in (d). As there is no collective motion, the clusters have effectively zero velocity. This means it takes a long time to reach the steady state, as clusters must either merge, or evaporate, until they have formed a single strip. For this system size, it can take in the realm of $O(10^7)$ time steps to do so. In contrast, the CIL model can achieve a steady state in approximately $O(10^3)$ time steps, as we will discuss later.

3.1.3 Phase diagram

Here we demonstrate the capabilities of our model by producing a phase diagram. To do so, we fix $\bar{\rho} = 0.12$ and vary only the strength of the noise, σ. Due to the length of time it takes to reach steady state, we reduce the system size to 90×30 lattice sites. By inspection the system appears to behave qualitatively similar to that of the larger lattice, hence we conclude that there are no strong finite size effects. The system is large enough for our purposes and does not take as long to reach equilibrium. Despite this, we still opt to take all of our samples from a single long run, in order to

minimize the chance that the system has not equilibrated when taking our measurements.

The simulation was initialized with $\sigma = 1/70 \approx 0.014$, in a state close to theoretical equilibrium. It was allowed to evolve for a further 10^6 time steps before measurements were taken. A sample was then taken every 10^4 time steps, for 100 samples. After taking the final sample, the noise strength was increased by $\delta\sigma = 1/700$. The system was allowed to relax for another 10^6 time steps before the measurements resumed at the same rate as before. After a further 100 samples the noise strength was increased again by $\delta\sigma$ and this process was repeated until $\sigma = 3/70$.

To determine whether or not phase separation had occurred, we quantified the large scale density variation by a parameter $\widetilde{\Delta\rho}$. As mentioned previously, due to the aspect ratio of the geometry and the periodic boundary conditions, the steady state is a single strip of high density parallel to the y-axis. At this stage, the system is largely invariant in the y-direction. Averaging over the density in that direction,

$$\rho_y(x) = \frac{1}{L_y}\int_0^{L_y} \mathrm{d}y\rho(x,y) \ , \tag{3.2}$$

thereby reduces the effects of the small scale stochastic fluctuations. We then took $\widetilde{\Delta\rho}$ to be simply the standard deviation of ρ_y, hence large values of $\widetilde{\Delta\rho}$ indicate phase separation.

Plotted in Fig. 3.3 are the mean values of $\widetilde{\Delta\rho}$ for the 100 samples for each value of σ. The error bars are the estimated standard deviation of the samples (not the sample mean), indicating the spread of the sample distribution. Large values of $\widetilde{\Delta\rho}$ indicate phase separation, but given that the system is noisy, $\widetilde{\Delta\rho}$ is never exactly zero, hence we must impose a cutoff. The value of $\widetilde{\Delta\rho}$ falls with increasing noise, as one would expect from the results in Fig. 3.1. Furthermore it falls faster and faster, until it quickly levels out around $\sigma = 0.0275$, at which point the standard deviation of the samples drops as well. From inspection of the samples, this is the point at which the phase separation ceases to be obvious. Hence we use $\widetilde{\Delta\rho}_{\text{threshold}} = 0.0430$, with $\widetilde{\Delta\rho} > \widetilde{\Delta\rho}_{\text{threshold}}$ taken to be phase separated.

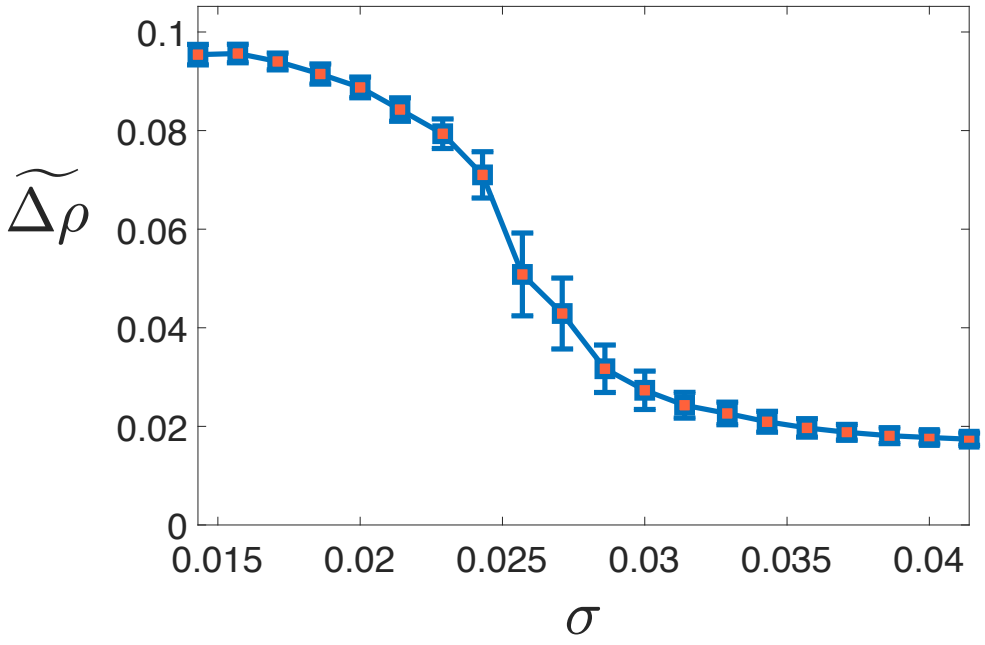

Figure 3.3: Relationship between the noise strength σ and the large scale density variation $\widetilde{\Delta\rho}$, that is, the standard deviation of the density in the x-direction. Measurements are taken from a 90×30 lattice, with parameters given by Table 3.1. Each data point is the average of 100 samples taken at intervals of 10^4 time steps from a single run. Upon taking 100 samples for a fixed σ, σ was increased and the system allowed to relax for 10^6 time steps before further measurements were taken. The error bars are the estimated standard deviation of the 100 samples. It was deemed by inspection that the cutoff threshold for phase separation corresponds to $\widetilde{\Delta\rho}_{\text{threshold}} = 0.0430$, with $\widetilde{\Delta\rho} > \widetilde{\Delta\rho}_{\text{threshold}}$ taken to be phase separated.

Once it had been identified which samples counted as phase separated, that is those with $\sigma < 0.0271$, we attempted to measure the density in the liquid and gas phases. To do this we made the assumption that the system had reached the theoretical steady state, so that the dense phase is entirely contained in a single vertical strip. To obtain the typical density value, both in and out of the strip, we averaged the density profile over a rectangle spanning the entire y-axis, but only $20\Delta x$ wide. This rectangle was shifted along the entire domain, with the highest and lowest values obtained taken as the density of the liquid and gas phases respectively.

Fig. 3.4 displays the results of this procedure, where the orange squares are the mean gas densities, and the blue circles are the mean liquid densities. Error bars for the standard error of the mean are smaller than the marker size. The data points appear to trace out a convex hull, the uppermost limits of which we have estimated with the black dashed line. Any system whose mean density and noise strength, $(\bar{\rho}, \sigma)$, falls within the yellow region will experience phase separation, with the density of their liquid and gas phases given by the values on the blue and orange curves for that σ, respectively.

Evidently there is a limit $\sigma_{\text{threshold}}$ for the noise, above which phase separation does not occur. The point at which the liquid and gas curves meet is necessarily critical. The form of the phase diagram is qualitatively similar to those from other studies on the subject, including lattice gas simulations [116], molecular dynamics simulations [35], and analytical arguments [16]. We do not go into any further detail about the nature of MIPS here, however we have demonstrated that our method has the capability to investigate this system, and may prove to be a useful tool for providing further insight into this phenomenon.

3.2 Contact inhibition of locomotion model

3.2.1 System setup

This section will focus on the results of the CIL method as described in Section 2.4.2.

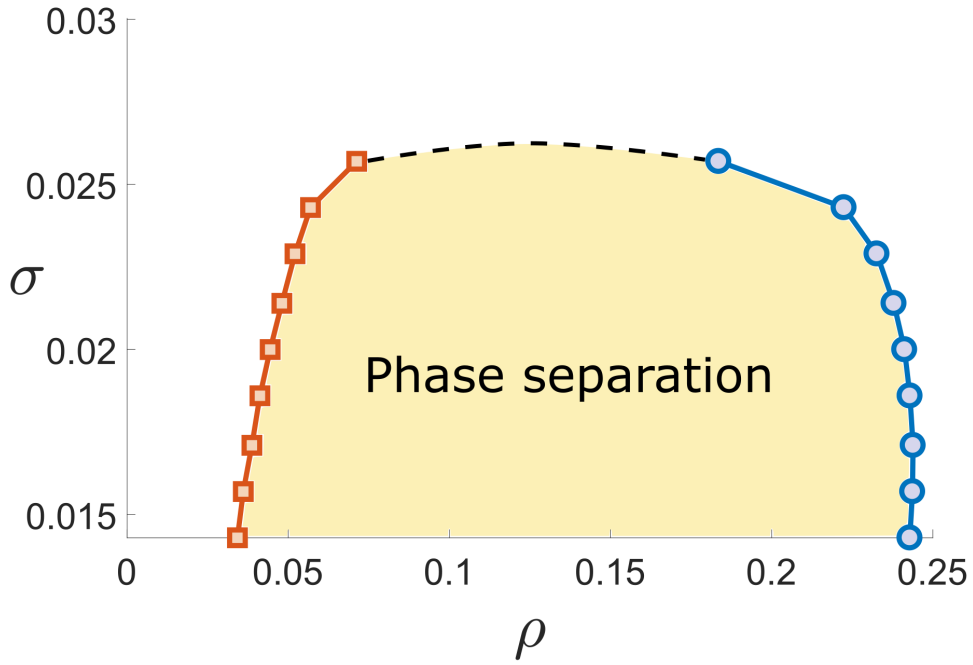

Figure 3.4: A phase diagram for the MIPS model. Presented are the mean densities of the liquid phase (blue circles) and gas phase (orange squares) for the samples with noise strength $\sigma < 0.0271$. Samples from outside this range were deemed not to have exhibited phase separation. Densities were obtained by assuming that the system is at equilibrium and hence is separated in a single vertical strip as in Fig. 3.1(d). The density profile was averaged over the y-direction, then averaged over a region $20\Delta x$ wide, with this region shifted until the maximum and minimum average densities in the system were obtained; these were deemed to be the liquid and gas densities respectively. Error bars for the standard error of the mean are smaller than the marker size. The meeting of the two curves has been estimated by the black dashed line. Results were sampled as described in Fig. 3.3, where the criterion for MIPS is also explained.

Ultimately we seek the conditions for steady large scale collective motion to exist in the system. We use the average speed of the entire system as an order parameter φ, given by

$$\varphi = \left| \frac{\sum_{\mathbf{r}\in\text{lattice}} \rho(\mathbf{r})\mathbf{u}(\mathbf{r})}{\sum_{\mathbf{r}\in\text{lattice}} \rho(\mathbf{r})} \right| . \tag{3.3}$$

Necessarily $0 \leq \varphi \leq B$. Even in complete disorder φ will never be exactly zero in a finite system, as the random vectors would have to balance out exactly. Furthermore, as φ is strictly positive, it can not have an average value of zero either. In fact for a disordered system $\langle\varphi\rangle \sim N^{-1/2}$ where N is the number of nodes in the system. Hence a cutoff value must be introduced to distinguish between disordered and ordered systems. The magnitude of $\mathbf{u}$ is also relevant in our definition of order φ, not just the direction. By this measure, a system with large values of $|\mathbf{u}|$ at each lattice site, but randomised directions, is equally disordered as a system with all of the vectors $\mathbf{u}$ aligned, but $|\mathbf{u}|$ very small throughout.

The system setup was similar to that in the MIPS model. For all of the results from the CIL model, we used a lattice of 180×60 nodes, again with periodic boundary conditions. A larger system of 360×120 nodes displayed no obvious qualitative differences, hence we concluded that 180×60 was large enough to account for any major finite size effects.

Every simulation was initialized by choosing two uniformly distributed random numbers for each lattice site – the first deciding the initial direction for $\mathbf{u}$ with each direction in $[0, 2\pi]$ equally likely, and the other choosing the initial density such that it falls within $\pm 10\%$ of $\bar{\rho}$, the prescribed average density. The initial magnitude of $\mathbf{u}$ is given by U_0, and the initial distribution f_i given by f_i^{SS}. The system was then evolved 10000 steps before any measurements were taken since our study focused on the steady state behaviour. Typically this could be achieved in roughly 1000 time steps, hence 10000 steps should guarantee that we are in a steady state for the vast majority of cases. This is significantly faster than the MIPS model, the reason being that flows develop which transport matter around the system quickly, as opposed to the MIPS model in which the clusters were essentially stationary.

As detailed below, during the course of a simulation the mean density would be deliberately changed by a small amount $\delta\bar{\rho}$ at certain time steps. This was achieved by adding $\delta\bar{\rho}/7$ to every f_i across the lattice; the system was not reinitialized. We refer to a single extended simulation with varying density as a 'run'. For measurements that involved averaging over multiple runs the initialization process was repeated between each run.

3.2.2 Typical behaviour

In our study we were interested in the steady state behaviour of the system, including the conditions for a particular state to occur and the nature of the transition between two states. Fig. 3.5 shows how φ behaves with varying average density $\bar{\rho}$ holding all other parameters constant.

Two curves have been traced by slowly increasing (blue) and decreasing (red) the total density in the system. The results displayed are averaged over 50 independent runs for each direction. A single run involved initializing the system once, and taking a sample every t_{sample} time steps, altering the average density by $\delta\bar{\rho}$ immediately after each sample is taken. Therefore, a single run provides one value of φ for each value of $\bar{\rho}$ sampled.

For each increasing density run, the system was initialized with $\bar{\rho} = 0.09$ and increased by $|\delta\bar{\rho}| = 0.0025$ every t_{sample} steps. For higher densities the system would reach equilibrium faster, hence in order to be able to detect the hysteresis effect between HO-RB and RB-HD, a lower value of $t_{\text{sample}} = 500$ was used for $\bar{\rho} > 0.2$, with $t_{\text{sample}} = 1500$ otherwise. In a finite system, using a large enough t_{sample} would eliminate all hysteresis effects, hence we must choose a value that allows the system enough time to stabilize without destroying the hysteresis entirely.

Similarly for the decreasing density runs, we initialized the system with $\bar{\rho} = 0.35$ and again decrease it by $|\delta\bar{\rho}| = 0.0025$ every t_{sample} steps, with $t_{\text{sample}} = 500$ for $\bar{\rho} > 0.2$ with $t_{\text{sample}} = 1500$ otherwise. The system was reinitialized between increasing and decreasing runs. As a result, they should be treated as independent.

The values of φ for samples at equal densities, $\bar{\rho}$, taken in the same

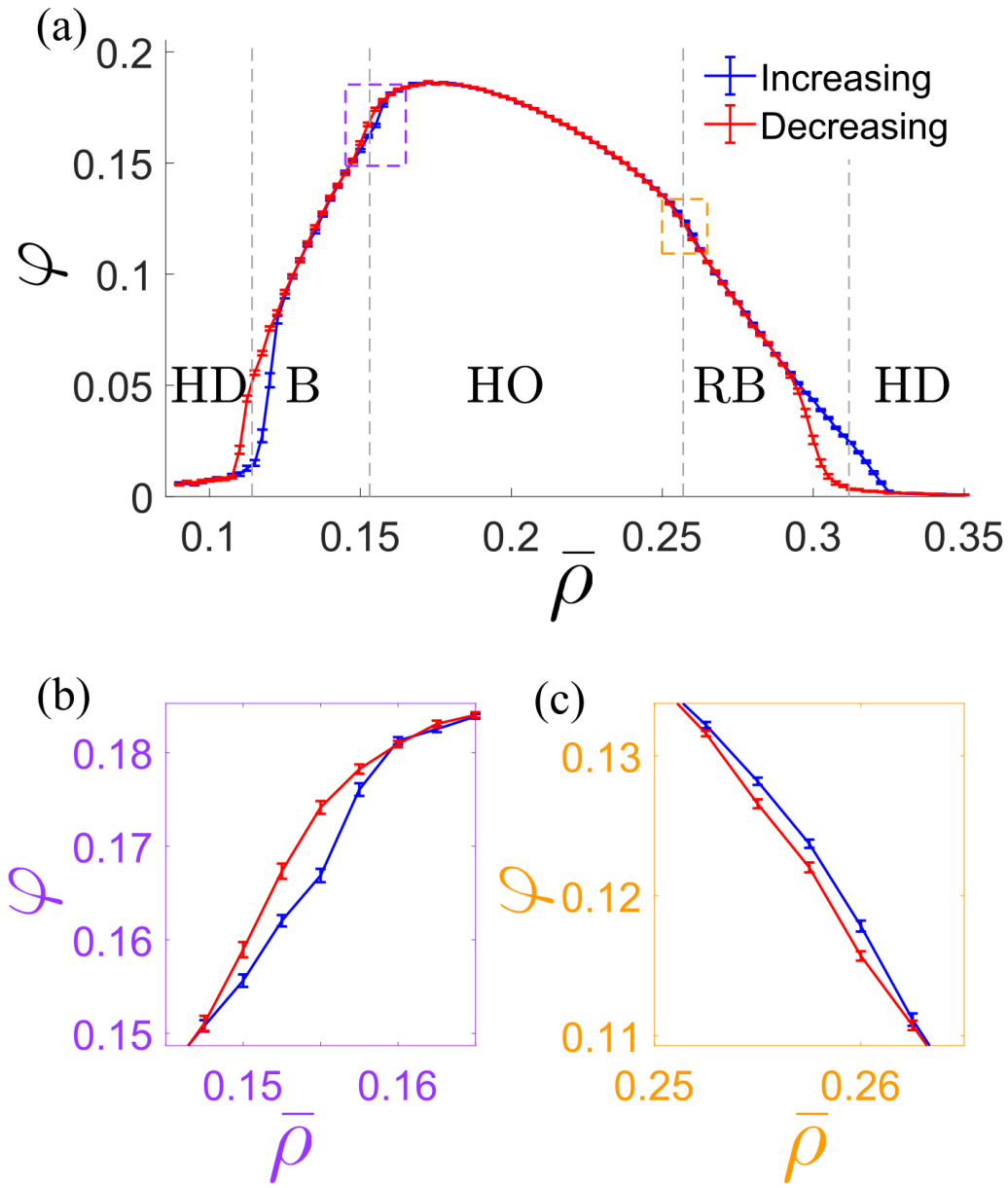

Figure 3.5: (a) Order parameter φ (Eq. (3.3)) vs. the average density $\bar{\rho}$ for $A = 2, B = 0.3$ (Eq. (2.39)). Measurements were taken whilst slowly increasing (blue) or decreasing (red) the total density in the system. The results align with the exception of four hysteresis loops, which locate the corresponding first-order phase transitions. The phase transitions partition the system into four distinct regimes: HD – homogeneous and disordered, B – banding, HO – homogeneous and ordered, RB – reverse banding. (b),(c) Magnified versions of the purple and orange dashed boxes respectively, highlighting the hysteresis effect in each.

direction of the cycle were collated and averaged. These average values trace the respective curves in Fig. 3.5. The error bars are the estimate of the standard error of the mean, that is, the estimate of the standard deviation σ_φ of the samples at each value of $\bar{\rho}$ scaled by the square root of the sample size, $\sigma_\varphi/\sqrt{50}$.

The remaining parameters were fixed at the values given by Table 3.2.

Parameter	Value
τ	1
B	0.3
A	2
c	1
σ	1/70

Table 3.2: Parameters used to obtain the results depicted in Fig. 3.5, Fig. 3.6, Fig. 3.8 and Fig. 3.9, with the exception of A which was varied in the latter two figures. Values are non-dimensional.

The two curves coincide well, with the exception of four regions, in which there exist hysteresis loops. These loops indicate the existence of meta-stable states; we therefore use them as proxies for the locations of first-order phase transitions that separate distinct regimes. The central two hysteresis loops are harder to spot; (b) and (c) are magnified versions of the purple and orange boxes respectively. Although they depict a smaller hysteresis than the more obvious pair, the actual difference between the values in the two branches is irrelevant. All that matters is that it is non-zero and clearly larger than the error bars. From this we can deduce that there is a discontinuity in the order parameter, which is indicative of a first order transition.

As evidenced by the value of φ collective motion exists only for the central values of $\bar{\rho}$, in the three regions labelled B, HO and RB. Recall that φ cannot be exactly zero, hence the regions marked as HD are considered to have no collective motion. We now examine the characteristics of the steady state in these regions. There are four distinct regimes, which are represented in Fig. 3.6 using the same visualisation scheme as in Fig. 3.1.

The first of these states is one of global disorder. Small clusters of sim-

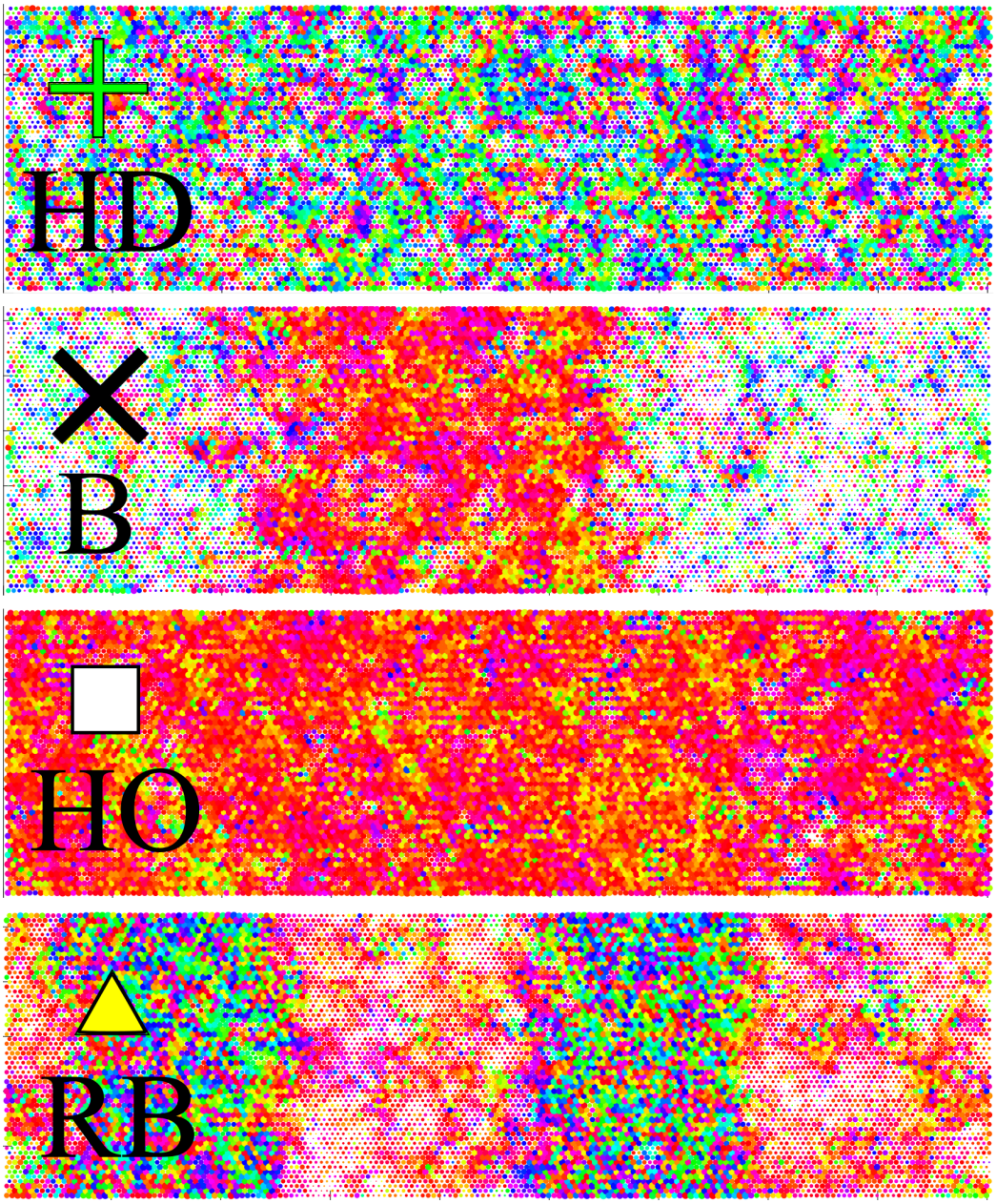

Figure 3.6: Snapshots of the typical steady state behavior of each of the phases. Display scheme is same as that in Fig. 3.1. Regions of uniform colour indicate collective motion in that region. The coloured symbols are identifiers for the data points in Fig. 3.9(a). Parameter values used are given in Table 3.2, with $\bar{\rho} = 0.105,\ 0.1425,\ 0.185,\ 0.2875$ for HD, B, HO, RB respectively.

ilar colours demonstrate that there is mild local alignment, but this cannot extend more than two or three lattice sites, and there is no collective motion across the system. Density fluctuations are also localised, hence we refer to this as the homogeneous disordered (**HD**) regime. In comparison, the third example is also homogeneous in density, but everywhere is predominantly red. Therefore there is a strong correlation in the velocity field across the system and we have collective motion. We refer to this state as homogeneous ordered (**HO**).

Returning to Fig. 3.5(a) we can see that two of the regions, those of the highest and lowest mean densities $\bar{\rho}$ presented, are in the HD phase and their behaviour is equivalent. They provide the lowest values of φ whilst the HO regime has the highest. These regions are separated by what we refer to here as the banding (**B**) and reverse banding (**RB**) regimes, each of which are revealed to be a co-existence of a HD phase and a HO phase, as visualised in Fig. 3.6. Their existence can be understood if we consider the transitions involved. Starting from the low density HD region, noise dominates and there is no global alignment. Upon increasing the density we enter the banding regime, where alignment effects take over and dense locally aligned bands spontaneously develop, which propagate through a low density disordered region. We recognise these bands as a HO phase moving through a dilute HD phase. Evidently and intuitively, the density must be a minimum value in order to overcome the noise and induce stable collective alignment. For the mean density values comprising the banding regime, this threshold would not be achieved if the matter was spread evenly across the system. However there is enough matter such that when concentrated in a band, the threshold can be achieved, and hence stable collective motion can exist within the confines of the band. As the mean density is increased further, the density in each phase remains constant. Instead, the high density bands grow in thickness until eventually the dilute HD phase vanishes in a similar fashion as to how the bands appeared, resulting in a single HO phase.

The first transition, HD-B, marking the onset of collective motion, is easily recognised from previous flocking studies [42, 62, 63, 66] which found it to be first order. The second transition, B-HO, where the dilute disordered

phase vanishes to leave homogeneous collective motion, is also present in these models but is less well studied. This is probably because higher density molecular dynamics simulations are more difficult to compute, although it has recently been shown to also be a first order transition [66]. Our results are in perfect agreement with both of these as evidenced by the aforementioned hysteresis loops. This lends credence to the conclusion that the two remaining hysteresis loops at higher densities also indicate first-order phase transitions, which to our knowledge have not been reported previously. These transitions do not exist in minimal flocking models with no volume exclusion effects, such as the Vicsek model, and, as we will see, are a result of our contact inhibition of locomotion assumption. The transitions separate the HO region from another HD region, again through a coexistence regime similar to the B regime (Fig. 3.6), but with the properties inverted — the high density regions are disordered (HD), whilst the low density regions are aligned and moving (HO). In the steady state, as material in the HO phase flows into a dense band it comes to a halt, extending the band on that side, whilst on the other side the band decays as the material flows away. The net result is that the dense band, although locally stationary, appears to propagate against the direction of flow, hence we call it reverse banding (RB). In other words, the dense band moves due to condensation on one side and evaporation on the other.

In active matter, this phenomenon was first reported in a collective cell migration model [124], and likened to density waves observed in traffic flow [123]. Interestingly, the same mechanism also underlies the directed motion of condensed drops under the influence of a chemical gradient [126], as well as the formation of a drop lattice in a chemical reaction-controlled phase separated drop system [127]. The RB regime also bears striking resemblance to the glider phase observed in a lattice gas experiment on flocking models [117]. However, they find the dense phase to be ordered, whilst their dilute phase is disordered; the reverse of our findings. Alternatively, as our system does not distinguish between velocity and orientation, applying our measure of order to their system would consider their dense phase disordered (or very weakly ordered) as the particles are jammed and cannot move, but their sparse phase

would also be disordered, as there is no obvious alignment between the particles. Therefore since both phases are disordered, their model would have more in common with our MIPS model, albeit they have a steady drift to the dense phase.

The reverse banding exists for a different reason than the banding phase, but the logic is similar. In the HD-B transition, the noise was overcome by increasing the density. This is because, in terms of changing the direction of motion, the noise has a stronger effect on nodes with low densities. The same is true for nodes with low speeds, because our noise is defined such that it acts on the momentum $\rho\mathbf{u}$ with constant strength. We discuss this in more detail in Section 3.2.5, but for now we demonstrate the effect visually in Fig. 3.7. Displayed on the left hand side are vectors representing the corresponding values of f_i (blue arrows), and the resultant velocity vector (yellow arrow), for three different distributions at a single node. The second distribution has the same velocity as the first but a lower density, whilst the third has the same density but a lower speed. Added to each of these is a noise distribution, identical in each of them, resulting in the corresponding distributions on the right hand side. Of particular interest is the deflection of the velocity from the original direction. For the first distribution the deflection is minimal; less than 30°. The same cannot be said for the second and third distributions, in which the velocities have almost reversed direction entirely.

So in addition to density, there is a minimum requirement on the speed for collective motion to occur. Recall that the speed is given by $U_0 = B - A\rho^2$. The parameter B was chosen such that this is achieved for our choice of σ. However, since $A > 0$, as ρ increases, U_0 decreases, until we fall below the minimum again, thus we have the higher density HD region. As with the B regime, if the density is non-uniformly distributed, then the density in certain regions can be *low enough* such that collective motion exists. This is exactly what is happening in the RB regime. The density is pooled in bands which are stationary, permitting collective motion to occur in a dilute phase.

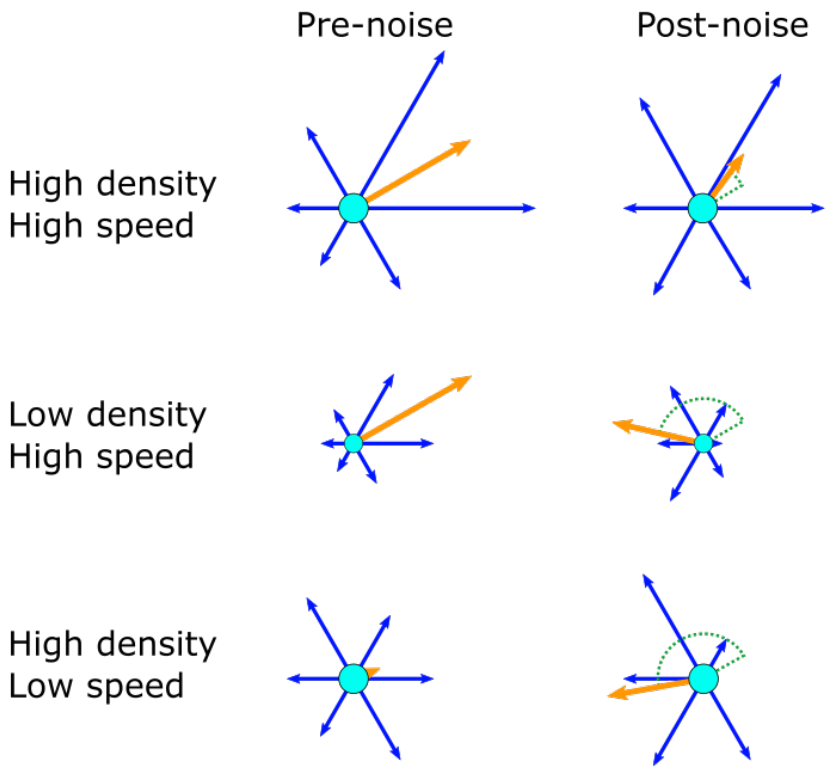

Figure 3.7: Schematics demonstrating the effect of identical noise functions on different distributions f_i. The length of the blue arrows indicate the value of f_i in the respective direction, with f_0 represented by the cyan circles. With both high density and high speed, the velocity vector (orange) is deflected by a small amount, whilst distributions that lack either of these are vulnerable to large changes in direction.

3.2.3 Phase behaviour

The results so far have been for a single fixed $A = 2$. We claimed that the higher phase transitions in Fig. 3.5 and the related RB and HD regimes only exist because the velocity decreases with ever increasing density, which we view as contact inhibition of locomotion. To verify this we now vary the parameter A, as well as $\bar{\rho}$, as A controls the rate of CIL in our expression for U_0. From this we create a phase diagram. In order to do so we need to be able to systematically classify the sampled data points as one of the aforementioned regimes, HD, B, HO or RB.

The parameters are the same as in Table 3.2, except of course A is now varied. Results were obtained by fixing A then slowly varying $\bar{\rho}$, much as for Fig. 3.5 except: there were no descending runs, $\Delta\rho = 0.01$, and $t_{\text{sample}} = 10000$, which is enough for the system to reach its steady state. The starting value for the density was $\bar{\rho} = 0.05$, and the highest value was $\bar{\rho} = 0.35$. Each run was repeated 10 times therefore there were 10 independent samples for each point $(\bar{\rho}, A)$. At each point, the parameters φ, $\widetilde{\Delta\rho}$, ζ (see below) were calculated for each of the 10 samples, then averaged and compared with our cutoff values. We determined the cutoff values by examining borderline cases by eye.

In order to categorize the system's behaviour, we used the following systematic method. Firstly, anything above the red line $B - A\bar{\rho}^2 = 0$ was marked as motionless, as this would have $U_0 = 0$ throughout the domain. As established, we have a finite system, and so even in the most disordered phase φ is never exactly zero, and as it is strictly positive it cannot average to zero either. Therefore we must impose a cutoff value to distinguish between a completely disordered state and one with an ordered phase (including the B and RB regimes). We used the cutoff $\varphi_{\text{threshold}} = 0.024$, with $\varphi < \varphi_{\text{threshold}}$ marked as HD.

To determine whether or not phase separation had occurred we used the same parameter $\widetilde{\Delta\rho}$ as defined for the MIPS model. As before, we had to impose a cutoff to distinguish between phase separated regions and local noise. This time we chose this to be $\widetilde{\Delta\rho}_{\text{threshold}} = 0.012$, with $\widetilde{\Delta\rho} > \widetilde{\Delta\rho}_{\text{threshold}}$

considered to be either within the B or RB regimes. Fig. 3.8 shows a 3D representation of $\widetilde{\Delta\rho}$ over the parameter space. The two high ridges clearly correspond to the B and RB regions. These narrow in thickness and the peak decreases as they approach each other and seem to vanish at the point where they meet.

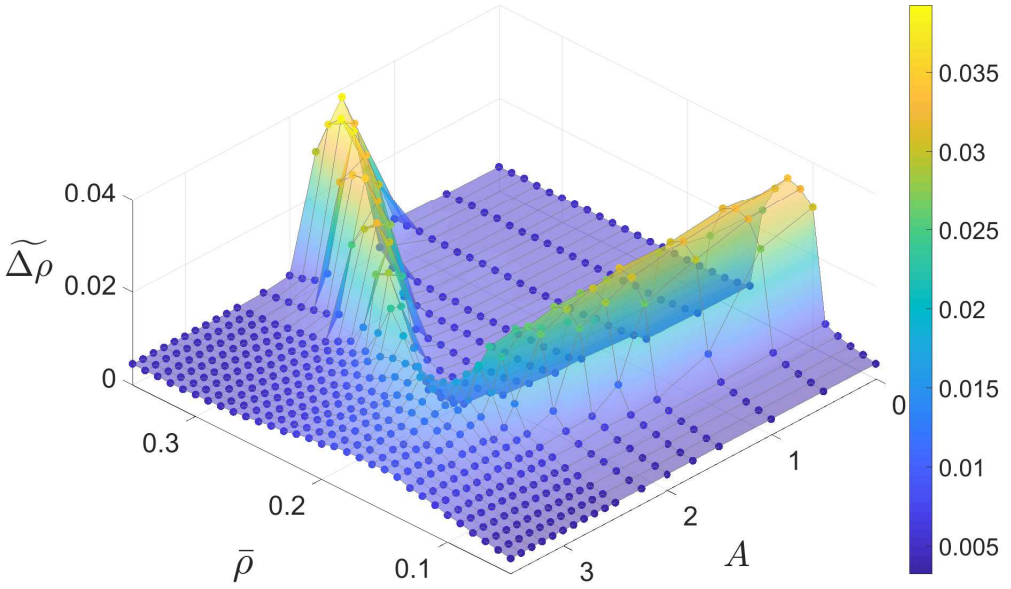

Figure 3.8: Surface plot showing the steady state behaviour of $\widetilde{\Delta\rho}$ over the parameter space, with high values of $\widetilde{\Delta\rho}$ indicating phase separation. The two high ridges visible correspond to the the banding B, and reverse banding RB regimes.

The two aforementioned quantities, φ and $\widetilde{\Delta\rho}$, do not enable us to distinguish between the B and RB phases. Therefore we also measured the following parameter:

$$\zeta = \frac{\sum_{\mathbf{r}\in\text{lattice}} \rho(\mathbf{r})[B - |\mathbf{u}(\mathbf{r})|]}{\sum_{\mathbf{r}\in\text{lattice}} \rho(\mathbf{r})} \,, \tag{3.4}$$

where ζ is large if high density regions are stationary, as in the RB regime.

Hence we identified RB values with $\zeta > \zeta_{\text{threshold}} = 0.1$.

These rules are summarized in Table 3.3. Visual inspection of the samples at several distinct points in the phase diagram shows the categorization to be largely accurate.

Regime	φ	$\widetilde{\Delta\rho}$	ζ
HD	< 0.024	–	–
HO	≥ 0.024	≤ 0.012	–
B	≥ 0.024	> 0.012	≤ 0.1
RB	≥ 0.024	> 0.012	> 0.1

Table 3.3: Rules used to classify points in Fig. 3.9.

The results are compiled in the phase diagram in Fig. 3.9(a). The marker symbols correspond to those in Fig. 3.6, as classified by our rules. Also included is a region of red asterisks; these are the points for which $B < A\bar{\rho}^2$, hence U_0 is zero throughout the system. The red line marks the dividing line $B = A\bar{\rho}^2$. The background colour of the phase diagram is the interpolated φ. The black curves are hand-drawn and mark the approximate locations of the first order phase transitions between the various regimes. They have been deemed first order partly through extrapolation from the results for $A = 2$, but also because of the sharp change in φ across the these lines, suggesting that there is almost certainly a discontinuity, hence a first order transition. Most curiously, these lines meet at the point marked by the star, which we discuss further shortly.

Note that when $A = 0$, we recover the expected phenomenology of a typical polar active model, such as the Vicsek model [50], in that the system transitions from the HD phase to the B regime followed by the HO phase as density increases, with no further change. However, as A grows, we see that the HO phase will transition back to the HD phase via the RB regime as density increases further. This agrees with our claim that these latter phases exist due to contact inhibition of locomotion. As A increases further the values of $\bar{\rho}$ for which the RB regime exist also decrease. Interestingly, the reverse is true for the B regime. For a fixed small density, initial increases

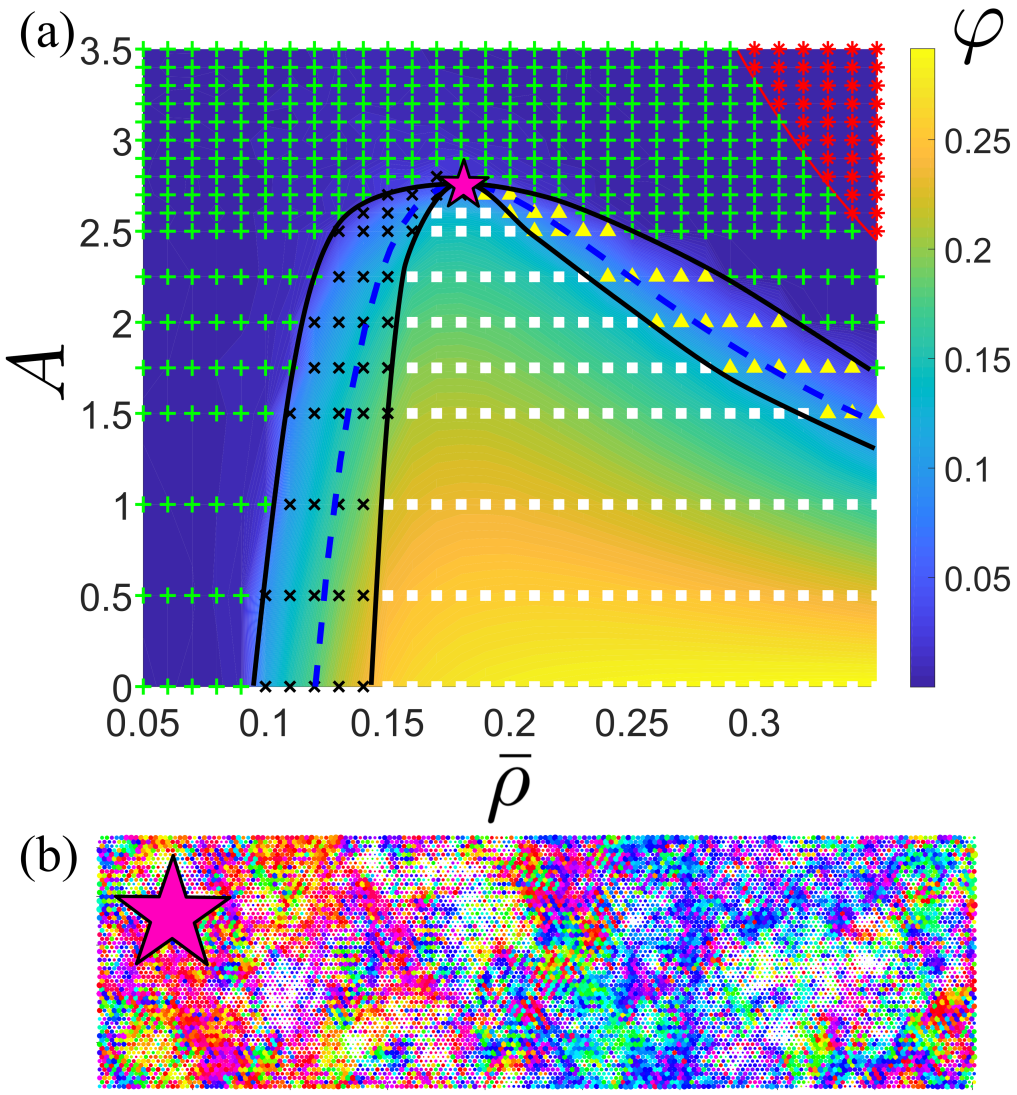

Figure 3.9: (a) Phase diagram comparing average density $\bar{\rho}$ with coefficient A. Each sample point was identified as belonging to one of five regimes, categorised by the coloured symbols (see Fig. 3.6). The red asterisk region has zero motion because $|\mathbf{u}| = B - A\bar{\rho}^2 \leq 0$ with equality depicted by the red line. Black lines depict approximate locations of phase transitions (drawn by eye) which meet at a critical point (star). The dashed blue curve also passes through this point and is a contour of ρU_0. It corresponds to the theoretical separatrix $\alpha_R = 0$, with $\alpha_R > 0$ below the curve. See Section 3.2.5 for details. (b) Snapshot of behavior close to the critical point at $\bar{\rho}_c \approx 0.18$ and $A_c \approx 2.75$, using same display scheme as in Fig. 3.6.

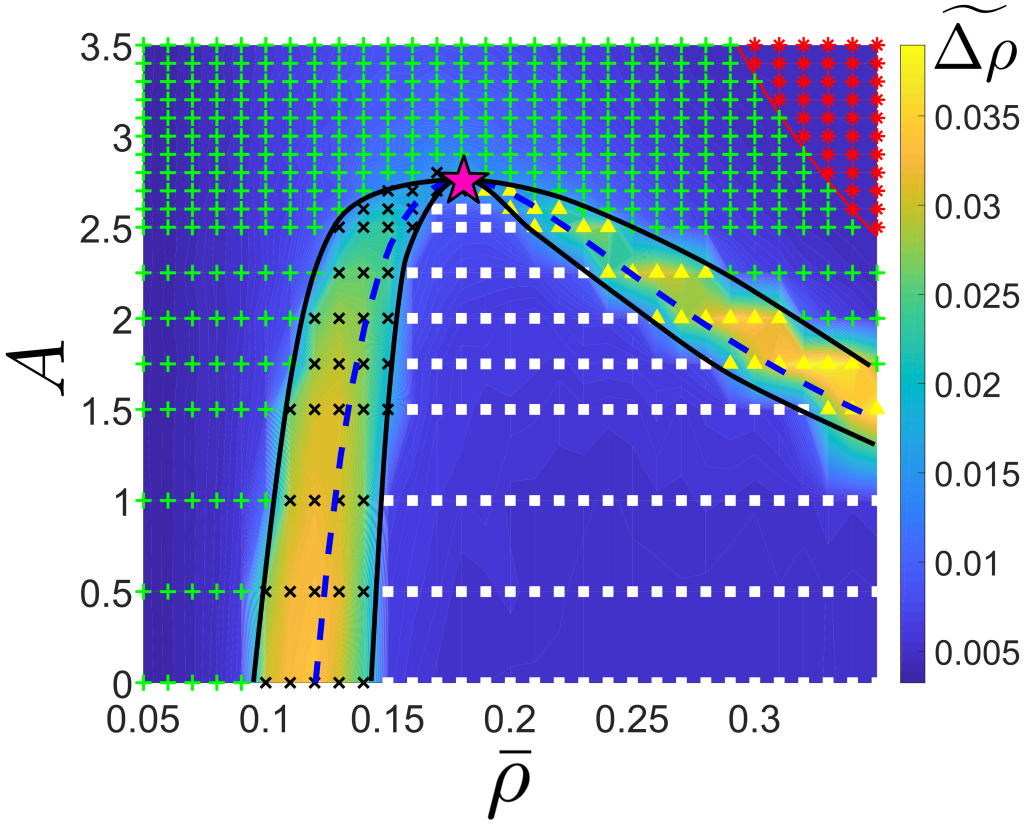

Figure 3.10: Phase diagram is identical to Fig. 3.9(a), apart from the background colour which now corresponds to the density variation parameter $\widetilde{\Delta\rho}$. Here, the R and RB regimes are clearly recognisable as the areas of high $\widetilde{\Delta\rho}$. They appear to act as buffer zones between HD and HO, except at the critical point (star), where the R and RB regimes meet and vanish.

in A have little effect and our transition lines are roughly parallel with the vertical axis. However, eventually A does begin to have an affect, and the transition responds by necessarily increasing the density. This is in line with our earlier comments; to overcome the noise, one must increase the density or increase the speed. As the speed falls, the density must increase to maintain the same outcome.

This leads to the most interesting outcome of our research. As the two leftmost transition lines bend to the right as A increases, and the rightmost lines travel to the left, all four first-order phase transition lines converge to a single point, indicated by a star in Fig. 3.9(a). If the phase boundary is now traversed by varying A at this fine-tuned density, the system will go directly from the HD phase to the HO phase, without any spatial heterogeneity as displayed in the B or the RB regimes. This is also evident from Fig. 3.8, as the critical point matches up with the point where the two ridges vanish as they meet each other. The order parameter φ also rises from (almost) zero in the HD phase to a positive value in the HO phase in a continuous manner. We therefore conclude that such a transition is critical and the star thus indicates a critical point of this active fluid model.

A snapshot of this critical behavior is shown in Fig. 3.9(b). We will discuss this critical point further in our hydrodynamic analysis. There is no obvious banding, though density variations appear larger than in the HD or HO regimes. More visually striking is that the regions of aligned motion are much further reaching, at places spanning the entire width of the domain, though no single direction dominates the entire system.

3.2.4 Analytical interpretation

As established in Chapter 2, in the hydrodynamic limit our model is necessarily described by the Toner-Tu equations due to our imposed symmetries. We now connect our simulation findings to the Toner-Tu model by performing a linear stability analysis.

We will use the version of the Toner-Tu EOM derived through our Chap-

man Enskog analysis in Section 2.5.2, that is:

$$\partial_t \rho + \nabla \cdot (\rho \mathbf{v}) = 0 \ , \tag{3.5}$$

$$\rho \left(\partial_t \mathbf{v} + \mathbf{v} \cdot \nabla \mathbf{v}\right) = -\nabla P + \nu \nabla \cdot \rho \left(\nabla \mathbf{v} + (\nabla \mathbf{v})^T\right) + \mathbf{F} \ , \tag{3.6}$$

where $P = c_s^2 \rho$ and we take $\mathbf{F} = \rho \left[\alpha(\rho) - \beta |\mathbf{v}|^2\right] \mathbf{v}$.

Since the bands in both the B and RB regimes are perpendicular to the direction of collective motion in the dense and dilute regions, respectively, the most unstable wave vectors in the HO state are expected to be parallel to the direction of motion. Therefore, we need only consider a 1D system, where the coordinate x is the direction of the collective motion. Expanding about a homogeneous collective motion state with $\rho = \rho_0 + \delta\rho \exp[st - \mathrm{i}kx]$, $v = \sqrt{\alpha_0/\beta} + \delta v \exp[st - \mathrm{i}kx]$ and $\alpha = \alpha_0 + \alpha_1 \delta\rho$, we have to linear order:

$$\left(s - \mathrm{i}k\sqrt{\frac{\alpha_0}{\beta}}\right) \delta\rho = \mathrm{i}k\rho_0 \delta u \ , \tag{3.7}$$

$$\rho_0 \left(s - \mathrm{i}k\sqrt{\frac{\alpha_0}{\beta}} + 2\alpha_0 + 2\nu k^2\right) \delta u = \left(\mathrm{i}k c_s^2 + \rho_0 \alpha_1 \sqrt{\frac{\alpha_0}{\beta}}\right) \delta\rho \ .$$

Note that for a stable system $\beta > 0$ necessarily, thus $\alpha_0 > 0$ implies collective motion, with $\alpha_0 \leq 0$ giving a stationary state.

Solving for s and focusing on the real part, which determines the stability of the system, we have

$$\mathrm{Re}[s] = \begin{cases} -2\alpha_0 + \mathcal{O}(k^2) \\ \frac{k^2}{8\alpha_0^2 \beta} \left[\alpha_1^2 \rho_0^2 - 4\alpha_0 c_s^2 \beta\right] + \mathcal{O}(k^3) \end{cases} \ , \tag{3.8}$$

where $\mathrm{Re}[s] > 0$ implies instability. The first eigenvalue $-2\alpha_0$ corresponds to the fast relaxation that occurs when the velocity deviates from the mean field value $\sqrt{\alpha_0/\beta}$ in the absence of spatial variations. The second eignvalue quantifies when the instability sets in. In particular, if $\alpha_0 \to 0$ and $\alpha_1 \neq 0$, the system is always unstable. In previous studies of collective motion, α_1 is typically assumed to be positive, so that alignment increase with density, and as α goes from negative to positive the system will necessarily become unsta-

ble resulting in the banding instability [42, 50, 62, 66]. This also corresponds to the banding (B) regime in our system, since a higher density reduces the effects of the noise, and as such alignment increases with density.

However, it is also clear from Eq. (3.8) that the instability condition does not depend on the sign of α_1. Hence, if α decreases as density increases, for example due to contact inhibition, the system will again be unstable. This is exactly what occurs in our simulation and corresponds to the Reverse-Banding (RB) regime in our phase diagram.

In our simulation we found that all four first-order phase transition lines converge at a critical point. With our hydrodynamic argument, we can see that this critical point is reached by setting both α_0 and α_1 to zero, which is achieved by fine-tuning $\bar{\rho}$ and A in our simulation. We believe that this critical point uncovered is distinct from any critical behaviour discussed in the context of dry polar active matter. We are aware of critical phenomena analyzed, either analytically or computationally, in the following active matter systems: 1) self-propelled particles with long-ranged metric alignment interactions [46,128], 2) incompressible active fluids [129], 3) critical motility-induced phase separation [116, 130, 131], and 4) self-propelled particles with velocity reversals and alignment interactions [32]. Our critical system is different from system 1) because ours does not have long-range interactions, from 2) because our velocity field is not divergence free (in fact, imposing the incompressibility condition by itself amounts to a type of long-range interactions), from 3) because critical MIPS happens in the disordered phase while criticality in our system occurs at the onset of the ordered phase, from 4) because our system exhibits collective motion while system 4) exhibits only orientational order, but no collective motion. Besides the above comparison, as our model spontaneously breaks rotational invariance at the critical point, it is also distinct from critical active matter in which the direction of motion is determined by an external field [132, 133].

3.2.5 Fluctuation-induced renormalization of α

In Chapter 2, we confirmed that our system indeed simulates a version of the Toner-Tu equations. There we found our system parameters to be related via

$$\alpha = \frac{1}{\Delta t\,(2\tau - 1)} \quad , \quad \beta = \frac{\alpha}{U_0^2} \ . \tag{3.9}$$

We have just demonstrated that the critical point relates to the parameter α through its relationship with ρ in $\alpha \approx \alpha_0 + \alpha_1\rho$, but the expression we have derived for α does not depend on the density at all, yet we still observe the same critical point.

The reason for this apparent contradiction is the noise; Eq. (3.8) was derived from a deterministic system of equations, but our LBM has stochastic noise which we previously did not incorporate into our Chapman-Enskog derivation. We will do so now by renormalizing α to account for the noise. We will not perform a full renormalization procedure on the EOM, as all we seek is to relate the result of the Chapman-Enskog expansion to our linear stability analysis.

Firstly, we must understand the macroscopic effect of the noise. Recall that

$$\sum_{i=0}^{7} \eta_i = 0 \ , \tag{3.10}$$

hence there is no contribution to the continuity equation. Let's define

$$\mathbf{h} = \sum_{i=0}^{7} \eta_i c\mathbf{e}_i \ . \tag{3.11}$$

From the definition of η_i it follows that

$$\langle h_x \rangle = \langle h_y \rangle = \langle h_x h_y \rangle = 0 \ , \tag{3.12}$$

$$\langle h_x(\mathbf{x},t) h_x(\mathbf{x}',t') \rangle = \langle h_y(\mathbf{x},t) h_y(\mathbf{x}',t') \rangle = c^2\sigma^2\delta(\mathbf{x}-\mathbf{x}')\delta(t-t') \ . \tag{3.13}$$

Our previously derived Eq. (2.121) now becomes

$$\rho\left(\partial_t \mathbf{v} + \mathbf{v}\cdot\nabla\mathbf{v}\right) = -\nabla P + \nabla\cdot\rho\nu\left(\nabla\mathbf{v} + (\nabla\mathbf{v})^T\right) + \mathbf{F}_{\mathrm{CIL}} + \mathbf{h}\ . \tag{3.14}$$

This equation is in terms of the momentum $\rho\mathbf{v}$, and not $\mathbf{u}$ as in Eq. (1.1b). Therefore the stochastic noise $\mathbf{f}$ in Eq. (1.1b) is related to $\mathbf{h}$ by

$$\mathbf{f} = \frac{\mathbf{h}}{\rho}\ . \tag{3.15}$$

Thus $\langle|\mathbf{f}|^2\rangle = 2c^2\sigma^2/\rho^2$.

The renomalization calculation mirrors almost exactly the corresponding calculation in the study of incompressible active polar fluids at criticality [129], except that the projection operator is absent here since our system is not incompressible. Specifically, the shift in α is given by

$$\delta\alpha = -\beta\int\frac{\mathrm{d}^{\mathrm{D}}\mathbf{q}}{(2\pi)^{\mathrm{D}}}\frac{\mathrm{d}\Omega}{2\pi}\frac{\langle|\mathbf{f}|^2\rangle}{(\mu q^2+\alpha)^2+\Omega^2} \tag{3.16}$$

$$= -\beta\frac{c^2\sigma^2}{\rho^2}\int\frac{\mathrm{d}^{\mathrm{D}}\mathbf{q}}{(2\pi)^{\mathrm{D}}}\frac{1}{\mu q^2+\alpha} \tag{3.17}$$

$$= -\frac{c^2\sigma^2\beta}{\rho^2\left(\mu\Lambda^2+\alpha\right)}\frac{S_{\mathrm{D}}\mathrm{d}\ell}{(2\pi)^{\mathrm{D}}}\ . \tag{3.18}$$

where $S_{\mathrm{D}} \equiv 2\pi^{\mathrm{D}/2}/\Gamma(\mathrm{D}/2)$ is the surface area of a unit sphere in D dimensions, Λ^{-1} corresponds to the small length scale cutoff, and $\Lambda\mathrm{d}\ell$ corresponds to the width of the momentum shell being integrated over in the above coarse-graining process.

Adding this shift to α modifies it to, to $\mathcal{O}(\alpha)$:

$$\alpha_R = \alpha\left(1 - \frac{c^2\sigma^2}{\rho^2U_0^2\mu\Lambda^2}\frac{S_{\mathrm{D}}\mathrm{d}\ell}{(2\pi)^{\mathrm{D}}}\right) = \alpha\left(1 - C_1\frac{1}{\rho^2U_0^2}\right)\ , \tag{3.19}$$

where we have used $\beta = \alpha/U_0^2$ as in Eq. 2.126 and C_1 is some constant.

The results of our stability analysis indicate that the critical transition occurs when U_0 and ρ are fine tuned such that $\alpha_R = 0$ and $\partial\alpha_R/\partial\rho = 0$, which can be achieved in our LBM by fine tuning $\bar{\rho}$ and A in the expression

of U_0, specifically to

$$\bar{\rho} = \frac{3\sqrt{C_1}}{2B} \quad , \quad A = \frac{4B^3}{27C_1} \ . \tag{3.20}$$

In our simulations we found $\bar{\rho}_c \approx 0.18$, $A_c \approx 2.75$. These values give $B \approx 0.27, C_1 \approx 0.001$, which is fairly consistent with our actual value of $B = 0.3$. In fact we can go further. In Fig. 3.9 the blue dashed line depicts the full contour for $\alpha_R = 0$ using these values. For parameter values below this curve $\alpha > 0$ and we have collective motion, with $\alpha < 0$ for parameter values above. By design this line cuts through our critical point (star), however it also bisects the banding and reverse banding regions, in perfect agreement with both our stability analysis; in the vicinity of this curve $\alpha_0 \approx 0$ and $\alpha_1 \neq 0$ except at the critical point.

Chapter 4

Interfacial instability

The work presented in this chapter was published in the paper:
D. Nesbitt, G. Pruessner, and C. F. Lee, "Edge instability in incompressible planar active fluids," *Physical Review E*, vol. 96, no. 6, pp. 1-7, 2017.

The banding regime of the CIL model manifested as a strip of dense aligned matter which propagated through a sparse disordered region. A single strip minimises the effective surface tension between the two phases, but for such a configuration to be stable at all is far from trivial. For example, the setup has similarities with the Saffman-Taylor instability, a classic example of interfacial pattern formation in fluid dynamics. Also known as viscous fingering, it refers to the interfacial phenomenon observed when a fluid is injected into a Hele-Shaw cell, displacing a resting fluid of higher viscosity. In such a case, the leading edge of the advancing fluid does not propagate uniformly, but splits into finger-like protrusions [134]. Whilst this is well understood in the context of classical fluids, what happens when we instead use an active fluid?

The answer to this question has direct relevance to epithelial tissue. In its simplest form, as in wound healing experiments, the tissue consists of a single

layer of tightly packed cells. These cells not only interact through adhesion and contact forces, they can also generate motility forces by crawling on the substrate; the tissue certainly qualifies as active matter. When an *in vitro* cell monolayer is scratched, or barricades are removed [69, 71], simulating a wound, the tissue spreads to fill the void (Fig. 4.1). However, a common observation from experiments is that an initially straight wound does not heal uniformly [69, 71]. Instead finger-like protrusions develop at the leading edge, reminiscent of those in the Saffman-Taylor instability.

The exact reason for this pattern formation remains unclear, with some attributing the effect to particular 'leader' cells guiding the rest [69, 135, 136]. These cells can be observed at the tip of the finger and are typically much larger and more active than the other cells in the tissue [69]. It was believed that the trauma from the formation of a wound induced the formation of leader cells, however the method of removing barricades debunks this idea, as the trauma is minimal yet both leader cells and finger formation are still observed [69].

Nonetheless, particle simulations have shown that the phenomenon can emerge from the collective motion of actively crawling cells with strong cell-cell adhesion, with no need for leader cells [8]. These results suggest that the fingering pattern may be a form of emergent behaviour; that collections of cells will always behave as such with no need for specialised leader cells, much like how the Saffmann-Taylor patterns form out of two homogeneous fluids. These findings motivate treating the sheet as an active fluid, as such an emergent behaviour should be observable from the macroscopic equations of motion. Though what exactly are the equations of motion for a sheet of epithelial cells is also cause for debate.

The particles in the molecular dynamics simulation mentioned above generate motility forces in a random direction, with a bias towards the direction they are already moving, hence they are polar. The motility forces are of constant strength with respect to the fixed substrate, therefore the system is dry. Cells interact simply via short range repulsive and medium range attractive forces, meaning the cells are roughly the same distance apart from one another. In addition to this the cells grow and divide when larger than

a certain threshold [8].

Alternatively, other studies consider epithelial layers to be nematic in nature. Several works have investigated the effects of topological defects within the structure of a tissue layer, and how they induce motion [74, 76]. In particular, by representing a cell division event with a local nematic dipole, simulations were able to reproduce similar finger-like growth to that of MDCK cells [75].

In contrast, a recent analysis of a minimal hydrodynamic model suggested that the fingering instability could arise simply out of cells collectively crawling on a substrate, without cell division, which qualifies instead as a dry polar active fluid [6]. A linear stability analysis suggested that the edge of a homogeneous incompressible planar active fluid is stable when the fluid is moving at a constant rate, however the interface becomes unstable if the fluid is initially stationary. However, their results included non-physical singularities in the growth rate, which they acknowledged was caused by neglecting a time derivative, meaning that the growth rate was not well defined. Here, we perform a more thorough theoretical analysis of the same model as in [6] to resolve these singularities and arrive at a qualitatively different conclusion.

4.1 Incompressible hydrodynamic model of wound healing

The model system consists of an incompressible two-dimensional dry polar active fluid propagating in the direction of its free surface, as illustrated in Fig. 4.1. This setup is similar to that of Saffman-Taylor, however we do not apply a pressure gradient to the active fluid; any propulsion will be self-generated. We also assume that the fluid being displaced is of negligible viscosity and density. The flow in this region is therefore not solved for and instead is treated as a space of constant pressure. As in Saffman-Taylor, we seek wave numbers of unstable perturbations, with a maximal growth rate corresponding to a typical finger thickness. In wound healing assays, fingers can be as few as five to ten cells thick, thus it is not clear if a continuum

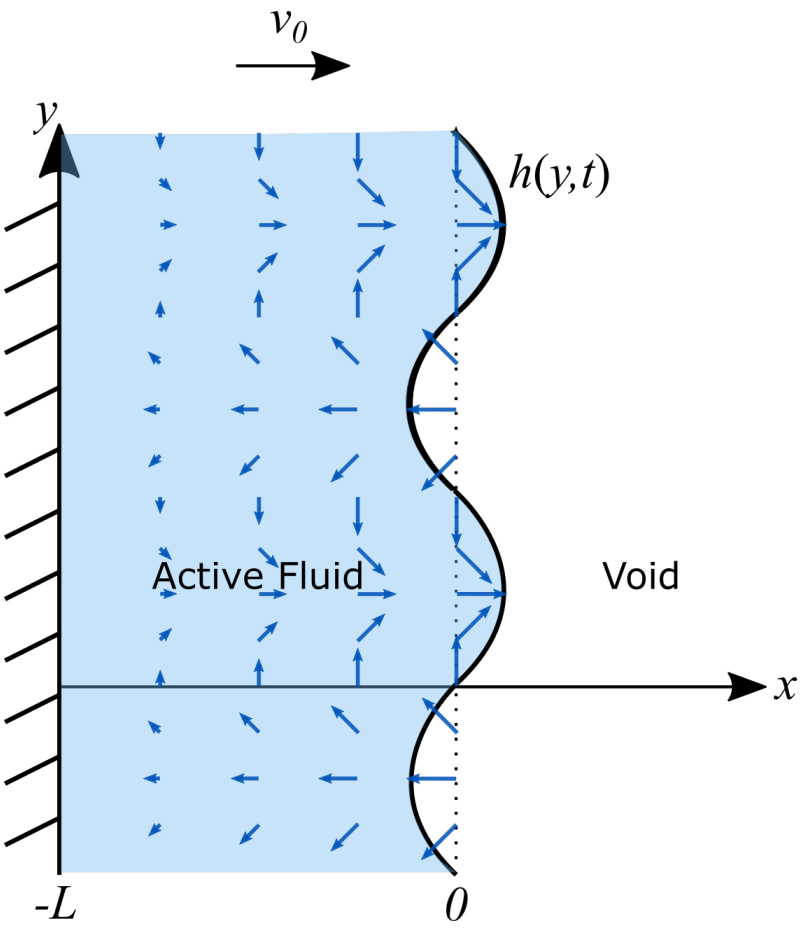

Figure 4.1: Schematic of the model geometry. A two dimensional strip, with thickness L, of active fluid, bounded between a solid wall and an empty void, is permitted to move with speed v_0 in the direction of the void. The trailing wall co-moves with the bulk fluid.

model will be able to replicate these, although both [75] and [6] observe finger formation using continuum models.

It was claimed that the following set of equations are sufficient to generate the fingering behaviour [6]:

$$\rho\left(\frac{\partial \mathbf{u}}{\partial t} + \lambda\left(\mathbf{u}\cdot\nabla\right)\mathbf{u}\right) = \mu\nabla^2\mathbf{u} - \nabla p + a\mathbf{u} - b|\mathbf{u}|^2\mathbf{u}\ , \tag{4.1a}$$

$$\nabla\cdot\mathbf{u} = 0\ , \tag{4.1b}$$

where ρ and $\mathbf{u}$ are the density and flow field of the active fluid respectively; p is the pressure and μ a viscosity. These are a simpler version of the Toner-Tu equations given in Eq. (1.1). Eq. (4.1a) is the incompressibility condition, which eliminates many of the non-linear terms in Eq. (1.1b). The pressure is now isotropic and simply a Lagrangian multiplier to enforce incompressibility.

The two terms $a\mathbf{u}$ and $b|\mathbf{u}|^2\mathbf{u}$ account for the activity, where a and b are constants. Each of these acts in a direction tangential to the instantaneous velocity of the fluid. The former acts as a driving term with $a > 0$ inherently assuming that the propulsion forces within the fluid align with the instantaneous velocity; $a < 0$ means that the active forces are acting against the motion. The non-linear term $b|\mathbf{u}|^2\mathbf{u}$ provides resistance, preventing arbitrary growth, hence $b > 0$ necessarily.

As mentioned, this is a dry model and momentum is not conserved [1]. Furthermore Galilean invariance does not apply and the prefactor of the advective term, λ, need not be unity. The underlying assumption justifying this model is that the mechanics of the cells are dominated by interaction with the substrate, specifically through their ability to crawl. The active terms in Eq. (4.1a) prescribe a preferred speed for the fluid to move at, much like the cells crawling on the substrate, but there is no preferred direction. The fluid is simply accelerated or decelerated in the direction it is already moving. This effectively assumes that cells move in the net direction of their neighbours, and tend to realign their own velocities to match this direction. Assuming that the net result gives a non-trivial polar order, upon taking the hydrodynamic limit the polar order dominates, thus higher order effects such as nematic order are negligible in this minimal model [137].

Mass is conserved in the active fluid via the incompressibility condition Eq. (4.1b) and the density ρ is assumed to be constant — a fair assumption, as cell division and death rates are low in comparison with the effects of motility forces in wound healing assays [6, 69].

Eq. (4.1) is rich in physics: it has been shown that the fluctuating form of the equation is connected to the Kardar-Parisi-Zhang model in 2D [138] and its associated critical behaviour is described by a novel universality class in non-equilibrium physics [129]. Here, we will focus on the stability criteria

when an interface is present.

We now perform a linear stability analysis on these equations using the geometry depicted in Fig. 4.1: a strip of active fluid of thickness L, bounded by a solid wall on one side with an open interface on the other. The fluid is assumed to move with a constant uniform base flow v_0 in the direction of the open interface, with the rear wall co-moving with the fluid. In such a homogeneous flow, $\mathbf{u} = v_0\hat{\mathbf{x}}$, all of the derivatives in Eq. (4.1) vanish, leaving a balance between the active terms. The solution $v_0 = 0$ exists for all real a, however $a > 0$ has the additional solution: $v_0 = \sqrt{a/b}$. We will refer to the $v_0 = 0$ case as the *stationary case* and to $v_0 > 0$ as the *moving case*.

We add a small perturbation to this flow $\mathbf{u} = (v_0 + u_x)\hat{\mathbf{x}} + u_y\hat{\mathbf{y}}$ and the interface $h = v_0 t + \tilde{h}$, where $|\tilde{h}|, |u_x|, |u_y| \ll 1$. We consider sinusoidal perturbations with wave number q, using the form

$$u_x = A\mathrm{e}^{r(x-v_0t)+\omega t+\mathrm{i}qy} \tag{4.2a}$$

$$u_y = B\mathrm{e}^{r(x-v_0t)+\omega t+\mathrm{i}qy} \tag{4.2b}$$

$$p = C\mathrm{e}^{r(x-v_0t)+\omega t+\mathrm{i}qy} \tag{4.2c}$$

$$\tilde{h} = h_0\mathrm{e}^{\omega t+\mathrm{i}qy} \tag{4.2d}$$

so that the real part of ω describes the growth rate of the mode, with a positive value corresponding to instability.

Substituting Eq. (4.2) into Eq. (4.1) gives, to linear order,

$$\rho\left(\omega + (\lambda-1)v_0 r\right)A = -rC + \mu(r^2-q^2)A + (a - 3bv_0^2)A \ , \tag{4.3a}$$

$$\rho\left(\omega + (\lambda-1)v_0 r\right)B = -\mathrm{i}qC + \mu(r^2-q^2)B + (a - bv_0^2)B \ , \tag{4.3b}$$

$$rA + \mathrm{i}qB = 0 \ . \tag{4.3c}$$

This is a homogeneous system of linearised equations in the constants A, B and C. As such, it can be expressed in the form of a matrix equation

$$M_1\mathbf{A} = \mathbf{0} \ , \tag{4.4}$$

where $\mathbf{A} = (A, B, C)^T$. For the solution to be non-trivial, the determinant

of the matrix of coefficients, M_1, must be zero. This restricts the values of r to be the roots of the quartic polynomial

$$\begin{aligned} 0 = {} & \mu r^4 + \rho\,(1-\lambda)\,v_0 r^3 - \left[\rho\omega + 2\mu q^2 - \left(a - bv_0^2\right)\right] r^2 \\ & - \rho\,(1-\lambda)\,v_0 q^2 r + q^2\left[\mu q^2 + \rho\omega - \left(a - bv_0^2\right) + 2bv_0^2\right] \ . \end{aligned} \tag{4.5}$$

Hence the general solution for the velocity perturbation is

$$u_x = \sum_{j=1}^{4} A_j \mathrm{e}^{r_j(x - v_0 t) + \omega t + \mathrm{i}qy} \tag{4.6}$$

where r_j are the four roots in Eq. (4.5). The other perturbation fields u_y and p can also be expressed in terms of A_j by referring back to Eq. (4.3).

The remaining unknowns A_j and h_0 are fixed by the boundary conditions. No-slip is applied at the rear wall, meaning all velocity perturbations (u_x, u_y) in the flow field must decay this far from the interface and thus at the rear wall $x = v_0 t - L$

$$u_x\Big|_{x=v_0t-L} = u_y\Big|_{x=v_0t-L} = 0 \ . \tag{4.7}$$

The velocity of the interface $h(y,t)$ must be continuous with the flow field. Linearised at the free surface equilibrium, $x = v_0 t$, this becomes

$$\frac{\partial \tilde{h}}{\partial t} = u_x\Big|_{x=v_0t} \ . \tag{4.8}$$

The fluid occupying the void region in Fig. 4.1 is of negligible viscosity compared to that of the active fluid. Hence this region is not solved for and is assumed to be of constant pressure. Therefore the tangential stress on the interface must be zero, Eq. (4.9a). The normal stress must be balanced by the surface tension γ and the pressure difference across the interface, Eq. (4.9b). Linearised about $x = v_0 t$ these conditions are

$$\frac{\partial u_x}{\partial y}\bigg|_{x=v_0t} + \frac{\partial u_y}{\partial x}\bigg|_{x=v_0t} = 0 \ , \tag{4.9a}$$

$$2\mu \frac{\partial u_x}{\partial x}\bigg|_{x=v_0t} - p|_{x=v_0t} = \gamma \frac{\partial^2 \tilde{h}}{\partial y^2} \ . \tag{4.9b}$$

The five boundary conditions give another system of homogeneous linear equations, this time in terms of the four A_j and h_0. After factoring some arbitrary non-zero terms, such as the complex number i and $\exp(\mathrm{i}q+\omega t)$, out of the equations, the system can be expressed as

$$M_2\mathbf{v} = \mathbf{0} \tag{4.10}$$

where

$$M_2 = \begin{pmatrix} \mathrm{e}^{-Lr_1} & \mathrm{e}^{-Lr_2} & \mathrm{e}^{-Lr_3} & \mathrm{e}^{-Lr_4} & 0 \\ \frac{r_1}{q}\mathrm{e}^{-Lr_1} & \frac{r_2}{q}\mathrm{e}^{-Lr_2} & \frac{r_3}{q}\mathrm{e}^{-Lr_3} & \frac{r_4}{q}\mathrm{e}^{-Lr_4} & 0 \\ 1 & 1 & 1 & 1 & -\omega \\ \frac{r_1^2+q^2}{q} & \frac{r_2^2+q^2}{q} & \frac{r_3^2+q^2}{q} & \frac{r_4^2+q^2}{q} & 0 \\ c_1 & c_2 & c_3 & c_4 & \gamma q^2 \end{pmatrix} , \tag{4.11}$$

$$c_j = \frac{\mu r_j(3q^2 - r_j^2) + (\rho\omega - (a - bv_0^2))r_j + \rho v_0(1-\lambda)r_j^2}{q^2} , \tag{4.12}$$

and $\mathbf{v} = (A_1, A_2, A_3, A_4, h_0)^T$. Again, for a non-trivial solution the matrix of coefficients, M_2, must have zero determinant. Since the r_j's are the roots of Eq. (4.5), and thus determined by ω and q, the determinant $f(\omega, q) = \det M_2$ is a function of ω and q. The problem is reduced to finding roots of $f(\omega, q)$ for the two cases.

4.2 The unstable stationary case

In the stationary case, $v_0 = 0$, factoring out non-zero constants reduces $f(\omega, q) = 0$ to

$$\begin{aligned} 0 =& \frac{\mu\omega}{\gamma}\Bigg\{ -k\cosh(L(k-q))\frac{\rho^2}{\mu^2}\left(\omega - \frac{a}{\rho}\right)^2 \\ &+ k\Big(1-\cosh(L(k-q))\Big)\left[8q^4 + 4q^2\frac{\rho}{\mu}\left(\omega - \frac{a}{\rho}\right)\right] \\ &- \sinh(Lk)\sinh(Lq)(k-q)^2\left(k^3 + k^2q + 3kq^2 - q^3\right)\Bigg\} \\ &- \frac{\rho}{\mu}\left(\omega - \frac{a}{\rho}\right)q^3\Big\{k\cosh(Lk)\sinh(Lq) - q\sinh(Lk)\cosh(Lq)\Big\} \end{aligned} \tag{4.13}$$

where

$$k = +\sqrt{q^2 + \frac{\rho}{\mu}\left(\omega - \frac{a}{\rho}\right)}. \tag{4.14}$$

We first consider the long wavelength limit (small q). Expanding the terms in powers of q we obtain an asymptotic expansion for ω:

$$\omega = \frac{a}{\rho} - \frac{\mu}{\rho L^2}\left(n\pi + \frac{\pi}{2}\right)^2 + \frac{\mu}{\rho}\left(1 + \frac{16(-1)^{n+1}}{(1+2n)\pi}\right)q^2 + O(q^4) \tag{4.15}$$

where n is any integer. It follows that ω is real for sufficiently small q. Our numerical calculations suggest that this holds for all real q and we will assume that ω is real henceforth.

With this assumption we can show by contradiction that ω is bounded above by a/ρ. If we assume that ω is greater than a/ρ, Eq. (4.14) implies that $k > q$. Upon inspection we find that each line of Eq. (4.13) is strictly negative, and thus the right hand side cannot be zero. This means there are no solutions for $\omega > a/\rho$. This in particular resolves the diverging growth rate encountered in [6]. Conveniently it also provides a finite range in which to numerically search for unstable modes.

Fig. 4.2(a) depicts the full unstable solution for the parameter values given in Table 4.1, obtained by solving $f(\omega, q) = 0$ numerically. Where necessary,

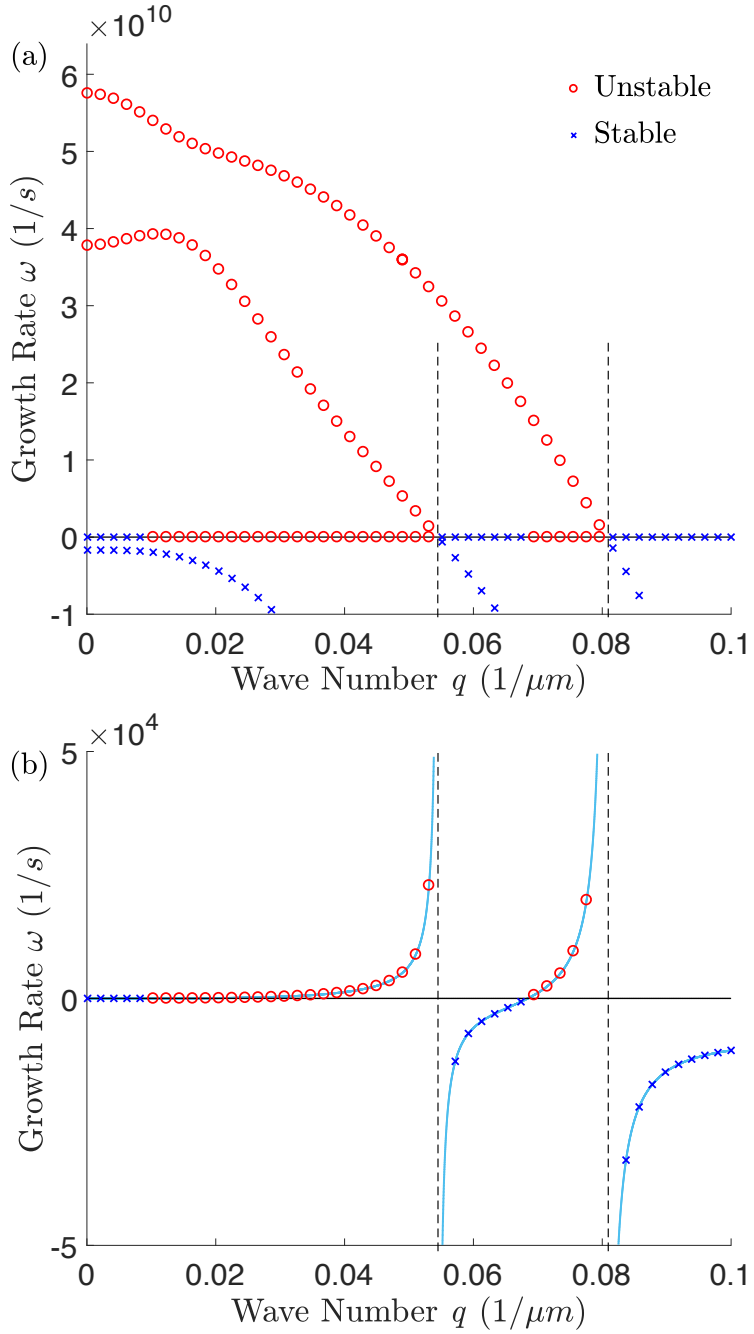

Figure 4.2: Stability diagram for the stationary case: $v_0 = 0$. Red circles (blue crosses) indicate unstable (stable) solutions. Plot (b) is the same as (a) but focused on a smaller range of ω. The solid blue curves in (b) show the results obtained when the inertial terms are ignored [6]. Although the solution curves in (a) appear to smoothly cross $\omega = 0$, we can see from (b) that the curves in fact turn sharply, and do not cross the dashed lines. Parameter values are given in Table 4.1.

we have excluded the zeros of f corresponding to degenerate cases of Eq. (4.5). These must be treated separately to determine if they are genuine solutions. As it so happens none of these are legitimate solutions, and can be safely disregarded. See Section 4.2.1 for details.

Parameter	Value	References
ρ	10^3 kgm^{-3}	-
μ	10^4 Pa s	[139, 140]
γ	10^3 Pa μm	[141]
L	100 μm	[71]
$\sqrt{a/b}$	2.7×10^{-3} μm s^{-1}	[69]
a	60 Pa s μm^{-2}	[6]
b	10^7 Pa s^3μm^{-4}	[6]
λ	1	-

Table 4.1: Values of parameters used, chosen to be physiologically relevant to epithelial cells. The density of water was used for ρ as this is a reasonable approximation for cells. For a and b, we use the values employed in [6]. As we discuss, this value of a is likely too large to be physiologically realistic. λ is a dimensionless coefficient. For simplicity we take $\lambda = 1$, meaning the LHS of Eq. (4.1b) is the material derivative of $\mathbf{u}$.

As the growth rate is now bounded above by a/ρ, there are no singularities as discussed in [6], and we seek the wave number that provides the largest growth rate. The highest curve outlined in Fig. 4.2(a) appears to obtain its maximum in the limit as $q \to 0$. This is in accord with the expansion in Eq. (4.15) – the constant part of ω is largest when $n = 0$, at which point the coefficient of the next lowest order term, q^2, is negative. As such the growth rate initially decays away from its peak at $q = 0$. The actual value $q = 0$ is not a valid mode. This would correspond to a flat wave, which would necessarily violate conservation of mass if it were to grow.

To understand why the most unstable mode occurs as $q \to 0$, recall that there is no external pressure, and the only driving force in our system is the internally generated active force $a\mathbf{u}$. This force provides the same growth rate for all wave numbers q. The motion is resisted by viscosity and surface tension. The strength of each of these increases with q, thus suggesting that

the maximum growth should be in their absence, namely in the limit $q \to 0$.

Viscosity counteracts shear within the velocity field. Due to the no-slip condition at the rear wall coupled with the incompressibility condition, any velocity perturbation at the free surface naturally induces shear throughout the fluid, as depicted schematically in Fig. 4.1. As q drops to zero, the shear due to variation in the $y-$direction becomes negligible, however the shear in the $x-$direction remains, as the velocity must vanish across the width L. Hence the very minimum we require for any perturbation to grow, is for the driving force $a\mathbf{u}$ to be stronger than the viscosity component corresponding to the latter direction, $\mu\partial^2\mathbf{u}/\partial x^2$. We therefore expect instability to occur only if

$$aU > C\frac{\mu U}{L^2}, \tag{4.16}$$

for some unknown dimensionless constant C. We can quantify C by returning to the asymptotic expansion (4.15). Since $\max_q \omega$ is achieved for $n = 0$ as $q \to 0$, we indeed find that the stationary case is linearly unstable only if

$$\frac{aL^2}{\mu} > \frac{\pi^2}{4}. \tag{4.17}$$

Hence we have a condition for instability. Evidently a negative value of a implies the system is stable – an expected result as both active terms would be acting against the motion.

Fig. 4.2(b) focuses on a region of much smaller ω. Also plotted are the results obtained using the analysis of [6]. Within this region the solutions actually align very well, revealing that their simplification to ignore the inertial terms in their analysis is valid when $|\omega|$ is 'small'. We can clarify the meaning of small by returning to the governing equation (4.1a). Deeming $\rho\,\partial\mathbf{u}/\partial t$ to be negligible with respect to $a\mathbf{u}$ is to assume that $|\omega| \ll a/\rho$, hence their solution is valid only within this region. Ultimately this means that although the flow has a very small Reynolds number Re, it also has a very small Stokes number St, which are given by the ratios

$$\mathrm{Re} = \frac{\rho\,(\mathbf{u}\cdot\nabla)\,\mathbf{u}}{\mu\nabla^2\mathbf{u}} \qquad \text{and} \qquad \mathrm{St} = \frac{(\mathbf{u}\cdot\nabla)\,\mathbf{u}}{\partial\mathbf{u}/\partial t}. \tag{4.18}$$

If St $\sim \mathcal{O}(1)$ and Re $\ll 1$, both of the terms $(\mathbf{u}\cdot\nabla)\,\mathbf{u}$ and $\partial\mathbf{u}/\partial t$ would be negligible, however in this case only the former is.

4.2.1 Degenerate solutions

Some roots of $f(\omega, q)$ are not solutions to our system. If any of the columns of the matrix M_2 are identical, then the determinant is trivially zero. This occurs if any of the roots r_j are repeated, that is, if the quartic Eq. (4.5) is degenerate. This situation arises along a small number of curves, $\omega_i = \omega_i(q)$. In these cases the form of the general solution is no longer given by Eq. (4.6), and M_2, as given in Eq. (4.11), is not valid. Therefore $f(\omega, q)$ cannot be used to determine whether or not $\omega_i(q)$ is a solution; f is trivially zero. The analysis must be repeated in these cases, using the correct general solution and deriving a new $f_i(\omega_i(q), q)$. This new function depends only on q, so the solutions we seek are pairs $(\omega_i(q^*), q^*)$ where $f_i(\omega_i(q^*), q^*) = 0$. Here we derive the conditions for degeneracy and analyse them in turn.

For $v_0 = 0$, Eq. (4.5) reduces to

$$\mu r^4 - (\rho\omega + 2\mu q^2 - a)r^2 + q^2(\mu q^2 + \rho\omega - a) = 0 \tag{4.19}$$

hence

$$r^2 = q^2 + \frac{(\rho\omega - a) \pm (\rho\omega - a)}{2\mu}\ . \tag{4.20}$$

This is degenerate in two cases

$$\omega_1 = \frac{a}{\rho} \quad , \quad \omega_2 = \frac{a}{\rho} - \frac{\mu}{\rho}q^2\ . \tag{4.21}$$

In what follows, let $u_x = \mathrm{e}^{\mathrm{i}qy+\omega t}\tilde{u}_x(x - v_0 t)$, and similarly for u_y and p.

Degenerate case: $\omega_1 = a/\rho$

The general solution is

$$\tilde{u}_x = (A_1 + A_2 x)\mathrm{e}^{qx} + (A_3 + A_4 x)\mathrm{e}^{-qx}. \tag{4.22}$$

The corresponding $\tilde{u}_y$ and $\tilde{p}$ are obtained from Eq. (4.1) and given by

$$\tilde{u}_y = \frac{\mathrm{i}}{q}\left[(A_1 q + A_2(1+qx))\mathrm{e}^{qx} - (qA_3 + A_4(-1+qx))\mathrm{e}^{-qx}\right], \tag{4.23}$$

$$\begin{aligned}\tilde{p} = \frac{1}{q^2}\Big\{ & A_1 q(a-\omega\rho)\mathrm{e}^{qx} + A_2\left[(a-\omega\rho)(1+qx) + 2q^2\right]\mathrm{e}^{qx} \\ & - A_3 q(a-\omega\rho)\mathrm{e}^{-qx} + A_4\left[(a-\omega\rho)(1-qx) + 2q^2\right]\mathrm{e}^{-qx}\Big\}.\end{aligned} \tag{4.24}$$

As before the boundary conditions provide a linear system of equations in A_j and h_0. The determinant of the matrix of coefficients must be zero, which reduces to

$$0 = 2 + 4(Lq)^2 + 2\cosh 2Lq + \frac{\rho\gamma}{a\mu}\left(q\sinh(2Lq) - 2(Lq)^2\right) \ . \tag{4.25}$$

This equation has no solutions for any real q regardless of the parameter values, hence the root $\omega_1 = a/\rho$ can be disregarded.

Degenerate case: $\omega_2 = a/\rho - (\mu/\rho)q^2$

The general solution is

$$\tilde{u}_x = A_1\mathrm{e}^{qx} + A_2\mathrm{e}^{-qx} + A_3 x + A_4. \tag{4.26}$$

The corresponding $\det M_2 = 0$ reduces to

$$\begin{aligned}0 = & \frac{\mu}{\rho}(\mu q^2 - a)(4 - 5\cosh(Lq) + Lq\sinh(Lq)) \\ & + \gamma q(Lq\cosh(Lq) - \sinh(Lq)) \ .\end{aligned} \tag{4.27}$$

It is not obvious how many solutions there are to this equation, if any at all; it depends heavily on the parameter values. For the values used in Fig. 2 there are exactly two solutions for which $\omega_2 > 0$. These match the points where the curve $\omega_2 = a/\rho - (\mu/\rho)q^2$ intersects the curves obtained from the non-degenerate cases. Assuming this result applies for all parameter sets, we could garnish information about the full solution from the number of valid points on the degenerate curve $\omega_2(q)$. For example, if there are no such

solutions to Eq. (4.27), then we can conclude that all of the unstable solution curves are bounded below $\omega = a/\rho - (\mu/\rho)q^2$. Otherwise we would have discontinuities in our full solution.

4.3 The stable moving case

In the case $v_0 = \sqrt{a/b}$ the roots of Eq. (4.5) cannot be written explicitly in a useful format, hence we present only numerical results. As all numerical solutions obtained found ω to be real, we assume that this is true generally. As for the stationary case, ω has multiple values for each q, all of which were negative, implying that the moving case is stable. There are also degenerate cases which were found to be removable as detailed in Section 4.3.1. Fig. 4.3 displays the highest roots found for the tested values of q, plotted alongside the original results obtained using the analysis of [6]. They align very well, confirming that the inertial terms have little effect on the dominant behaviour of the solution in the moving case, and it is always stable.

As with the stationary case, by ignoring the inertial terms in [6], their results are single valued, and the branch obtained is that with the smallest values of $|\omega|$.

4.3.1 Degenerate solutions

In the moving case, $v_0 = \sqrt{a/b}$, the quartic equation (3) cannot be solved in a useful format for general parameters, hence for simplicity we restrict our attention to the special case $\lambda = 1$. Therefore Eq. (4.5) becomes

$$\mu r^4 - (\rho\omega + 2\mu q^2)r^2 + q^2(\mu q^2 + \rho\omega + 2a) = 0 \ , \tag{4.28}$$

so

$$r^2 = \frac{1}{2\mu}(\rho\omega + 2\mu q^2 \pm \sqrt{\rho^2\omega^2 - 8\mu a q^2}). \tag{4.29}$$

Roots are repeated in the cases

$$\omega_3 = -\frac{2a}{\rho} - \frac{\mu}{\rho}q^2 \quad , \quad \omega_\pm = \pm\frac{\sqrt{8\mu a}}{\rho}q \ . \tag{4.30}$$

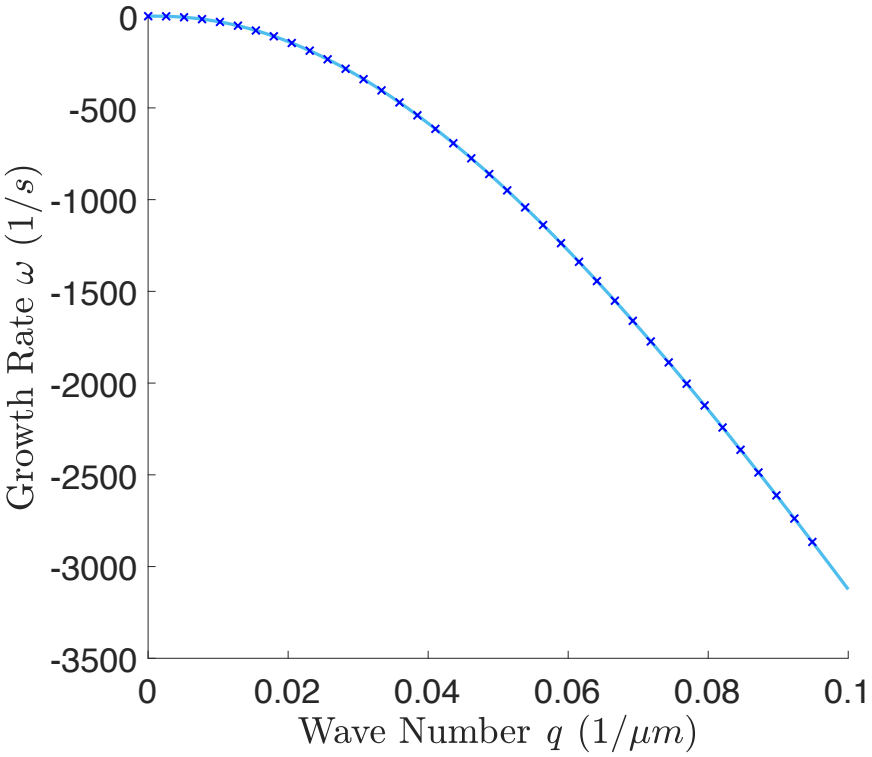

Figure 4.3: Stability diagram for the moving case ($v_0 = \sqrt{a/b}$) showing the growth rate versus the wave number of the perturbation. Results are numerical (crosses) and plotted alongside the solution obtained after ignoring inertial terms (curve) [6]. Parameter values are given in Table 4.1.

The former provides only negative values of ω, which are stable and thus do not require further analysis. Therefore, for the moving case there is only one potentially unstable degenerate case, namely

$$\omega_+ = \sqrt{8\mu a}q/\rho \ . \tag{4.31}$$

As before let $u_x = \mathrm{e}^{\mathrm{i}qy+\omega t}\tilde{u}_x(x - v_0 t)$, and similarly for u_y and p. The general solution has the form

$$\tilde{u}_x = (A_1 + A_2(x - v_0 t))\mathrm{e}^{r(x-v_0 t)} + (A_3 + A_4(x - v_0 t))\mathrm{e}^{-r(x-v_0 t)} \tag{4.32}$$

where r is the positive solution to

$$r^2 = q^2 + \sqrt{2a/\mu}\, q. \tag{4.33}$$

It is not apparent what the corresponding $\tilde{u}_y$ and $\tilde{p}$ are, so we assume:

$$\tilde{u}_y = (\hat{B}_1 + \hat{B}_2)\mathrm{e}^{r\xi} + (\hat{B}_3 + \hat{B}_4)\mathrm{e}^{-r\xi}, \tag{4.34}$$

$$\tilde{p} = (\hat{C}_1 + \hat{C}_2)\mathrm{e}^{r\xi} + (\hat{C}_3 + \hat{C}_4)\mathrm{e}^{-r\xi}, \tag{4.35}$$

where the $\hat{B}_j$ and $\hat{C}_j$ are all *functions* of $\xi = x - v_0 t$, and relate directly to A_j, for each j respectively. Using the incompressibility condition we obtain

$$\tilde{B}_1 = \frac{\mathrm{i}r}{q} A_1 \quad , \quad \tilde{B}_2 = \frac{\mathrm{i}(1 + r\xi)}{q} A_2 \ , \tag{4.36}$$

$$\tilde{B}_3 = -\frac{\mathrm{i}r}{q} A_3 \quad , \quad \tilde{B}_4 = \frac{\mathrm{i}(-1 + r\xi)}{q} A_4 \ . \tag{4.37}$$

By substituting $\tilde{B}_j$ into the momentum equation for u_y, we can obtain

$$\tilde{C}_1 = -\frac{r(\mu(q^2 - r^2) + \rho\omega)}{q^2} A_1 \ , \tag{4.38}$$

$$\tilde{C}_2 = -\frac{(\mu(q^2 - r^2) + \rho\omega)(1 + r\xi) - 2\mu r^2}{q^2} A_2 \ , \tag{4.39}$$

$$\tilde{C}_3 = \frac{r(\mu(q^2 - r^2) + \rho\omega)}{q^2} A_3 \ , \tag{4.40}$$

$$\tilde{C}_4 = -\frac{(\mu(q^2 - r^2) + \rho\omega)(1 - r\xi) - 2\mu r^2}{q^2} A_4 \ . \tag{4.41}$$

Applying the boundary conditions and factoring out constants, we get a matrix system $M\mathbf{v} = 0$ as before, this time:

$$M = \begin{pmatrix} \mathrm{e}^{-Lr} & -L\mathrm{e}^{-Lr} & \mathrm{e}^{Lr} & -L\mathrm{e}^{Lr} & 0 \\ r\mathrm{e}^{-Lr} & (Lr-1)\mathrm{e}^{-Lr} & -r\mathrm{e}^{Lr} & (Lr+1)\mathrm{e}^{Lr} & 0 \\ -1 & 0 & -1 & 0 & \omega \\ r^2 + q^2 & 2r & r^2 + q^2 & -2r & 0 \\ c_1 & c_2 & -c_1 & c_2 & \gamma q^2 \end{pmatrix} \tag{4.42}$$

where

$$c_1 = r(\mu(3q^2 - r^2) + \rho\omega) \ , \tag{4.43}$$

$$c_2 = 3\mu(q^2 - r^2) + \rho\omega \ . \tag{4.44}$$

Once again the determinant of this matrix must be zero, explicitly

$$\begin{aligned} 0 = {} & 2\gamma q^4 r(2\sinh 2Lr - 4Lr) \\ & + \mu\omega \left\{ r^4(2\cosh 2Lr + 14 - 4L^2r^2) \right. \\ & \qquad + q^2 \left[r^2(8L^2r^2 + 12\cosh 2Lr - 12) \right. \\ & \qquad\quad \left. \left. + q^2(12L^2r^2 + 6 - 6\cosh 2Lr) \right] \right\} \\ & + \omega^2\rho \left\{ r^2(2\cosh 2Lr - 2 + 4L^2r^2) \right. \\ & \qquad \left. - q^2(2\cosh 2Lr - 2 - 4L^2r^2) \right\} . \end{aligned} \tag{4.45}$$

By examining each of these lines we can deduce that there are no solutions. Recall that all of our parameters are positive, including r, q and ω. By inspection the first two lines are strictly positive individually. The square brackets straddling lines 3 and 4 are also strictly positive, seen using the fact that $r^2 > q^2$ from Eq. (4.33). Similarly the curly brackets straddling lines 5 and 6 are also strictly positive. Hence there is no way that the expression on the right hand side can be zero, so we conclude that the degenerate root $\omega_+ = +\sqrt{8\mu a}q/\rho$ is not a solution to our system, and can be disregarded from numerical results.

4.4 Relevance to wound healing

We have performed a linear stability analysis on a strip of incompressible active fluid governed by the hydrodynamic equations of motion in Eq. (4.1) about a stationary system and a constant uniform flow. The fluid density was assumed to be constant and uniform.

Our results for the moving case, with speed $\sqrt{a/b}$, were no different from those in [6], and the system is always linearly stable, at least for the case $\lambda = 1$.

We found that from a stationary position, the interface can be unstable, subject to the criterion in Eq. (4.17), and recognised that it describes a balance between the viscosity and active driving force. However, we have concluded that the most unstable mode is simply the largest wavelength that the domain permits; our model assumed the strip to be infinitely long, hence no restriction was placed on the wave number. In the context of wound healing, our model suggests that the typical thickness for the growing fingers will be of the system size. Our results are qualitatively different from those obtained in [6], due to the inclusion of the inertial terms in our analysis.

Given that the cells in a wound healing assay would be starting from an equilibrium state, the stationary case is far more relevant. As such, the existence of an instability is promising, but the lack of a maximal mode would ultimately suggest that our incompressible active fluid model is insufficient to produce the fingering behaviour exhibited in wound healing experiments. Furthermore, using physiologically relevant parameters (see caption of Fig. 4.2), the minimal a required for instability is 2.5 Pa s μm^{-2} according to Eq. (4.17). However, in a typical experiment the time scale is of the order of hours. If we assume that it takes one hour to achieve a steady state, we would expect dimensionally for ρ/a to be about one hour. Using the same value of ρ, the density of water, a would therefore be of the order of 2.8×10^{-13} Pa s μm^{-2}. This is many orders of magnitude smaller than the minimum required for instability, explaining why instabilities of the order of the system size are not observed in experiments. Note that the actual density of the cell layer never needs to be incorporated into the analysis in [6] since the L.H.S. of Eq. (4.1) is set to zero.

Our work thus strongly indicates that compressibility of the tissue is critical for fingering instability. Indeed, examining wound healing assays reveals a stark difference between the typical diameter of a cell in the bulk of the tissue, and that of a cell in the finger-like protrusions, with the latter being significantly larger [71]. Even without an interface, the velocities of cells within a confluent layer have been shown to vary with cell density [48]. All of these suggest variations in the cell density should not be ignored.

Our work has relevance beyond tissue regeneration. Since we have shown

that the boundary perpendicular to the moving direction of 2D incompressible active fluids is stable, our work suggests that the recent predictions on the scaling behavior of incompressible active fluids in the moving phase [138] may be studied on an open system, thus potentially facilitating the experimental verification of the theory.

Finally, the results for the moving case may also have some relevance to our work in Chapter 3. Although the system simulated in Chapter 3 is compressible, under certain conditions phase separation occurs, in which an aligned band of roughly uniform density propagates through a much more dilute region at a constant speed. The resulting image is similar to Fig. 4.1 with a second open interface instead of the fixed wall, and a dilute medium in place of the void. Crucially this band is stable in time, in agreement with the moving phase in this study.

Chapter 5

Conclusions

5.1 Summary of results

In this thesis we developed a new lattice Boltzmann method for simulating dry polar active fluids, with attention focused to the behaviour at comparatively high densities. This was achieved by intentionally breaking conservation of momentum, necessarily rendering the hydrodynamics of our system in the realm of the Toner-Tu equations. We confirmed this using a Chapman-Enskog analysis, and furthermore derived the relationships between the system parameters and the corresponding coefficients of the macroscopic equations. We used our method to successfully simulate two types of behaviour associated with dry active fluids, namely motility-induced phase separation and collective motion, producing phase diagrams for each. By incorporating contact inhibition of locomotion into our collective motion model we uncovered two new first order transitions at high densities, and a potentially new critical transition. By performing a stability analysis on the corresponding Toner-Tu equations, we were able to interpret this result analytically, and derived the conditions for this critical behaviour to occur.

In addition we performed a stability analysis on an open interface of a strip of fluid described by an incompressible version of the Toner-Tu equations. The strip was found to be stable if moving at a fixed speed, which is consistent with our observations from the CIL model, where stable dense

bands propagate through a disordered sparse phase. The strip was found to be unstable if initially stationary, however in contrast to the conclusions of a previous study, the most unstable mode was found to be the longest wavelength limit, thereby implying there is no characteristic wavelength developed by the instability. This contradicts the claim that the incompressible system could describe the observed fingering instability in wound healing assays, however it remains possible that a compressible system may be able to produce this instability.

5.2 Future work

By far the most significant and most unexpected results of our work was the discovery of two new first order phase transitions and in particular, a potentially new critical behaviour. As mentioned, we believe this to be a new form of critical behaviour associated with active matter, however more detailed investigation is required to confirm this beyond doubt. This would involve determining the critical exponents, a task which we believe our LBM is ideal for performing. Our LBM is already quick to run, and has the capability of being parallelised to enhance the speed further.

We have also demonstrated our LBM to be adaptable to other active systems, with its ability to generate MIPS. Since the computational time of our model does not depend on the density of the system, our model is potentially more efficient than comparable molecular dynamics models, especially at high densities. However, we have not performed any rigorous complexity comparisons or speed tests to confirm this.

Through our Chapman-Enskog analysis, we have derived a clear link between our system parameters, and those of the overarching Toner-Tu equations. Not only is this beneficial for the particular systems that we investigated, permitting us to interpret our results through stability analysis, it also paves the way for future studies of other systems, such as chiral active matter. By understanding the relationship between the choice of $\mathbf{u}^*$, and the forcing term $\mathbf{F}$, we can not only quickly the derive the corresponding Toner-Tu equations for any alternative choice of $\mathbf{u}^*$, but can also reverse-engineer

a particular choice of Toner-Tu equations to obtain the required form of $\mathbf{u}^*$ so as to be simulated by our LBM.

For the purposes of this study, periodic boundary conditions were sufficient, however our LBM can also be expanded to include more complicated boundary conditions using the standard methods developed for LBMs. No-slip, impermeable walls are particularly easy to implement, meaning the method is well suited to simulate flow in complex geometries.

Although our systems of interest began as a single homogeneous phase, they naturally separate into multiple phases. Our method could also be adapted to simulate other types of multiphase flows, such as a mixture of two or more different fluids, perhaps even related by chemical reactions. In particular one could surely reproduce the system described in Chapter 4, which could be viewed as phase separation between two immiscible fluids, one of which is active. This could provide further insight into the behaviour of a dry polar active fluid, starting from rest, and could verify the conclusions of our stability analysis for the stationary case by incorporating compressibility effects.

Finally, we adapted $\mathbf{u}$ in the definition of f_i^{eq}, in order to break conservation of momentum, however we preserved conservation of mass. By adopting a similar approach for the density ρ, we could also expand our method to simulate systems which do not respect conservation of mass, such as cell division in a spreading epithelial sheet. Furthermore, by preserving the form of f_i^{eq}, which is derived from the Maxwell-Boltzmann distribution for particle velocities at thermodynamic equilibrium, we assumed that active particles generate a similar distribution. It raises the question over what other distributions could be used, and which systems do they represent. Further work could be performed on active molecular dynamics models to determine the corresponding distribution, linking the microscopic and mesoscopic pictures. However, we emphasise that the macroscopic (hydrodynamic) picture will be largely unchanged, as long as the key symmetries are preserved.

The advent of lattice Boltzmann methods made particle simulations for passive fluids effectively obsolete. We cannot predict what the future holds for the study of active matter, but we expect that the lattice Boltzmann

methods developed here will continue to prove both useful and fruitful in the uncovering of new results.

Bibliography

[1] M. C. Marchetti, J. F. Joanny, S. Ramaswamy, T. B. Liverpool, J. Prost, M. Rao, and R. A. Simha, "Hydrodynamics of soft active matter," *Rev. Mod. Phys.*, vol. 85, no. 3, pp. 1143–1189, 2013.

[2] M. Ballerini, N. Cabibbo, R. Candelier, A. Cavagna, E. Cisbani, I. Giardina, V. Lecomte, A. Orlandi, G. Parisi, A. Procaccini, M. Viale, and V. Zdravkovic, "Interaction ruling animal collective behavior depends on topological rather than metric distance: Evidence from a field study," *Proc. Natl. Acad. Sci.*, vol. 105, no. 4, pp. 1232–1237, 2008.

[3] Y. Katz, K. Tunstrom, C. C. Ioannou, C. Huepe, and I. D. Couzin, "Inferring the structure and dynamics of interactions in schooling fish," *Proc. Natl. Acad. Sci.*, vol. 108, no. 46, pp. 18720–18725, 2011.

[4] F. Ginelli, F. Peruani, M.-H. Pillot, H. Chaté, G. Theraulaz, and R. Bon, "Intermittent collective dynamics emerge from conflicting imperatives in sheep herds," *Proc. Natl. Acad. Sci.*, vol. 112, no. 41, pp. 12729–12734, 2015.

[5] D. Nesbitt, G. Pruessner, and C. F. Lee, "Edge instability in incompressible planar active fluids," *Phys. Rev. E*, vol. 96, no. 6, pp. 1–7, 2017.

[6] J. Zimmermann, M. Basan, and H. Levine, "An instability at the edge of a tissue of collectively migrating cells can lead to finger formation during wound healing," *Eur. Phys. J. Spec. Top.*, vol. 223, no. 7, pp. 1259–1264, 2014.

[7] F. Giavazzi, M. Paoluzzi, M. Macchi, D. Bi, G. Scita, M. L. Manning, R. Cerbino, and M. C. Marchetti, "Flocking transitions in confluent tissues," *Soft Matter*, vol. 14, no. 18, pp. 3471–3477, 2018.

[8] M. Basan, J. Elgeti, E. Hannezo, W.-J. W.-J. Rappel, and H. Levine, "Alignment of cellular motility forces with tissue flow as a mechanism for efficient wound healing," *Proc. Natl. Acad. Sci. U. S. A.*, vol. 110, no. 7, pp. 2452–9, 2013.

[9] S. F. Schoeller and E. E. Keaveny, "From flagellar undulations to collective motion: predicting the dynamics of sperm suspensions," *J. R. Soc. Interface*, vol. 15, no. 140, p. 20170834, 2018.

[10] Y. Hatwalne, S. Ramaswamy, M. Rao, and R. A. Simha, "Rheology of Active-Particle Suspensions," *Phys. Rev. Lett.*, vol. 92, no. 11, pp. 118101–1, 2004.

[11] C. W. Wolgemuth, "Collective Swimming and the Dynamics of Bacterial Turbulence," *Biophys. J.*, vol. 95, no. 4, pp. 1564–1574, 2008.

[12] G. Liu, A. Patch, F. Bahar, D. Yllanes, R. D. Welch, M. C. Marchetti, S. Thutupalli, and J. W. Shaevitz, "Self-Driven Phase Transitions Drive Myxococcus xanthus Fruiting Body Formation," *Phys. Rev. Lett.*, vol. 122, no. 24, p. 248102, 2019.

[13] V. Schaller, C. Weber, C. Semmrich, E. Frey, and A. R. Bausch, "Polar patterns of driven filaments," *Nature*, vol. 467, no. 7311, pp. 73–77, 2010.

[14] Y. Sumino, K. H. Nagai, Y. Shitaka, D. Tanaka, K. Yoshikawa, H. Chaté, and K. Oiwa, "Large-scale vortex lattice emerging from collectively moving microtubules," *Nature*, vol. 483, no. 7390, pp. 448–452, 2012.

[15] A. Opathalage, M. M. Norton, M. P. N. Juniper, B. Langeslay, S. A. Aghvami, S. Fraden, and Z. Dogic, "Self-organized dynamics and the

transition to turbulence of confined active nematics," *Proc. Natl. Acad. Sci.*, vol. 116, no. 11, pp. 4788–4797, 2019.

[16] M. E. Cates and J. Tailleur, "Motility-Induced Phase Separation," *Annu. Rev. Condens. Matter Phys.*, vol. 6, no. 1, pp. 219–244, 2015.

[17] D. Needleman and Z. Dogic, "Active matter at the interface between materials science and cell biology," *Nat. Rev. Mater.*, vol. 2, no. 9, p. 17048, 2017.

[18] K. Kruse and F. Jülicher, "Self-organization and mechanical properties of active filament bundles.," *Phys. Rev. E. Stat. Nonlin. Soft Matter Phys.*, vol. 67, no. 5 Pt 1, p. 051913, 2003.

[19] T. E. Schaus, E. W. Taylor, and G. G. Borisy, "Self-organization of actin filament orientation in the dendritic-nucleation/array-treadmilling model.," *Proc. Natl. Acad. Sci. U. S. A.*, vol. 104, no. 17, pp. 7086–7091, 2007.

[20] N. H. Nguyen, D. Klotsa, M. Engel, and S. C. Glotzer, "Emergent Collective Phenomena in a Mixture of Hard Shapes through Active Rotation," *Phys. Rev. Lett.*, vol. 112, no. 7, p. 075701, 2014.

[21] S. Weitz, A. Deutsch, and F. Peruani, "Self-propelled rods exhibit a phase-separated state characterized by the presence of active stresses and the ejection of polar clusters," *Phys. Rev. E - Stat. Nonlinear, Soft Matter Phys.*, vol. 92, no. 1, pp. 1–9, 2015.

[22] H. Youn Lee and M. Kardar, "Macroscopic equations for pattern formation in mixtures of microtubules and molecular motors," *Phys. Rev. E*, vol. 64, no. 5, p. 056113, 2001.

[23] S. Sankararaman, G. I. Menon, and P. B. Sunil Kumar, "Self-organized pattern formation in motor-microtubule mixtures," *Phys. Rev. E*, vol. 70, no. 3, p. 031905, 2004.

[24] F. Ziebert and W. Zimmermann, "Pattern formation driven by nematic ordering of assembling biopolymers," *Phys. Rev. E*, vol. 70, no. 2, p. 022902, 2004.

[25] F. Ziebert and W. Zimmermann, "Nonlinear competition between asters and stripes in filament-motor systems," *Eur. Phys. J. E*, vol. 18, no. 1, pp. 41–54, 2005.

[26] J. S. Bois, F. Jülicher, and S. W. Grill, "Pattern Formation in Active Fluids," *Phys. Rev. Lett.*, vol. 106, no. 2, p. 028103, 2011.

[27] A. P. Solon, J.-b. Caussin, D. Bartolo, H. Chaté, and J. Tailleur, "Pattern formation in flocking models: A hydrodynamic description," *Phys. Rev. E*, vol. 92, no. 6, p. 062111, 2015.

[28] S. M. Fielding, D. Marenduzzo, and M. E. Cates, "Nonlinear dynamics and rheology of active fluids: Simulations in two dimensions," *Phys. Rev. E - Stat. Nonlinear, Soft Matter Phys.*, vol. 83, no. 4, pp. 1–14, 2011.

[29] H. H. Wensink, J. Dunkel, S. Heidenreich, K. Drescher, R. E. Goldstein, H. Lowen, and J. M. Yeomans, "Meso-scale turbulence in living fluids," *Proc. Natl. Acad. Sci.*, vol. 109, no. 36, pp. 14308–14313, 2012.

[30] S. P. Thampi, R. Golestanian, and J. M. Yeomans, "Vorticity, defects and correlations in active turbulence," *Philos. Trans. R. Soc. A Math. Phys. Eng. Sci.*, vol. 372, no. 2029, p. 20130366, 2014.

[31] V. Bratanov, F. Jenko, and E. Frey, "New class of turbulence in active fluids," *Proc. Natl. Acad. Sci.*, vol. 112, no. 49, pp. 15048–15053, 2015.

[32] B. Mahault, X. C. Jiang, E. Bertin, Y. Q. Ma, A. Patelli, X. Q. Shi, and H. Chaté, "Self-Propelled Particles with Velocity Reversals and Ferromagnetic Alignment: Active Matter Class with Second-Order Transition to Quasi-Long-Range Polar Order," *Phys. Rev. Lett.*, vol. 120, no. 25, pp. 1–7, 2018.

[33] Y. Fily and M. C. Marchetti, "Athermal Phase Separation of Self-Propelled Particles with No Alignment," *Phys. Rev. Lett.*, vol. 108, no. 23, p. 235702, 2012.

[34] M. E. Cates and J. Tailleur, "When are active Brownian particles and run-and-tumble particles equivalent? Consequences for motility-induced phase separation," *EPL*, vol. 101, no. 2, p. 20010, 2013.

[35] G. Gonnella, D. Marenduzzo, A. Suma, and A. Tiribocchi, "Motility-induced phase separation and coarsening in active matter," *Comptes Rendus Phys.*, vol. 16, no. 3, pp. 316–331, 2015.

[36] Z. Cheng, Z. Chen, T. Vicsek, D. Chen, and H.-t. Zhang, "Pattern phase transitions of self-propelled particles: gases, crystals, liquids, and mills," *New J. Phys.*, vol. 18, no. 10, p. 103005, 2016.

[37] C. F. Lee, "Interface stability, interface fluctuations, and the GibbsThomson relationship in motility-induced phase separations," *Soft Matter*, vol. 13, no. 2, pp. 376–385, 2017.

[38] L. Giomi, T. B. Liverpool, and M. C. Marchetti, "Sheared active fluids: Thickening, thinning, and vanishing viscosity," *Phys. Rev. E - Stat. Nonlinear, Soft Matter Phys.*, vol. 81, no. 5, pp. 1–9, 2010.

[39] S. J. DeCamp, G. S. Redner, A. Baskaran, M. F. Hagan, and Z. Dogic, "Orientational order of motile defects in active nematics," *Nat. Mater.*, vol. 14, no. 11, pp. 1110–1115, 2015.

[40] J. Toner and Y. Tu, "Long-range order in a two-dimensional dynamical XY model: How birds fly together," *Phys. Rev. Lett.*, vol. 75, no. 23, pp. 4326–4329, 1995.

[41] J. Toner and Y. Tu, "Flocks, herds, and schools: A quantitative theory of flocking," *Phys. Rev. E*, vol. 58, no. 4, pp. 4828–4858, 1998.

[42] G. Grégoire and H. Chaté, "Onset of Collective and Cohesive Motion," *Phys. Rev. Lett.*, vol. 92, no. 2, p. 4, 2004.

[43] J. Toner, Y. Tu, and S. Ramaswamy, "Hydrodynamics and phases of flocks," *Ann. Phys. (N. Y).*, vol. 318, no. 1 SPEC. ISS., pp. 170–244, 2005.

[44] E. Bertin, M. Droz, and G. Grégoire, "Hydrodynamic equations for self-propelled particles: microscopic derivation and stability analysis," *J. Phys. A Math. Theor.*, vol. 42, no. 44, p. 445001, 2009.

[45] N. S. Gov, "Traction forces during collective cell motion.," *HFSP J.*, vol. 3, no. 4, pp. 223–227, 2009.

[46] F. Ginelli and H. Chaté, "Relevance of metric-free interactions in flocking phenomena," *Phys. Rev. Lett.*, vol. 105, no. 16, pp. 1–4, 2010.

[47] C. F. Lee, "Fluctuation-induced collective motion: A single-particle density analysis," *Phys. Rev. E - Stat. Nonlinear, Soft Matter Phys.*, vol. 81, no. 3, pp. 1–6, 2010.

[48] T. E. Angelini, E. Hannezo, X. Trepat, M. Marquez, J. J. Fredberg, and D. A. Weitz, "Glass-like dynamics of collective cell migration," *Proc Natl Acad Sci U S A*, vol. 108, no. 12, pp. 4714–4719, 2011.

[49] J. Toner, "Reanalysis of the hydrodynamic theory of fluid, polar-ordered flocks," *Phys. Rev. E - Stat. Nonlinear, Soft Matter Phys.*, vol. 86, no. 3, pp. 1–9, 2012.

[50] T. Vicsek, A. Czirók, E. Ben-Jacob, I. Cohen, and O. Shochet, "Novel Type of Phase Transition in a System of Self-Driven Particles," *Phys. Rev. Lett.*, vol. 75, no. 6, pp. 1226–1229, 1995.

[51] A. Czirók, H. E. Stanley, and T. Vicsek, "Spontaneously ordered motion of self-propelled particles," *J. Phys. A. Math. Gen.*, vol. 30, no. 5, pp. 1375–1385, 1997.

[52] P. Galajda, J. Keymer, P. Chaikin, and R. Austin, "A Wall of Funnels Concentrates Swimming Bacteria," *J. Bacteriol.*, vol. 189, no. 23, pp. 8704–8707, 2007.

[53] J. Tailleur and M. E. Cates, "Sedimentation, trapping, and rectification of dilute bacteria," *EPL*, vol. 86, no. 6, p. 60002, 2009.

[54] J. Bialké, H. Löwen, and T. Speck, "Microscopic theory for the phase separation of self-propelled repulsive disks," *EPL*, vol. 103, no. 3, p. 30008, 2013.

[55] I. Buttinoni, J. Bialké, F. Kümmel, H. Löwen, C. Bechinger, and T. Speck, "Dynamical Clustering and Phase Separation in Suspensions of Self-Propelled Colloidal Particles," *Phys. Rev. Lett.*, vol. 110, no. 23, p. 238301, 2013.

[56] G. S. Redner, M. F. Hagan, and A. Baskaran, "Structure and Dynamics of a Phase-Separating Active Colloidal Fluid," *Phys. Rev. Lett.*, vol. 110, no. 5, p. 055701, 2013.

[57] J. Stenhammar, A. Tiribocchi, R. J. Allen, D. Marenduzzo, and M. E. Cates, "Continuum Theory of Phase Separation Kinetics for Active Brownian Particles," *Phys. Rev. Lett.*, vol. 111, no. 14, p. 145702, 2013.

[58] J. Stenhammar, D. Marenduzzo, R. J. Allen, and M. E. Cates, "Phase behaviour of active Brownian particles: the role of dimensionality," *Soft Matter*, vol. 10, no. 10, pp. 1489–1499, 2014.

[59] M. J. Schnitzer, "Theory of continuum random walks and application to chemotaxis," *Phys. Rev. E*, vol. 48, no. 4, pp. 2553–2568, 1993.

[60] J. Arlt, V. A. Martinez, A. Dawson, T. Pilizota, and W. C. K. Poon, "Painting with light-powered bacteria," *Nat. Commun.*, vol. 9, no. 1, p. 768, 2018.

[61] M. B. Miller and B. L. Bassler, "Quorum Sensing in Bacteria," *Annu. Rev. Microbiol.*, vol. 55, no. 1, pp. 165–199, 2001.

[62] Z. Csahók and T. Vicsek, "Lattice-gas model for collective biological motion," *Phys. Rev. E*, vol. 52, no. 5, pp. 5297–5303, 1995.

[63] H. Chaté, F. Ginelli, G. Grégoire, and F. Raynaud, "Collective motion of self-propelled particles interacting without cohesion," *Phys. Rev. E*, vol. 77, no. 4, p. 046113, 2008.

[64] T. Ihle, "Kinetic theory of flocking: Derivation of hydrodynamic equations," *Phys. Rev. E*, vol. 83, no. 3, p. 030901, 2011.

[65] A. P. Solon and J. Tailleur, "Revisiting the flocking transition using active Spins," *Phys. Rev. Lett.*, vol. 111, no. 7, pp. 1–5, 2013.

[66] F. Thüroff, C. A. Weber, and E. Frey, "Numerical Treatment of the Boltzmann Equation for Self-Propelled Particle Systems," *Phys. Rev. X*, vol. 4, no. 4, p. 041030, 2014.

[67] F. Ginelli, "The Physics of the Vicsek model," *Eur. Phys. J. Spec. Top.*, vol. 225, no. 11-12, pp. 2099–2117, 2016.

[68] D. A. Lauffenburger and A. F. Horwitz, "Cell Migration: A Physically Integrated Molecular Process," *Cell*, vol. 84, no. 3, pp. 359–369, 1996.

[69] M. Poujade, E. Grasland-Mongrain, A. Hertzog, J. Jouanneau, P. Chavrier, B. Ladoux, A. Buguin, and P. Silberzan, "Collective migration of an epithelial monolayer in response to a model wound.," *Proc. Natl. Acad. Sci. U. S. A.*, vol. 104, no. 41, pp. 15988–93, 2007.

[70] X. Trepat, M. R. Wasserman, T. E. Angelini, E. Millet, D. A. Weitz, J. P. Butler, and J. J. Fredberg, "Physical forces during collective cell migration," *Nat. Phys.*, vol. 5, no. 6, pp. 426–430, 2009.

[71] L. Petitjean, M. Reffay, E. Grasland-Mongrain, M. Poujade, B. Ladoux, A. Buguin, and P. Silberzan, "Velocity fields in a collectively migrating epithelium," *Biophys. J.*, vol. 98, no. 9, pp. 1790–1800, 2010.

[72] S. Mark, R. Shlomovitz, N. S. Gov, M. Poujade, E. Grasland-Mongrain, and P. Silberzan, "Physical model of the dynamic instability in an expanding cell culture," *Biophys. J.*, vol. 98, no. 3, pp. 361–370, 2010.

[73] N. Sepúlveda, L. Petitjean, O. Cochet, E. Grasland-Mongrain, P. Silberzan, and V. Hakim, "Collective Cell Motion in an Epithelial Sheet Can Be Quantitatively Described by a Stochastic Interacting Particle Model," *PLoS Comput. Biol.*, vol. 9, no. 3, 2013.

[74] M. L. Blow, S. P. Thampi, and J. M. Yeomans, "Biphasic, Lyotropic, Active Nematics," *Phys. Rev. Lett.*, vol. 113, no. 24, p. 248303, 2014.

[75] A. Doostmohammadi, S. P. Thampi, T. B. Saw, C. T. Lim, B. Ladoux, and J. M. Yeomans, "Celebrating Soft Matter's 10th Anniversary: Cell division: a source of active stress in cellular monolayers," *Soft Matter*, vol. 11, no. 37, pp. 7328–7336, 2015.

[76] A. Doostmohammadi, S. P. Thampi, and J. M. Yeomans, "Defect-Mediated Morphologies in Growing Cell Colonies," *Phys. Rev. Lett.*, vol. 117, no. 4, p. 048102, 2016.

[77] A. Cavagna, L. Del Castello, I. Giardina, T. Grigera, A. Jelic, S. Melillo, T. Mora, L. Parisi, E. Silvestri, M. Viale, and A. M. Walczak, "Flocking and Turning: a New Model for Self-organized Collective Motion," *J. Stat. Phys.*, vol. 158, no. 3, pp. 601–627, 2014.

[78] B. Liebchen and D. Levis, "Collective Behavior of Chiral Active Matter: Pattern Formation and Enhanced Flocking," *Phys. Rev. Lett.*, vol. 119, no. 5, pp. 1–5, 2017.

[79] M. Bindschadler and J. L. McGrath, "Sheet migration by wounded monolayers as an emergent property of single-cell dynamics.," *J. Cell Sci.*, vol. 120, no. Pt 5, pp. 876–884, 2007.

[80] M. Basan, J. Prost, J.-F. Joanny, and J. Elgeti, "Dissipative particle dynamics simulations for biological tissues: rheology and competition.," *Phys. Biol.*, vol. 8, no. 2, p. 026014, 2011.

[81] N. Podewitz, F. Jülicher, G. Gompper, and J. Elgeti, "Interface dynamics of competing tissues," *New J. Phys.*, vol. 18, no. 8, p. 083020, 2016.

[82] D. Forster, *Hydrodynamic fluctuations, broken symmetry, and correlation functions*. Frontiers in physics; 47, Reading, Mass.: Benjamin, 1975.

[83] E. Bertin, M. Droz, and G. Grégoire, "Boltzmann and hydrodynamic description for self-propelled particles," *Phys. Rev. E*, vol. 74, no. 2, p. 022101, 2006.

[84] A. Baskaran and M. C. Marchetti, "Hydrodynamics of self-propelled hard rods," *Phys. Rev. E*, vol. 77, no. 1, p. 011920, 2008.

[85] T. Ihle, "Invasion-wave-induced first-order phase transition in systems of active particles," *Phys. Rev. E*, vol. 88, no. 4, p. 040303, 2013.

[86] R. Benzi, S. Succi, and M. Vergassola, "The lattice Boltzmann equation: theory and applications," *Phys. Rep.*, vol. 222, no. 3, pp. 145–197, 1992.

[87] S. Chen, D. Martínez, and R. Mei, "On boundary conditions in lattice Boltzmann methods," *Phys. Fluids*, vol. 8, no. 9, pp. 2527–2536, 1996.

[88] P. M. Chaikin and T. C. Lubensky, *Principles of Condensed Matter Physics*. Cambridge University Press, 1995.

[89] U. Frisch and D. Pazzis, "Lattice as Automata for the Navier-Stokes Equation," *Phys. Rev. Lett.*, pp. 1505–1508, 1986.

[90] J. Hardy, Y. Pomeau, and O. de Pazzis, "Time evolution of a two-dimensional model system. I. Invariant states and time correlation functions," *J. Math. Phys.*, vol. 14, no. 12, pp. 1746–1759, 1973.

[91] J. Hardy, Y. Pomeau, and O. de Pazzis, "Time Evolution of a Two-Dimensional Classical Lattice System," *Phys. Rev. Lett.*, vol. 31, no. 5, pp. 276–279, 1973.

[92] J. Hardy, O. de Pazzis, and Y. Pomeau, "Molecular dynamics of a classical lattice gas: Transport properties and time correlation functions," *Phys. Rev. A*, vol. 13, no. 5, pp. 1949–1961, 1976.

[93] U. Frisch, D. d 'Humieres, B. Hasslacher, P. Lallemand, Y. Pomeau, and J.-P. Rivet, "Lattice Gas Hydrodynamics in Two and Three Dimensions," *Complex Syst.*, vol. 1, pp. 649–707, 1987.

[94] F. J. Higuera and J. Jiménez, "Boltzmann approach to lattice gas simulations," *EPL*, vol. 9, no. 7, pp. 663–668, 1989.

[95] F. J. Higuera, S. Succi, and R. Benzi, "Lattice gas-dynamics with enhanced collisions," *Eur. Lett.*, vol. 9, pp. 345–349, 1989.

[96] G. R. McNamara and G. Zanetti, "Use of the Boltzmann Equation to Simulate Lattice-Gas Automata," *Phys. Rev. Lett.*, vol. 61, no. 20, pp. 2332–2335, 1988.

[97] H. Chen, S. Chen, and W. H. Matthaeus, "Recovery of the Navier-Stokes equations using a lattice-gas Boltzmann method," *Phys. Rev. A*, vol. 45, no. 8, pp. R5339–R5342, 1992.

[98] X. He and L.-S. Luo, "Theory of the lattice Boltzmann method: From the Boltzmann equation to the lattice Boltzmann equation," *Phys. Rev. E*, vol. 56, no. 6, pp. 6811–6817, 1997.

[99] X. He and L.-S. Luo, "Lattice Boltzmann Model for the Incompressible NavierStokes Equation," *J. Stat. Phys.*, vol. 88, no. 3/4, pp. 927–944, 1997.

[100] Q. Zou, S. Hou, S. Chen, and G. D. Doolen, "A improved incompressible lattice Boltzmann model for time-independent flows," *J. Stat. Phys.*, vol. 81, no. 1-2, pp. 35–48, 1995.

[101] Z. Guo, B. Shi, and N. Wang, "Lattice BGK Model for Incompressible NavierStokes Equation," *J. Comput. Phys.*, vol. 165, no. 1, pp. 288–306, 2000.

[102] Q. Zou and X. He, "On pressure and velocity boundary conditions for the lattice Boltzmann BGK model," *Phys. Fluids*, vol. 9, no. 6, pp. 1591–1598, 1997.

[103] E. Fattahi, C. Waluga, B. Wohlmuth, U. Rüde, M. Manhart, and R. Helmig, "Lattice Boltzmann methods in porous media simulations: From laminar to turbulent flow," *Comput. Fluids*, vol. 140, pp. 247–259, 2016.

[104] S. Ramachandran, P. B. S. Kumar, and I. Pagonabarraga, "A Lattice-Boltzmann model for suspensions of self-propelling colloidal particles," *Eur. Phys. J. E*, vol. 20, no. 2, pp. 151–158, 2006.

[105] C. Denniston, E. Orlandini, and J. M. Yeomans, "Lattice Boltzmann simulations of liquid crystal hydrodynamics," *Phys. Rev. E*, vol. 63, no. 5, p. 056702, 2001.

[106] C. Denniston, D. Marenduzzo, E. Orlandini, and J. M. Yeomans, "Lattice Boltzmann algorithm for threedimensional liquidcrystal hydrodynamics," *Phil. Trans. R. Soc. Lond. A*, vol. 362, no. 1821, pp. 1745–1754, 2004.

[107] D. Marenduzzo, E. Orlandini, and J. M. Yeomans, "Switching hydrodynamics in multi-domain, twisted nematic, liquid-crystal devices," *Europhys. Lett.*, vol. 71, no. 4, pp. 604–610, 2005.

[108] D. Marenduzzo, E. Orlandini, M. E. Cates, and J. M. Yeomans, "Steady-state hydrodynamic instabilities of active liquid crystals: Hybrid lattice Boltzmann simulations," *Phys. Rev. E - Stat. Nonlinear, Soft Matter Phys.*, vol. 76, no. 3, pp. 1–18, 2007.

[109] M. E. Cates, O. Henrich, D. Marenduzzo, and K. Stratford, "Lattice Boltzmann simulations of liquid crystalline fluids: active gels and blue phases," *Soft Matter*, vol. 5, no. 20, pp. 3791–3800, 2009.

[110] A. Doostmohammadi, T. N. Shendruk, K. Thijssen, and J. M. Yeomans, "Onset of meso-scale turbulence in active nematics," *Nat. Commun.*, vol. 8, no. May, p. 15326, 2017.

[111] L. Giomi, M. C. Marchetti, and T. B. Liverpool, "Complex Spontaneous Flows and Concentration Banding in Active Polar Films," *Phys. Rev. Lett.*, vol. 101, no. 19, p. 198101, 2008.

[112] J. Elgeti, M. E. Cates, and D. Marenduzzo, "Defect hydrodynamics in 2D polar active fluids," *Soft Matter*, vol. 7, no. 7, p. 3177, 2011.

[113] M. L. Blow, M. Aqil, B. Liebchen, and D. Marenduzzo, "Motility of active nematic films driven by active anchoring," *Soft Matter*, vol. 13, no. 36, pp. 6137–6144, 2017.

[114] M. Ravnik and J. M. Yeomans, "Confined active nematic flow in cylindrical capillaries," *Phys. Rev. Lett.*, vol. 110, no. 2, pp. 1–5, 2013.

[115] S. P. Thampi, R. Golestanian, and J. M. Yeomans, "Velocity correlations in an active nematic," *Phys. Rev. Lett.*, vol. 111, no. 11, pp. 2–6, 2013.

[116] B. Partridge and C. F. Lee, "Critical Motility-Induced Phase Separation Belongs to the Ising Universality Class," *Phys. Rev. Lett.*, vol. 123, no. 6, p. 068002, 2019.

[117] F. Peruani, T. Klauss, A. Deutsch, and A. Voss-Boehme, "Traffic Jams, Gliders, and Bands in the Quest for Collective Motion of Self-Propelled Particles," *Phys. Rev. Lett.*, vol. 106, no. 12, p. 128101, 2011.

[118] H. Chen, I. Goldhirsch, and S. A. Orszag, "Discrete rotational symmetry, moment isotropy, and higher order lattice Boltzmann models," *J. Sci. Comput.*, vol. 34, no. 1, pp. 87–112, 2008.

[119] S. Chen and G. D. Doolen, "LATTICE BOLTZMANN METHOD FOR FLUID FLOWS," *Annu. Rev. Fluid Mech.*, vol. 30, no. 1, pp. 329–364, 1998.

[120] P. L. Bhatnagar, E. P. Gross, and M. Krook, "A Model for Collision Processes in Gases. I. Small Amplitude Processes in Charged and Neutral One-Component Systems," *Phys. Rev.*, vol. 94, no. 3, pp. 511–525, 1954.

[121] M. R. Swift, E. Orlandini, W. R. Osborn, and J. M. Yeomans, "Lattice Boltzmann simulations of liquid-gas and binary fluid systems," *Phys. Rev. E*, vol. 54, no. 5, pp. 5041–5052, 1996.

[122] M. M. P. Zegers, M.-A. Forget, J. Chernoff, K. E. Mostov, M. B. A. ter Beest, and S. H. Hansen, "Pak1 and PIX regulate contact inhibition during epithelial wound healing.," *EMBO J.*, vol. 22, no. 16, pp. 4155–65, 2003.

[123] M. J. Lighthill and G. B. Whitham, "On Kinematic Waves. II. A Theory of Traffic Flow on Long Crowded Roads," *Proc. R. Soc. A Math. Phys. Eng. Sci.*, vol. 229, no. 1178, pp. 317–345, 1955.

[124] S. K. Schnyder, J. J. Molina, Y. Tanaka, and R. Yamamoto, "Collective motion of cells crawling on a substrate: roles of cell shape and contact inhibition," *Sci. Rep.*, vol. 7, no. 1, p. 5163, 2017.

[125] Q. Li, P. Zhou, and H. J. Yan, "Revised Chapman-Enskog analysis for a class of forcing schemes in the lattice Boltzmann method," *Phys. Rev. E*, vol. 94, no. 4, p. 043313, 2016.

[126] C. A. Weber, C. F. Lee, and F. Jülicher, "Droplet ripening in concentration gradients," *New J. Phys.*, vol. 19, no. 5, p. 053021, 2017.

[127] C. F. Lee and J. D. Wurtz, "Novel physics arising from phase transitions in biology," *J. Phys. D. Appl. Phys.*, vol. 52, no. 2, p. 023001, 2019.

[128] A. Peshkov, S. Ngo, E. Bertin, H. Chaté, and F. Ginelli, "Continuous theory of active matter systems with metric-free interactions," *Phys. Rev. Lett.*, vol. 109, no. 9, pp. 1–6, 2012.

[129] L. Chen, J. Toner, and C. F. Lee, "Critical phenomenon of the orderdisorder transition in incompressible active fluids," *New J. Phys.*, vol. 17, no. 4, p. 042002, 2015.

[130] J. T. Siebert, F. Dittrich, F. Schmid, K. Binder, T. Speck, and P. Virnau, "Critical behavior of active Brownian particles," *Phys. Rev. E*, vol. 98, no. 3, p. 030601, 2018.

[131] F. Caballero, C. Nardini, and M. E. Cates, "From bulk to microphase separation in scalar active matter: a perturbative renormalization group analysis," *J. Stat. Mech. Theory Exp.*, vol. 2018, no. 12, p. 123208, 2018.

[132] H. K. Janssen and B. Schmittmann, "Field theory of critical behaviour in driven diffusive systems," *Zeitschrift für Phys. B Condens. Matter*, vol. 64, no. 4, pp. 503–514, 1986.

[133] K.-t. Leung and J. L. Cardy, "Field theory of critical behavior in a driven diffusive system," *J. Stat. Phys.*, vol. 44, no. 3-4, pp. 567–588, 1986.

[134] P. G. Saffman and G. Taylor, "The Penetration of a Fluid into a Porous Medium or Hele-Shaw Cell Containing a More Viscous Liquid," *Proc. R. Soc. London. Ser. A. Math. Phys. Sci.*, vol. 245, no. 1242, pp. 312 LP – 329, 1958.

[135] N. S. Gov, "Collective cell migration patterns: follow the leader.," *Proc. Natl. Acad. Sci. U. S. A.*, vol. 104, no. 41, pp. 15970–15971, 2007.

[136] T. Omelchenko, J. M. Vasiliev, I. M. Gelfand, H. H. Feder, and E. M. Bonder, "Rho-dependent formation of epithelial "leader" cells during wound healing.," *Proc. Natl. Acad. Sci. U. S. A.*, vol. 100, no. 19, pp. 10788–10793, 2003.

[137] P. Lenz, *Cell Motility*. Biological and Medical Physics, Biomedical Engineering, Springer, 2007.

[138] L. Chen, C. F. Lee, and J. Toner, "Mapping two-dimensional polar active fluids to two-dimensional soap and one-dimensional sandblasting," *Nat. Commun.*, vol. 7, p. 12215, 2016.

[139] G. Forgacs, R. A. Foty, Y. Shafrir, and M. S. Steinberg, "Viscoelastic Properties of Living Embryonic Tissues: a Quantitative Study," *Biophys. J.*, vol. 74, no. 5, pp. 2227–2234, 1998.

[140] E.-m. Schötz, R. D. Burdine, F. Jülicher, M. S. Steinberg, C.-p. Heisenberg, and R. A. Foty, "Quantitative differences in tissue surface tension influence zebrafish germ layer positioning," *HFSP J.*, vol. 2, no. 1, pp. 42–56, 2008.

[141] R. A. Foty, G. Forgacs, C. M. Pfleger, and M. S. Steinberg, "Liquid properties of embryonic tissues: Measurement of interfacial tensions," *Phys. Rev. Lett.*, vol. 72, no. 14, pp. 2298–2301, 1994.

Appendix A

Reuse and permissions licence for Chapter 4

American Physical Society
Reuse and Permissions License

30-Jul-2019

This license agreement between the American Physical Society ("APS") and David Nesbitt ("You") consists of your license details and the terms and conditions provided by the American Physical Society and SciPris.

Licensed Content Information

License Number:	**RNP/19/JUL/017203**
License date:	30-Jul-2019
DOI:	10.1103/PhysRevE.96.062615
Title:	Edge instability in incompressible planar active fluids
Author:	David Nesbitt, Gunnar Pruessner, and Chiu Fan Lee
Publication:	Physical Review E
Publisher:	American Physical Society
Cost:	USD $ 0.00

Request Details

Does your reuse require significant modifications: No

Specify intended distribution locations:	Worldwide
Reuse Category:	Reuse in a thesis/dissertation
Requestor Type:	Author of requested content
Items for Reuse:	Whole Article
Format for Reuse:	Print and Electronic
Total number of print copies:	Up to 1000

Information about New Publication:

University/Publisher:	Imperial College London
Title of dissertation/thesis:	Exploring the Behaviour of Two-Dimensional Dry Polar Active Fluids in a Dense Regime
Author(s):	David Nesbitt
Expected completion date:	Jul. 2019

License Requestor Information

Name:	David Nesbitt
Affiliation:	Individual
Email Id:	david.nesbitt13@imperial.ac.uk
Country:	United Kingdom

American Physical Society
Reuse and Permissions License

TERMS AND CONDITIONS

The American Physical Society (APS) is pleased to grant the Requestor of this license a non-exclusive, non-transferable permission, limited to Print and Electronic format, provided all criteria outlined below are followed.

1. You must also obtain permission from at least one of the lead authors for each separate work, if you haven't done so already. The author's name and affiliation can be found on the first page of the published Article.
2. For electronic format permissions, Requestor agrees to provide a hyperlink from the reprinted APS material using the source material's DOI on the web page where the work appears. The hyperlink should use the standard DOI resolution URL, http://dx.doi.org/{DOI}. The hyperlink may be embedded in the copyright credit line.
3. For print format permissions, Requestor agrees to print the required copyright credit line on the first page where the material appears: "Reprinted (abstract/excerpt/figure) with permission from [(FULL REFERENCE CITATION) as follows: Author's Names, APS Journal Title, Volume Number, Page Number and Year of Publication.] Copyright (YEAR) by the American Physical Society."
4. Permission granted in this license is for a one-time use and does not include permission for any future editions, updates, databases, formats or other matters. Permission must be sought for any additional use.
5. Use of the material does not and must not imply any endorsement by APS.
6. APS does not imply, purport or intend to grant permission to reuse materials to which it does not hold copyright. It is the requestor's sole responsibility to ensure the licensed material is original to APS and does not contain the copyright of another entity, and that the copyright notice of the figure, photograph, cover or table does not indicate it was reprinted by APS with permission from another source.
7. The permission granted herein is personal to the Requestor for the use specified and is not transferable or assignable without express written permission of APS. This license may not be amended except in writing by APS.
8. You may not alter, edit or modify the material in any manner.
9. You may translate the materials only when translation rights have been granted.
10. APS is not responsible for any errors or omissions due to translation.
11. You may not use the material for promotional, sales, advertising or marketing purposes.
12. The foregoing license shall not take effect unless and until APS or its agent, Aptara, receives payment in full in accordance with Aptara Billing and Payment Terms and Conditions, which are incorporated herein by reference.
13. Should the terms of this license be violated at any time, APS or Aptara may revoke the license with no refund to you and seek relief to the fullest extent of the laws of the USA. Official written notice will be made using the contact information provided with the permission request. Failure to receive such notice will not nullify revocation of the permission.
14. APS reserves all rights not specifically granted herein.
15. This document, including the Aptara Billing and Payment Terms and Conditions, shall be the entire agreement between the parties relating to the subject matter hereof.